Aqueous Basic Solutions: Hydroxide Solvation, Structural Diffusion, and Comparison to the Hydrated Proton

Dominik Marx

Lehrstuhl für Theoretische Chemie, Ruhr-Universität Bochum, 44780 Bochum, Germany

Amalendu Chandra

Department of Chemistry, Indian Institute of Technology, Kanpur, India 208016

Mark E. Tuckerman*

Department of Chemistry and Courant Institute of Mathematical Sciences, 100 Washington Square East, New York University, New York, New York 10003

Received June 30, 2009

Contents

* .

1. General Introduction

Many hydrogen-bonded liquids, molecular solids, and low-dimensional systems support anomalous diffusion mechanisms of topological charge defects created by the addition or removal of protons. The most familiar examples are the "classic" cases of aqueous acidic and basic solutions,[1] where the defects appear in the form of hydrated hydronium (H_3O^+) and hydroxide (OH^-) ions, denoted as H^+(aq) and OH^-(aq), respectively.[2] While anomalous charge migration has important consequences in chemical,[1,3,4] biological,[5−8] and technological[9,10] applications, *vide infra*, providing a molecular-level, mechanistic understanding of the fascinating physical principles underlying the charge transport process is a challenging, yet fundamental, problem in physical chemistry.[11]

A skeletal mechanistic picture that still guides our understanding of the anomalous diffusion process in hydrogen-bonded systems can be traced back to a paper from 1806 by Theodor Christian Johann Dietrich von Grotthuss (1785−1822), a renowned scholar from Leipzig. Two centuries ago, von Grotthuss suggested that a structural or topological defect is actually transported *via* sequential proton transfer (PT) reactions along some arrangement of water molecules;[12] a recent review[13] includes facsimile reprints of the original drawings. Although many long-standing efforts to elucidate the details of this so-called structural ("Grotthuss") diffusion mechanism are known, the ingenuity of von Grotthuss' proposal has only recently been fully recognized. The problem of unraveling the *microscopic details* of structural diffusion mechanisms in hydrogen-bonded media is an active

10.1021/cr900233f
Published on Web 02/22/2010

Dominik Marx studied chemistry and physics at Universität Mainz and the University of California at Irvine, where he worked with Max Wolfsberg on isotope effects. He received his *Diplom* (M.Sc.) in Chemistry (1990) with Karl Heinzinger at MPI für Chemie and his Ph.D. (1992) with Kurt Binder (Institut für Physik, Universität Mainz). Thereafter, he worked as a Postdoctoral Fellow at IBM Zurich Research Laboratory (Rüschlikon) with Michele Parrinello, as a staff scientist at MPI für Festkörperforschung, and obtained the *Habilitation* in Theoretical Physics at Universität Stuttgart (1998), before he received a full Professorship at Ruhr-Universität Bochum in 1999. Several Chairs in Germany and abroad were offered to him, and he is currently Distinguished Professor of Theoretical Chemistry and Head of the Center for Theoretical Chemistry at the University of Bochum. Dominik Marx was fascinated from early on by the multifaceted problems that are posed by the physics and chemistry of complex molecular systems which can only be tackled using utmost "realistic" computer simulation approaches. The leitmotives of the Marx Group are, on the one hand, the development of novel quantum and quasiclassical simulation techniques for molecular many-body systems and, on the other, their application in terms of high-performance scientific computing.

Amalendu Chandra received his B.Sc. and M.Sc. degrees from the University of Burdwan, India, in 1984 and 1986, respectively, and his Ph.D. in 1991 from the Indian Institute of Science, Bangalore, where he worked in the group of Biman Bagchi. He was an Izaak Walton Killam postdoctoral fellow with Gren N. Patey at the University of British Columbia for two years before joining the faculty of the Indian Institute of Technology Kanpur in 1993. He is currently the Rahul and Namita Gautam Chair Professor in the Department of Chemistry of the same Institute, and he is a Fellow of the Indian Academy of Sciences. He was a Visiting Assistant Professor at Washington State University in 1997 and a Visiting Professor at Ruhr-Universität Bochum with Research Fellowships from the Alexander von Humboldt Foundation in 2002−2003 and also for short terms in subsequent years. He received the Shanti Swarup Bhatnagar Prize from the Council of Scientific and Industrial Research, Government of India, in 2007. His research interests include theoretical and computational studies of liquids, interfaces, and clusters using both classical and quantum methods.

area of research pursued experimentally mainly *via* diffraction and spectroscopic techniques and theoretically by state-of-the-art *ab initio* molecular dynamics (AIMD)[13] or parametrized empirical valence bond (EVB)[14] simulation approaches. These largely complementary methods have revealed important information about the structural fluctuations, kinetics, electronic properties, and thermodynamics connected with anomalous diffusion processes in aqueous solutions and various other hydrogen-bonded systems.

Mark Tuckerman obtained his B.S. in physics from U.C. Berkeley in 1986 and his Ph.D. in physics from Columbia University in 1993, working in the group of Bruce J. Berne. From 1993 to 1994, he held an IBM postdoctoral fellowship at the IBM Forschungslaboratorium in Rüschlikon, Switzerland, in the group of Michele Parrinello, and from 1995 to 1996, he held an NSF postdoctoral fellowship in Advanced Scientific Computing at the University of Pennsylvania in Philadelphia in the group of Michael L. Klein. He is currently Professor of Chemistry and Mathematics at New York University. His research interests include reactions in solution, organic reactions on semiconductor surfaces, development of the methodology of molecular dynamics, including novel techniques for enhancing conformational sampling and prediction of free energies in biological systems, and development of new approaches to electronic structure and *ab initio* molecular dynamics calculations.

In the case of excess protons, $H^+(aq)$, the pertinent details of the mechanism are now fairly well understood, as explained in current textbooks on physical chemistry[1] and reviewed in more detail recently.[13,14] The situation is much less clear for the ostensibly closely related complementary system, $OH^-(aq)$, and several mutually exclusive mechanistic proposals are being debated in the literature,[15,16] *vide infra*. In light of much recent progress, a review that is both critical and comprehensive is clearly timely. This review focuses on the controversial subject of the anomalous diffusion of hydroxide in basic solutions, $OH^-(aq)$. The stage is first set with a brief review of structural diffusion of $H^+(aq)$ in acidic solutions, primarily so that a comparison to $OH^-(aq)$ can be subsequently made. The presentation is based on the formal and unifying "presolvation concept", which is explained within the context of the $H^+(aq)$ diffusion process. In order to connect the qualitative predictions of the presolvation concept to actual mechanisms and the resulting kinetics in quantitative detail, a theoretical formalism introduced by us recently is used that allows structural diffusion to be analyzed, independent of the particular system, based on appropriately defined population correlation functions. This theoretical framework leads to consistent sets of various lifetimes and rates for $OH^-(aq)$ that can be directly compared to $H^+(aq)$ and can, in addition, be connected to different structural diffusion mechanisms proposed previously and the resulting diffusion coefficients. Moreover, the pertinent time scales can be compared to experimental results, in particular to data obtained using modern time-resolved vibrational spectroscopy.

The principal aims of the present review are to (1) review the various viewpoints that have emerged over the past decade, (2) dissect the resulting distinct scenarios at the molecular level, (3) extract theoretical predictions from these proposals, (4) connect these predictions to experimental conclusions as closely as currently possible, (5) assess counterion, concentration, microsolvation, and quantum effects, and finally (6) set the stage for new benchmark experiments to be carried out in the future by providing additional predictions. In passing, we touch on present issues such as the importance of quantum effects on the structure of water and aqueous solutions, the effect of microsolvation versus the condensed phase environment, and the validity and consistency of various types of AIMD approaches.

We have made our best effort to provide a comprehensive review of the existing literature on the solvation and diffusion of hydroxide in bulk water (the focus of the present review) up to the summer of 2009.

As a result of our analysis, it is concluded that there is a fundamental asymmetry between the solvation patterns of OH^-(aq) and H^+(aq), which supports the so-called "dynamical hypercoordination" scenario (see below) and is in stark contrast to the longstanding traditional view. The asymmetry between OH^-(aq) and H^+(aq) not only leads to *qualitatively* different structural diffusion mechanisms of these species in bulk solution, as shown here, but also has important consequences for numerous other systems. A key example is the ongoing controversy surrounding the equilibrium surface charge of aqueous droplets, surfaces, and interfaces[17−31] and the associated accumulation and exclusion of H^+(aq) versus OH^-(aq) at the water/vapor interface.[20,27] Another example is the use of polymeric membranes for use in emerging fuel-cell technologies. Perfluorinated materials, such as Nafion, or anhydrous materials, such as as polyethyleneoxide functionalized with imidazole, pyrazole, or sulfonic or phosphonic acid,[32−35] have been shown to shuttle positive charge defects *via* an anomalous diffusion mechanism. The same is true for alkaline-anion exchange membranes,[36−40] which transport OH^- in a direction opposite to that of H^+ in proton-exchange membranes. More generally, deep insights into the molecular scale mechanisms of anomalous charge migration in hydrogen-bonded systems have influenced our understanding of the proton-transport properties of widely varying systems including liquid hydrogen fluoride,[41−44] liquid methanol,[45] methanol−water solutions,[46,47] heterocyclic systems,[48−50] solid acids,[51−54] doped ammonium perchlorates,[55−57] alkaline hydrolysis reactions,[58,59] or hydroxide-rich ice systems.[60] Beyond understanding such bulklike mechanisms, these differences in solvation and charge migration are expected to have a significant impact on our view of issues related to the conductivity of water channels, pumps, and wires,[5−8,61−64] the properties of charge defects in hydrogen-bonded networks embedded in restricted geometries and under confinement, radiolysis, and photodetachment,[65−69] Hofmeister effects,[17,20,27,70,71] acids versus bases on ice nanosurfaces,[72−74] and atmospheric chemistry,[75−79] to name just a few.

2. Structural Diffusion in Aqueous Acids: Mechanism and Presolvation Concept

The observation that water and aqueous systems, in general, are able to transport topological charge defects in the form of hydrated hydronium and hydroxide ions at anomalously high rates[1] constitutes one of water's many unusual properties. However, despite the fundamental and wide-ranging importance of these elementary processes in chemistry, physics, and biology, the microscopic mechanistic details have proven difficult to pin down for many decades.[13] Substantial experimental[4,80−101] and theoretical[13,14,102−134] investigations into the structural diffusion or Grotthuss mechanism of the hydrated excess proton, H^+(aq), have ultimately produced an essentially consistent picture that has become textbook knowledge.[1] This picture involves an intricate interplay between a 3-fold solvated hydronium complex known as the "Eigen cation", $H_3O^+ \cdot (H_2O)_3$ or $H_9O_4^+$, and a shared-proton complex known as the "Zundel cation", $[H_2O\cdots H\cdots OH_2]^+$ or $H_5O_2^+$. These complexes are continuously interconverted *via* individual PT reactions. Pioneering AIMD simulations[102−104] showed that the interconversion itself is driven by specific fluctuations in the second shell of the hydrogen bond (HB) network around the charge defect. This was found to agree with a concurrent and independent theoretical analysis of existing data at that time.[106] In particular, a schematic mechanism in terms of a sequence of transitions from $H_9O_4^+$ to $H_5O_2^+$ to $H_9O_4^+$ complexes, as governed by hydrogen-bond cleavage of water molecules in the second solvation shell, has been sketched in Figure 2 of ref 106; see also refs 107, 109, and 118 for reviews and refinements. Consequently, the overall structural diffusion process is dominated by a nonvehicular migration mechanism of the charge defect, as shown schematically, for example, in Figure 2 of ref 106 or Figure 8 of ref 13 and, based on an actual sequence of configurations generated by *ab initio* path integral simulations, in Figure 1 of ref 120. Conversely, in the Grotthuss mechanism, contributions from so-called "vehicular diffusion", i.e. hydrodynamic Stokes-like diffusion of long-lived quasi-rigid molecular solvation aggregates, play only a minor role at ambient conditions. It is mentioned in passing that the relative importance of these different contributions depends strongly on temperature and pressure, as seen dramatically, for example, in supercritical water.[131]

The early AIMD simulations[102−104] and the independent theoretical analysis[129] of H^+(aq) were followed by an empirical valence bond study[110] in which a *two-state* EVB model was introduced in order to investigate proton *transfer* between two *specified* water molecules embedded in liquid water (see ref 116 in relation to the parametrization of this particular EVB model). Thus, by construction, the first EVB simulation[110] of a hydrated proton in water refers necessarily to a localized protonic defect that is confined to a particular hydrogen bond and thus unable to undergo structural diffusion. Subsequently, so-called "extended"[112] or "multistate"[115] EVB models were successful in simulating actual proton transport within the three-dimensional hydrogen-bonded water network by allowing for true charge migration via Grotthuss structural diffusion in bulk water.[113−115,117,119] These studies are reviewed in ref 14, where follow-up EVB work is also comprehensively covered. The proton diffusion scenario extracted from such multistate EVB simulations turns out to be similar to that provided by the AIMD simulations and the theoretical analysis.

The specific fluctuations that drive such Grotthuss diffusion in acidic aqueous solutions are in accord with a notion introduced by us[135] (see also refs 16 and 134), which we refer to as the *presolvation concept*. The latter provides a unified mechanistic framework for understanding, at the molecular level, the local fluctuations that must occur in

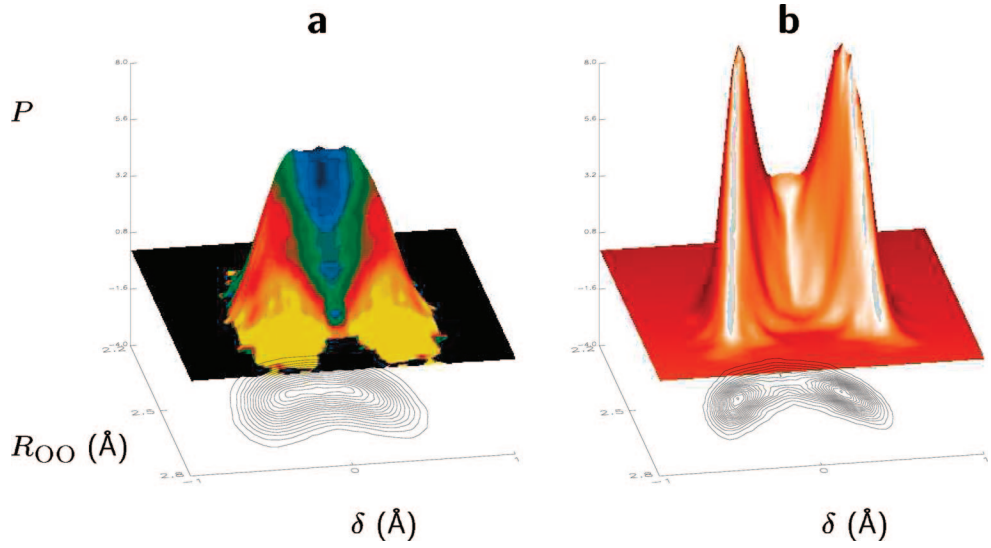

Figure 1. Analysis of the topological charge defect underlying structural diffusion in an acidic solution obtained by adding one excess proton to liquid water, H^+(aq); see section 4 for methodological details. Averaged distribution function $P(\delta, R_{OO})$ as a function of the PT coordinate δ and the oxygen−oxygen separation R_{OO} of the most active HB from canonical AIMD simulations at 300 K where the nuclei are treated as quantum (a) and classical (b) particles; see the caption of Figure 2a and section 5.1 for definitions and labeling conventions. In panel a, the averaged local coordination number, $n(\delta, R_{OO})$, of the *proton-receiving* oxygen, $\bar{O}$, is superimposed on $P(\delta, R_{OO})$. Color code for panel a: n decreases from yellow (≈4) to red to green to blue (≈3.5). All distributions are smoothed and symmetrized about $\delta = 0$, and the $P(\delta, R_{OO})$ distributions in parts a and b are normalized to unity and shown on the same scale. Reprinted with permission from ref 120. Copyright 1999 Nature Publishing Group.

conjunction with the structural diffusion process. This concept has proven robust in its ability to explain structural diffusion in a variety of hydrogen-bonded systems[16,45,46,57,134,135] and, most importantly for the present purpose, to explain why certain proposed models of structural diffusion fail to yield a physically meaningful picture as analyzed in refs 16 and 134. At the core of the presolvation concept is the common notion that bulk water molecules exist in a preferred solvation structure (subject to fluctuations and defects), which, for the purposes of this discussion, we assume to be the accepted 4-fold tetrahedral coordination pattern. This tetrahedral motif has been shown to explain a host of different phenomena related to water and aqueous systems[136,137] (here, we avoid discussion of the experiments and their interpretation presented in ref 138). Most importantly, structural diffusion requires that, in any PT reaction, the proton-receiving species, i.e. the acceptor site, must first have a solvation pattern that corresponds to the species into which it will be transformed as a result of the reaction.

Application of the presolvation concept to H^+(aq) leads to a picture in which PT, and thus the structural diffusion process, is initiated by a HB breaking event between the first and second solvation shell of H_3O^+, thereby reducing the coordination number of a (proton-receiving) water molecule in the first shell from four to three. Since the hydronium oxygen does not accept a hydrogen bond, the reduction in coordination number of the first-solvation shell water places this water molecule in a coordination pattern similar to that of the $H_9O_4^+$ cation itself, thereby allowing the proton to transfer from the hydronium to this water *via* the aforementioned interconversion process. The rate-limiting step in the process is the time needed to effect the coordination number reduction. This time, which correlates with the lifetime of a water−water hydrogen bond, has been estimated from NMR measurements[84,87] to be approximately 1.5 ps. This migration process was first revealed, on the detailed molecular level, in Car−Parrinello AIMD simulations[102−104] more than 15 years ago (see Figure 1 in ref 103 for some snapshots and Figure 1 in ref 120 for a complete sequence). The crucial reduction in coordination number (i.e., $n(\delta, R_{OO})$) of the proton-receiving water molecule (denoted here $\bar{O}$) in the first shell upon PT (i.e., in the limit $\delta \rightarrow 0$ of the PT coordinate) is most beautifully seen (cf. the blue region) in the distribution function reproduced in Figure 1a. The labeling conventions and definitions (i.e., of $\bar{O}$, δ, R_{OO} etc.), as well as the defect localization procedure used throughout this review, are introduced and explained in section 5.1 in conjunction with Figure 2a.

One decade later, the predicted two-step mechanism and the predicted rate-limitation due to solvation shell fluctuations were directly confirmed experimentally[97] using femtosecond vibrational pump−probe spectroscopy: "In the first step, the hydrogen-bond coordination number of one of the H_2O molecules in the first solvation shell is lowered by the breaking of a hydrogen bond to the second solvation shell. [...] In the second step, the protonic charge is transferred from the H_3O^+ ion to the H_2O molecules with the reduced hydrogen-bond coordination number, a process in which the Zundel structure occurs as an intermediate state. Our results show that this second step occurs on an extremely fast time scale. As a consequence, the first step is the rate-limiting one, and the agreement between the solvent reorganization time in water [...] with the proton hopping time [...] confirms this." (quoted from ref 97). Shortly thereafter, and independently from these first Car−Parrinello AIMD simulations[102−104] of Grotthuss diffusion, a molecular mechanism was proposed in ref 106, to which the Car−Parrinello simulation results were suggested to be qualitatively consistent (see also ref 13 and its Addendum). This was derived from a survey of available data in conjunction with a critical analysis of various mechanistic ideas that have been proposed over the years.

Inclusion of nuclear quantum effects[120] using the powerful *ab initio* path integral simulation technique[139−142] (see section 4.4 for more information) provides the full picture. The associated quantum fluctuations have been predicted to lead

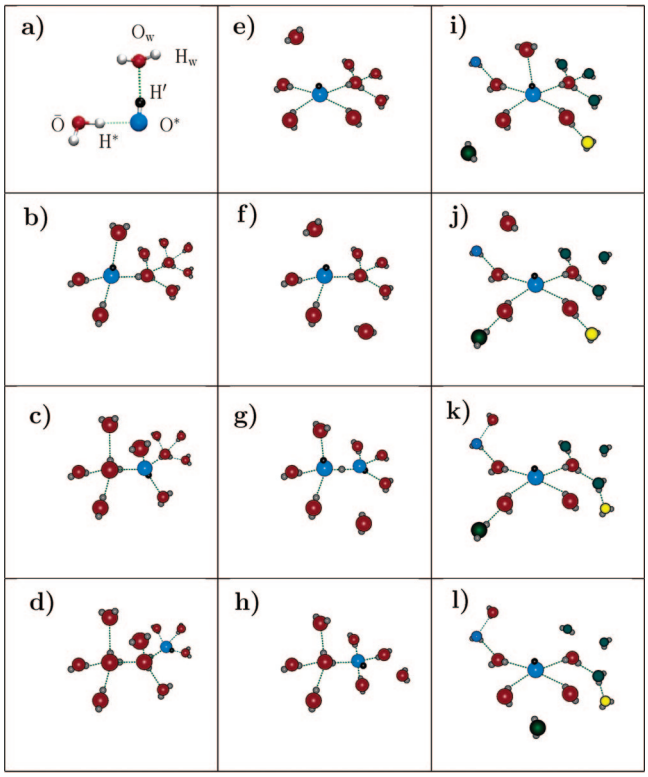

Figure 2. Schematic sketches of the different charge migration mechanisms of OH^- in bulk water, $OH^-(aq)$; see Figure 12 for the corresponding configuration snapshots sampled from trajectories. (a) Labeling convention of the defect site where the PT coordinate is given by $\delta = R_{O^*H^*} - R_{\bar{O}H^*}$ and $R_{OO} = R_{O^*\bar{O}}$ is the oxygen−oxygen distance of the most active HB as defined in the text; see section 5.1. Traditional mirror image mechanism, b−d; dynamical hypercoordination mechanism, e−h; and static hypercoordination mechanism, i−l. In all panels only the local neighborhoods are shown, the defect is highlighted in blue and black, and in i−l, to highlight the vehicular diffusion mechanism, different coloring schemes are used for water molecules in the second solvation shell. Reprinted with permission from ref 16. Copyright 2006 American Chemical Society.

to a topological defect that cannot be characterized entirely in terms of either the Eigen or Zundel structures but approaches these "idealized" structures only as limiting forms, and the term "fluxional complex" was coined to describe this situation.[120] This is compellingly illustrated by comparing AIMD simulations based on classical nuclei shown in Figure 1b to analogous path integral simulations in panel a where the nuclei are treated as quantum particles. In the classical case (b), the probability of finding a protonic defect in Eigen-like configurations (i.e., for $|\delta| \gg 0$) is much higher, as indicated by the clearly visible peaks, than finding the charge defect in Zundel-like configurations (i.e., in the regime $|\delta| \approx 0$); note that $|\delta| \gg 0$ implies that the most active proton is close to a specific water molecule forming a H_3O^+ ion, which is typically solvated by three water molecules in the Eigen cation configuration $H_3O^+ \cdot (H_2O)_3$. $|\delta| \approx 0$ implies that the most active proton is close to the midpoint of its HB, thus yielding the Zundel cation $[H_2O \cdots H \cdots OH_2]^+$. As will be elaborated in section 6.1, this translates into a purely thermal free energy barrier[122] of roughly one k_BT, where Eigen-like complexes are free energy minima and Zundel-like complexes can be thought of as transition states in the classical limit shown in panel b. The situation changes qualitatively after including quantum-mechanical effects of the nuclei as done in panel a of Figure 1: in this case, the probabilities to find the defect in an Eigen-like or Zundel-like configuration are very similar, as seen from the flat and broad ridge that extends from $|\delta| \approx 0$ into the wings. In terms of the free energy landscape, this amounts to washing out the thermal interconversion barrier, i.e. $\Delta F \ll k_BT$, which is mainly achieved by zero-point motion that "fills up the Eigen-wells" (see section 6.1). In terms of mechanism and structure, these quantum effects imply that the Zundel complex is not a transition state and that the defect is highly "fluxional".[120] In other words, PT between two *neighboring* water molecules, which interconverts Eigen-like and Zundel-like structures, is a very fast event and cannot be rate-limiting, in agreement with conclusions drawn from earlier AIMD simulations[102−104] relying on the classical approximation to the nuclear motion. The "fluxionality" of the defect implies that the Zundel and Eigen complexes as well as all "intermediate" complexes are thermodynamically nearly isoenergetic.

Several years after the aforementioned prediction, this aspect of structural diffusion in acids was fully borne out by time-resolved ultrafast spectroscopy,[97] which concluded "[...] that the Eigen and Zundel structures interchange within a very short time (<100 fs), which means that the proton rapidly rattles between the oxygen atoms of two neighboring water molecules. [...] As a consequence, the proton in water forms a "fluxional complex" with the Eigen and Zundel structures as limiting and intermediate conformations, respectively." (quoted from ref 97). Furthermore, as a result of quantum effects, the defect can become delocalized[120] over *several* HBs and hence over several water molecules, a phenomenon driven by fluctuations in the local HB network. Importantly, the quantum fluxionality is the primary reason for the decrease in the free energy difference between typical Eigen-like and Zundel-like complexes and is ascribed primarily to zero-point vibrational motion; proton tunneling appears to play only a negligible role.[120] Indeed, recent attempts to fit neutron diffraction differential cross sections[96] by *either* Eigen-like *or* Zundel-like complexes highlight the difficulty of making a sharp distinction between these two complexes, which strongly supports the aforementioned predicted fluxionality. The basic picture just described may be refined,[98,129,133] e.g. by including more solvation shells in the spirit of the Eucken−Gierer−Wirtz theory,[143,144] which is derived from a cluster-type view of liquid water (using the concept of what the latter authors referred to as "*Aggregate*"[143] or "*Assoziate*"[144] in their work).

Before leaving this section, it is worth noting that an idea similar to the presolvation concept underlies Marcus' theory of electron transfer,[145,146] in which solvent fluctuations must occur that equalize the free energy cost before and after the electron transfer step. Related conceptual approaches have also been developed for adiabatic PT in polar solvents, where, being subject to much stronger coupling, solvent fluctuations are crucial to modulate energy barriers.[147−151] In particular, the picture of presolvating the proton acceptor brings to mind the notion of a change of the adiabatic free energy profile along some appropriately chosen reaction coordinate from an asymmetric shape that favors the proton donor to symmetric one, as suggested in ref 151. This change in the free energy profile is a necessary step before the proton can be transferred successfully to the receiving site. Here, the "symmetrization" of the free energy profile corresponds to the aforementioned change in the coordination pattern of the proton-receiving species. In the presolvation concept, how-

ever, the solvation-shell fluctuations must be of a *very specific structural character* that is dictated by the coordination pattern of the proton-receiving species. Finally, it is noted in passing that the coordination number changes required by the presolvation concept were recently found to be key to the reorientational motion of water molecules in the bulk liquid.[152,153] In these studies, it is found that a water molecule exchanges a hydrogen bond in the network by breaking a HB with a first solvation shell water that is momentarily overcoordinated and forming a HB with a second shell water that is simultaneously momentarily undercoordinated.[152] Interestingly, the change in *average* coordination number, which defines over- and undercoordination with respect to bulk coordination, is about ±0.3 in ref 152. This value is close to the approximately 0.5 found[120] for the coordination number changes that trigger H^+(aq) diffusion, as illustrated in Figure 1a. Thus, even in the case of reorientational relaxation, the presolvation concept, which ultimately requires a restoration of the preferential coordination patterns in the local neighborhood of a topological defect, here orientational rather than ionic, leads to a mechanism that explains the observed dynamics.

3. Structural Diffusion in Aqueous Bases: Current Knowledge, Controversies, and Open Issues

3.1. Some Historical Remarks

Turning now to the structural diffusion mechanism of hydroxide ions in a bulk aqueous environment, OH^-(aq), one finds that the picture is much less clear in comparison to the H^+(aq) case. We first note that the standard free energies of hydration[154] of OH^- and H_3O^+ are very similar, about −106 and −103 kcal/mol, respectively, and quite different from that of H^+, about −264 kcal/mol. Historically, efforts to investigate the OH^-(aq) problem as an *independent question* have been few. The reason for this can be traced back, to the best of our knowledge, to an idea spelled out by Danneel[155] more than a century ago and worked out two decades later in greater quantitative detail by Hückel,[156] by Wannier,[157] and independently, although in less detail, by Bernal and Fowler.[158] Subsequently, Gierer and Wirtz[144] incorporated the (temperature-dependent!) local water structure using modern association and hydrogen bonding concepts and Eucken's "*Aggregate*".[143] The essential idea relies on the assumption that the mechanism of OH^-(aq) transport could be inferred from that of H_3O^+ by invoking pseudo-symmetry arguments. This notion led to the so-called "mirror image" concept, in which H_3O^+ is viewed as a water molecule with an excess proton, while OH^- is regarded as a H_2O with a missing proton ("proton hole");[156] terms such as "*Spiegelbild*" (mirror image) and "*Loch*" (hole) were actually introduced by Wannier.[157]

Within this picture, the structural diffusion mechanisms of the two species, OH^-(aq) and H^+(aq), are related straightforwardly by assuming similar solvation shell topologies. From this starting point, a mechanism of OH^- migration is inferred from that of H_3O^+ by essentially reversing the HB polarities, rotations, and directions of PT, as most clearly illustrated by Figure 3. This particular scenario, as well as closely related ones, have been persistently put forth in the literature for many decades up to the present[4,81−83,144,155−168] (inspect the many suggestive schematic drawings and figures

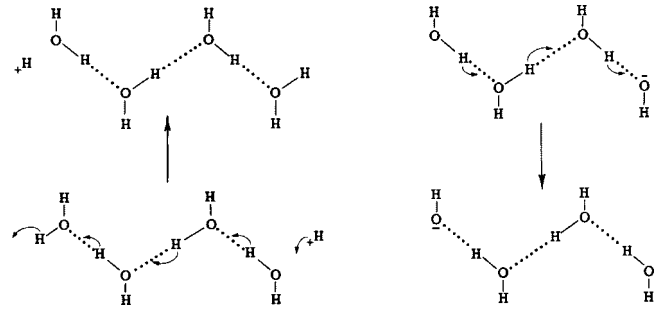

Figure 3. "Left panel (a): Electrical conduction of protons in water, by successive hydrogen shifts along a chain of hydrogen bonds. Right panel (b): Mechanism for hydroxide anion mobility in water. The proton "hole" moves by successive hydrogen shifts akin to those shown in panel (a)" (quoted from ref 163). The authors are grateful to F. H. Stillinger for permission to reproduce these figures, with their captions, from pp 184/185 of his review.[163] Reprinted with permission from ref 163. Copyright 1978 Academic Press/Elsevier.

contained in these publications as mentioned in our bibliographic notes). In one of the more recent accounts, a mirror image or proton hole hopping mechanism for OH^-(aq) migration was worked out in quantitative detail in ref 164, in close analogy to the structural diffusion picture derived earlier for the H^+(aq) case[106] (note that Figure 3 of ref 164, which illustrates the rate-limiting step for OH^-(aq) mobility, is *literally* the mirror image of Figure 2 in the same paper, depicting the rate-limiting step for H^+(aq) mobility according to ref 106). In this picture, OH^- *accepts three* HBs and *donates none*, thus forming the $OH^-\cdot(H_2O)_3$ or $H_7O_4^-$ anion. Structural diffusion is driven predominantly by the same type of second solvation shell effects that drive H^+(aq) migration. These fluctuations lead to the formation of an intermediate $H_3O_2^-$ complex that is analogous to the $H_5O_2^+$ (Zundel) complex of the H^+(aq) case and is only slighly less stable than $H_7O_4^-$ (see refs 169, 162, and 170 for some infrared (IR) spectroscopic analyses carried out along these lines). Within this scenario,[164] "A suggested mechanism for hydroxide mobility in water identifies the rate limiting step as a cleavage of a second shell hydrogen bond which converts a $H_7O_4^-$ ion (triply coordinated hydroxide) to $(HOHOH)^-$ (deprotonated water dimer)." (quoted from ref 164). "The present section argues that the dominant stable isomers of the hydroxide ion in liquid water are the $H_7O_4^-$ and $H_3O_2^-$ ions." (quoted from ref 164). "The suggested mechanism of hydroxide mobility is similar to that of proton mobility in water, except for the small difference in the O−O distance within the dimer, which might explain the perplexing observations in the literature." (quoted from ref 164). "Hydroxide mobility resembles proton mobility because the rate limiting step, which contributes most of the activation barrier, is a cleavage of a second shell hydrogen bond. It converts a deprotonated (protonated) water monomer to a deprotonated (protonated) water dimer, allowing the diffusing hydroxide-ion (proton) to delocalize over two oxygen centers. However, the O−O distance for the deprotonated dimer is slightly larger than that of the protonated dimer. [...]" (quoted from ref 164).

To the best of our knowledge, the only source in the early literature where this symmetry argument, and thus, by inference, the mirror image concept, has been seriously questioned is an insightful, yet essentially forgotten, historic paper by Huggins[171] from 1936; see, however, section III.4, "*Die Arbeit von Huggins*", in ref 144 for a lucid discussion of the conceptual importance of ref 171, which culminates

in the statement that Huggins' viewpoint, although qualitative, best acknowledges the importance of hydrogen bonding for anomalous conductivity (termed "*Extraleitfähigkeit*") and thus for structural diffusion in H^+(aq) and OH^-(aq) solutions. In Huggins' paper,[171] it is argued that the solvation shell of OH^-(aq) very likely differs *qualitatively* from that of H^+(aq). It is worth noting that this argument appears to differ from an earlier view expressed by him in ref 159. If Huggins' later argument retained its validity, the charge migration mechanism would be affected at a *qualitative* level. Here again, the presolvation concept serves as a useful guide, a point that is clearly illustrated in the proceeding three sections. Interestingly, Wannier himself stressed that the values of the temperature-independent microscopic input parameters obtained by fitting his theory to a combination of temperature-dependent experimental observables turned out to be very similar for both positive and negative charge defects.[157] He, therefore, concluded that the observed differences between the H^+(aq) and OH^-(aq) systems, which were evident from the known experimental data at that time, could not be explained by his (mirror image) theory (see details in the bibliographic notes[157]). Finally, there is a more recent analysis[172] (it has been cited only four times according to the *Web of Science* as of October 2009), which points out "...that the commonly used schematic representation of the $OH^{\ominus}$ conductance mechanism in aqueous solution is not the analogue of the corresponding diagrams for the $H^{\oplus}$ ion." (quoted from ref 172).

Presumably because of the intuitive appeal of the mirror image picture, it has taken several decades for researchers to undertake a serious investigation of the structure and mobility of OH^-(aq) in its own right. In the last ten years, however, there has emerged a wealth of theoretical[15,16,30,69,102−104,134,135,164,166,167,173−185] and experimental[67,68,99,184,186−206] investigations into OH^-(aq) structure and mobility (including several relatively large microsolvated $OH^-\cdot(H_2O)_n$ clusters studies), and these have sparked a serious controversy about both the solvation pattern of OH^-(aq) and its microscopic transport mechanism. The origin of the controversy can be traced back to the pioneering AIMD simulations of both the H^+(aq) and OH^-(aq) systems[102−104] and a wealth of subsequent computer simulation studies of OH^-(aq)[16,69,102−104,134,135,178−180,182,184] which provided strong evidence that the oxygen site in OH^- prefers to be *hypercoordinated*[135] in liquid water by *accepting four* HBs. Furthermore, OH^- has been shown to *donate transiently one* HB *via* its hydroxyl hydrogen when fully solvated in bulk water. Based on earlier work[102−104] and subsequent *ab initio* path-integral simulations,[135] a novel "dynamical hypercoordination" mechanism was proposed and depicted for the first time in Figure 3 of ref 135; see also the *Highlight Article*.[15] As argued in refs 16 and 134, this mechanism can be seen to differ strongly from the traditional mirror image mechanism. We mention in passing that the notion of hypercoordination as introduced in ref 135 for OH^-(aq) pertains to (noncovalent) hydrogen bonding and solvation structure is distinctly different from hypervalency[207−210] in the sense of (covalent) chemical bonding and molecular structure; the oxygen atom in the dynamical hypercoordination mechanism should by no means be considered as "pentavalent".[211]

In the remainder of this section, the different structural and mechanistic proposals that can be found in the literature will be presented and critically examined by comparing them to each other within a unified framework. Importantly, applying the presolvation concept introduced for H^+(aq) to the OH^-(aq) case allows several possible charge migration mechanisms to be derived depending on the preferred OH^-(aq) coordination state. This intimate connection between solvation patterns and diffusion mechanisms is extremely valuable in view of a series of very recent diffraction and spectroscopic experiments[67,68,99,184,197−205] that yield detailed and consistent information about the solvation shell of OH^-(aq). In the subsequent parts of this section, convincing evidence is provided that only one of the proposed scenarios is consistent with what is currently known from experiment. In particular, both hypercoordination of the oxygen site and the ability of OH^-(aq) to donate a HB *via* the hydroxyl hydrogen, as predicted by the aforementioned AIMD simulations,[16,102−104,134,135] are strongly supported by these state-of-the-art experiments in the condensed phase. However, experiments that provide the most direct mechanistic insights into the migration of OH^-(aq) using time-dependent probes, which have been applied successfully for the H^+(aq) case,[92,95,97,98,101] are still lacking. Fortunately, this gap can be closed by analyzing the detailed mechanism obtained from different computer simulation approaches that yield different preferred coordination patterns of OH^-(aq). Such analyses will be discussed in section 5 after the underlying techniques have been described (see section 4). Important issues related to solvation and diffusion, such as quantum effects due to nuclear motion, condensed phase solvation versus microsolvation, and the possible influence of counterions and concentration, are discussed in section 6. When viewed against well-known mobility experiments, which yield diffusion coefficients of both H^+(aq) and OH^-(aq), all of the analyses to be presented strongly favor the novel dynamical hypercoordination mechanism over the traditional mirror image picture as the only mechanism consistent with the recent diffraction and spectroscopic data.

3.2. Mirror Image/Proton Hole-like Scenarios

The traditional view[4,82,83,144,155−158,162,163] and several recent analyses[164,166,167] of the hydrated hydroxide anion have led to the suggestion that the OH^- oxygen favors 3-fold coordination of the oxygen of OH^-(aq) in aqueous solution. In particular, "Three distinct lines of investigation [...] converge on the common view that $HO\cdot[H_2O]_3^-$ is a prominent, likely even dominating, coordination structure for HO^-(aq); this is the most primitive issue underlying current speculations regarding HO^- in aqueous solutions." (quoted from ref 167) and "The present results suggest a picture that is simpler, more traditional, but with additional subtlety. These coordination structures are labile but the tricoordinate species is the prominent case. [...] No evidence is found for rate-determining activated interconversion of a $HO\cdot[H_2O]_4^-$ trap structure to a $HO\cdot[H_2O]_3^-$ mediating hydroxide transport. The view of HO^- diffusion as the hopping of a proton hole has substantial validity, with the rate depending largely on the dynamic disorder of the water hydrogen-bond network." (quoted from ref 167). The recent work is based on a survey and synthesis of available data and concepts,[164] quasichemical theory,[166,212] and AIMD simulations,[167] as well as on some experiments on $OH^-\cdot(H_2O)_n$ microsolvated clusters in the gas phase.[187,192,195] Let us assume for the moment that this solvation pattern were to hold *in the bulk*. Under this assumption, two possible mechanisms could be derived from the presolvation concept. If the OH^- hydrogen

does not donate a HB, as assumed implicitly in ref 164, then the 3-fold coordinated OH^-(aq) would indeed behave as a mirror image[4,82,83,144,155−158,161−165,168] of the H^+(aq) case. In this case, fluctuations would break a HB between the first and second solvation shell of OH^-(aq), thereby reducing the coordination number of a first-shell water of OH^- from four to three[164] (water molecules "a" and "c" in Figure 3 of ref 164 are these first and second shell molecules, respectively). The obvious difficulty with this picture is that the nascent water molecule formed in the PT step does not possess the favored 4-fold tetrahedral water coordination pattern. Furthermore, it is unclear how this nascent water molecule relaxes in order to acquire the preferred coordination of a typical water molecule in the equilibrium bulk liquid.

It should be noted in this context that observed differences between IR and Raman spectra of concentrated basic solutions[213] have been suggested as providing evidence in favor of the mirror image picture. The observed differences were attributed to the structure and purported stability of the $H_3O_2^-$ complex in aqueous basic solutions (see also refs 162, 169, and 170 for some IR-spectroscopic analyses carried out along these lines). However, the use of such spectroscopic data to *directly* confirm or refute this picture is highly subtle. We will discuss this aspect in detail later in section 6.3; however, we briefly note here that explicit AIMD simulations of concentrated KOD and NaOD solutions[178−180] support the aforementioned hypercoordinated picture over the mirror image picture and, furthermore, are able to reproduce the experimental IR spectra of ref 213.

Another mechanism could be derived if the OH^- oxygen were to favor 3-fold coordination *and* the OH^- hydrogen *could* donate a HB, in close analogy with the classic Lewis-like or localized molecular orbital picture. In this case, the OH^-, being the proton-receiving species in bases, would naturally possess a coordination pattern like that of a bulk water molecule as depicted in Figure 2b. A solvation pattern such as this for OH^-(aq) would lead, according to the presolvation concept, to unhindered proton transfer from an accepted water molecule in the first solvation shell to the neighboring OH^- (see step (b) → (c) in Figure 2). Once shifted to the respective neighboring site, the OH^- would, again, be perfectly coordinated and, thus, would again be ready for a subsequent PT from a neighboring water molecule from which a HB is accepted. In this way, charge migration would occur with no rate-limiting step apart from fast local reorientations (see step (c) → (d) in Figure 2). The consequence of such a mechanism[167] would be an extraordinarily high structural diffusion rate, possibly exceeding that of H^+(aq), according to presolvation analysis.

3.3. Dynamical Hypercoordination Scenario

In contrast to the scenarios discussed in the previous section, several AIMD computer simulation studies[16,69,102−104,134,135,178−180,182,184] suggest that the oxygen in OH^-, being the proton-receiving species in aqueous bases, is, on average, *hypercoordinated*;[135] that is, it preferentially *accepts four* HBs in a roughly square-planar arrangement (shown for the first time in Figure 2 of ref 102). This preferred complex of the OH^-(aq) defect is depicted in Figure 4a together with its electron localization function (ELF);[214] the ELF takes on values between zero and one and is large in those regions of real space where two electrons with antiparallel spin are *paired*, thus forming covalent bonds or lone pairs.[214] This solvation shell is qualitatively different

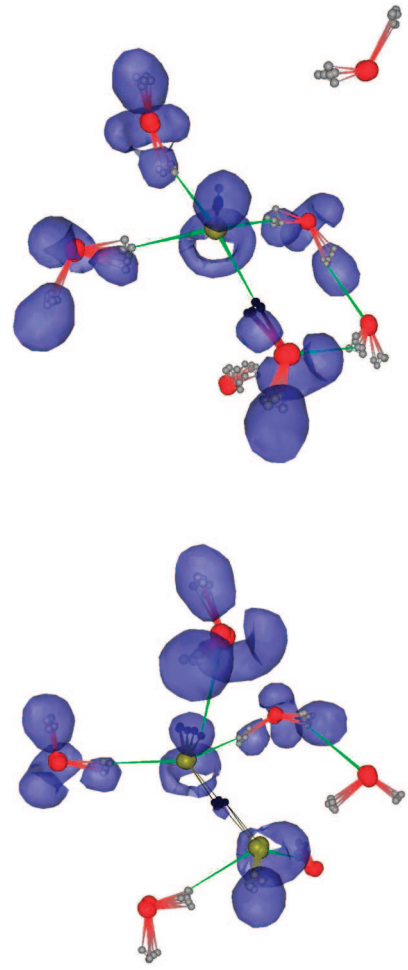

Figure 4. Representative resting and active states of OH^- in bulk water, OH^-(aq), within the dynamical hypercoordination mechanism;[135] note that only the most relevant molecules are depicted. The resting state (a, top) is the majority complex, with four hydrogen bonds accepted by O* in an essentially *square-planar* arrangement; note that the water molecule $(H_2O)_w$ closest to H′, in the upper right corner, is not hydrogen bonded. The active state (b, bottom) is a short-lived transient complex with three hydrogen bonds accepted by O* and an additional hydrogen bond donated by H′ in a locally *tetrahedral* arrangement; here, this complex is captured close to proton transfer (i.e., $|\delta| \approx 0$), where H* is roughly midway between the proton donor $\bar{O}$ and the proton acceptor O*. The special atoms H*, O*, and $\bar{O}$ are highlighted in black and yellow, respectively, the hydrogen bonds are marked schematically in green, and the blue clouds are isosurfaces of the electron localization function;[214] see the caption of Figure 2a and section 5.1 for definitions and labeling conventions. In addition, quantum effects such as librations of individual water molecules can be identified by the delocalization of the nuclei within the underlying *ab initio* path integral technique (see section 4.4). Reprinted with permission from ref 135. Copyright 2002 Nature Publishing Group.

from what would be deduced on the basis of either the traditional Lewis-type picture of hydrogen bonding or the localized molecular orbitals (as obtained, for instance, by applying the Boys localization criterion). These approaches invariably predict one covalent O−H bond and three lone pairs around the oxygen site of an isolated OH^- anion in vacuum. Based on these concepts, one would argue that OH^-(aq) should *accept three* HBs *via* its three lone pairs, with the possibility of donating a HB *via* its hydrogen end. Instead, the origin of the hypercoordination phenomenon arises from a substantial delocalization of the lone pairs,[135] leading to a "ring" of enhanced *electron pairing* probability,

the plane of which is perpendicular to the OH^- bond axis and lies just below the oxygen. This phenomenon can be quantified with the help of the ELF[214] as visualized in Figure 4a, which clearly reveals a ring attractor at the base of the central OH^- ion. This cylindrically symmetric pattern around the O−H bond axis is also in accord with the symmetry of the electrostatic potential as created by OH^- in vacuum and is also seen in both the ELF of OH^- in vacuum[215] and in the spatial distribution functions around OH^- basic solutions derived from neutron scattering.[197] Based on this electronic structure analysis, there is *no* reason to assume that OH^- can accept a maximum of three HBs or that accepting three HBs should be its preferred solvation pattern in liquid water.

The plausibility of hydroxyl oxygen hypercoordination in solution suggests that structural diffusion of $OH^-(aq)$ should differ *qualitatively* from that of $H^+(aq)$ and its mirror image according to the schemes sketched in Figure 2. If hypercoordination holds, the initial step in the structural diffusion process, according to the presolvation concept, must be a reduction in the coordination number of the $OH^-(aq)$ itself by breaking a HB between its oxygen and a *first shell* water molecule according to steps (e) → (f) of Figure 2. Only this type of event will leave the OH^- *oxygen* in a topology similar to that of a water molecule in bulk water. However, the presolvation concept requires that the topology of the *full* coordination shell of OH^- resemble that of a water molecule, which requires that the hydroxyl hydrogen be able to donate a HB, even if only transiently. Thus, according to the presolvation idea, PT to OH^- can only be completed in an isotropic bulk environment when OH^- also donates a HB to a neighboring water molecule through its *hydrogen* end (see step (f) → (g) in Figure 2). Indeed, the combination of the coordination number reduction around the hydroxyl oxygen and the donation of a HB through the hydroxyl hydrogen places the hydroxide ion in the solvation pattern of a bulk water molecule, a locally tetrahedral arrangement, which is a short-lived transient complex. As the proton is transferred (panel b of Figure 4), i.e. upon transformation of OH^- into an intact water molecule, the donated HB strengthens and leaves the nascent H_2O molecule with two accepted and two donated HBs, as required for an ideally coordinated water molecule in the bulk liquid (see step (g) → (h) in Figure 2). In the proton-transfer process, the electronic structure around the defect changes in a subtle way: in Figure 4b the ELF ring attractor around the proton-receiving OH^- opens up and yields two (partially) localized lone pairs as the OH^- is transformed into an intact water molecule. At the same time, the two lone pairs on the proton-donating water molecule are confluent and begin to form a delocalized ring attractor as this water is transformed into the nascent OH^-. In this charge migration scenario, the rate-limiting step is the time needed for the coordination change and the relaxation into a tetrahedral configuration. This nontraditional mechanism (see panels i−l in Figure 2 for a rough scheme and the same panels in Figure 12 for the corresponding configuration snapshot sequence from computer simulation), which we call the "dynamical hypercoordination" mechanism hereafter, was depicted for the first time in Figure 3 of ref 135 based on earlier work.[102−104]

3.4. Static Hypercoordination Scenario

In addition to the mirror image and dynamical hypercoordination pictures, a purely vehicular diffusion mechanism is also conceivable. Based on the evidence provided previously, we could envision a scenario in which the hypercoordinated solvation pattern of $OH^-(aq)$ exists as a static, rigid structure, as shown in Figure 2i rather than a dynamical one.[16,103,104,134,135] Let us now apply the presolvation concept to this picture. It should be clear that a purely vehicular diffusion mechanism must occur preferentially in a static hypercoordinated structure, since this structure is inactive with respect to PT, as the above discussion suggests. Hence, if the oxygen of $OH^-(aq)$ accepts four HBs in a square-planar arrangement and maintains this coordination, then it never attains the proper solvation pattern it would need to receive a proton from a neighboring water molecule. This conclusion remains even if the hydroxyl hydrogen is able to donate a HB. Thus, OH^- could be viewed, in this case, as any simple anion with a tighly bound first solvation shell $[OH^- \cdot (H_2O)_4](aq)$. According to this picture, the only possible diffusion mechanism involves *second* solvation shell changes due to HB fluctuations in the third shell and beyond, as sketched in panels (j) → (k) → (l) in Figure 2. This implies that diffusion would mostly occur hydrodynamically *via* the vehicular Stokes mechanism, whereas PT and thus structural diffusion would be unlikely events. Thus, not only is *static* hypercoordination insufficient to describe structural diffusion, it actually hinders the process! We conclude, therefore, that the hypercoordinated structure must be *dynamical*, as discussed in the previous subsection, so that it can devolve to a lower coordination state by breaking a first-shell HB.

3.5. Experimental Facts versus Virtual Reality

As noted earlier, state-of-the-art computer simulation techniques provide a window into the microscopic motions of individual atoms and molecules in a chemical process. Simulations allow the trajectory of every atom to be followed in both space and time, much like Maxwell's Demon, and thus yield the microscopic details of the resulting structural diffusion mechanism and underlying solvation shell structures and their dynamics. In particular, the method of AIMD simulation, which combines finite-temperature MD with forces computed "on the fly" from electronic structure calculations based on density functional theory, is a powerful approach for investigating these mechanistic questions (see section 4). By virtue of the Born−Oppenheimer approximation, AIMD calculations also yield the ground-state electron distribution at each step of the calculations, thereby allowing a variety of electronic properties to be computed. Still, any feasible simulation of such complex processes in the condensed phase relies on approximations, and indeed, different simulation protocols have predicted several different structural diffusion scenarios, including mirror image, dynamical hypercoordination, and static hypercoordination mechanisms, as well as qualitatively different solvation shells of $OH^-(aq)$, as reviewed in the previous sections. Current experiments, on the other hand, are also limited in their ability to combine sub-Ångstrøm resolution in space (such as provided by diffraction techniques) with subpicosecond resolution in time (as accessible by ultrafast spectroscopies). However, by combining state-of-the-art simulation results with state-of-the-art experimental data, it is possible to *sort out consistent from inconsistent scenarios* when using the full set of data available from experiment; this is the strategy followed herein.

An early but weak indication of a rather high hydration number of $OH^-(aq)$ was reported based on dielectric relaxation experiments[189] of aqueous NaOH solutions, yield-

ing an extrapolated "effective hydration number" of 5.5 ± 0.5 in the limit of vanishing concentration. However, this cannot be considered as providing definitive support of hypercoordination, since it is well-known to be very difficult to interpret such hydrodynamic solvation numbers in terms of coordination numbers or hydrogen bonding patterns obtained from both diffraction experiments and computer simulations,[216,217] as already stressed in ref 135.

Later, a comprehensive series of neutron scattering experiments[196−200] of various alkali solutions as a function of concentration was launched.[191] This systematic investigation provided strong evidence for the dynamical hypercoordination predicted earlier in AIMD simulations.[102−104,135,178−180] In particular, the data[196] obtained with an aqueous 4.6 M NaOH solution were found to be compatible with the presence of hypercoordinated (though nonplanar) hydrogen-bonded complexes, $H_9O_5^-$, yielding a first peak at $r \approx 2.3$ Å in the oxygen−oxygen radial distribution function. This value should be compared to approximately 2.8 Å in the corresponding water−water function of this solution. The coordination number of the hydroxide ion, obtained by integrating the radial distribution function, was found to be 3.7 ± 0.3, corresponding to between three and four strongly bound first neighboring water molecules per hydroxide oxygen. Note that this coordination number has been revised to 3.9 ± 0.3 according to ref 197 (see footnote 53 in this publication) using configurations generated by EPSR instead of straightforward integration of the radial distribution function, as had been done previously in ref 196. In addition to providing evidence for about *four* accepted water molecules, the data[196] revealed the presence of a fifth water molecule that is weakly hydrogen-bonded to the hydroxyl hydrogen site at an oxygen−oxygen distance between 2.75 and 3.20 Å with respect to the OH^- ion. This leads to about *one* (1.0 ± 0.2) water molecule at a distance from the hydroxyl hydrogen site between 1.77 and 2.22 Å (see also ref 199).

The concentration dependence of the solvation shell was subsequently investigated[197] for NaOH:H_2O molar ratios of 1:12 (a concentration of 4.6 M), 1:9, and 1:6 and the high concentration of 1:3. As expected, the solvation number decreases from 3.9 ± 0.3 tightly bound water molecules for 1:12 and 1:9 solute:solvent molecules to 3.5 ± 0.3 and 2.9 ± 0.3 when the solute concentration goes up to 1:6 or 1:3, respectively. However, the spatial distribution functions for water molecules around the hydroxide remain nearly *invariant*, thus suggesting that only the population of the hydration shell changes as a function of concentration, but *not* its structure.[197] Nevertheless, it must be stressed that, based on this analysis, the four HBs accepted by OH^- are not coplanar. Most interestingly, when the partial radial distribution function corresponding to a fifth first shell water molecule near the hydroxyl hydrogen is integrated, the number of water molecules obtained remains one at all concentrations studied! In addition, although this fifth molecule on top of the hydroxide does not form a typical HB, it nevertheless features orientational correlations, as quantified by the orientation of its dipole moment with respect to the O−H axis of the hydroxide ion. This property is also found to be reproducible at all concentrations studied[197] (see also ref 199). In order to investigate the behavior of a more dilute solution, the concentration of hydroxide was decreased further using a 2 M NaOH solution. At this molarity, there is about one OH^- per 28 water molecules,[200] confirming and extending the trends revealed earlier.[197] At this low concentration, not only are cations and anions both fully hydrated, but there is also a sufficient number of water molecules present beyond the first hydration shell, as confirmed by the data.[200] This OH^-:water ratio is close to one OH^- per 31 water molecules, a ratio commonly used in previous AIMD simulations (subject to periodic boundary conditions).[16,102−104,134,135] In addition, a significantly lower concentration of 1:63 (unpublished data, but see Figures 5, 6a, and 7a and Tables 1 and 5 in this review) was investigated in refs 16 and 134 using AIMD. Experimentally, the shape of the hydroxide hydration shell is again found to be independent of concentration in ref 200; the number of strongly hydrogen-bonded water molecules increases from 3.9 in the 1:12 and 1:9 solutions[197] to 4.2, and there is still exactly one additional weakly bound water molecule beyond this tight shell. As a result of these observations, it has even been suggested that the peculiar hypercoordinated solvation pattern of OH^-(aq) could be exploited to probe the water dynamics.[201] Finally, the possible influence of different alkali counterions, in particular Li^+, Na^+, and K^+, on the hypercoordination of OH^-(aq) was assessed systematically in ref 198 using solute/solvent concentrations ranging from 1:3 down to 1:12. It was found that varying the counterion does not affect the overall shape of both the radial and spatial distribution functions, thus confirming the earlier conclusions.[196,197]

More recently, a joint X-ray diffraction and MD study[184] of aqueous NaOH solutions of varying concentration concluded that traditional molecular dynamics based on standard OH^-/water nonpolarizable force fields fail to reproduce the experimentally determined bulk structure; it is noted here only in passing that more sophisticated approaches such as polarizable force fields,[185] the "charged ring" force field,[183] multistate EVB models,[30] and a combination thereof[206] are more promising in describing OH^-(aq), *vide infra*. In stark contrast, AIMD is found in this study to be a suitable tool for the detailed interpretation of the hydration sphere of both the anions and cations as well as the solutions' bulk structure, as extracted from X-ray diffraction. In particular, this joint study supports both hypercoordination of the hydroxide anion in basic solutions and its ability to also donate a hydrogen bond *via* hydration of the hydroxyl hydrogen.[184]

In summary, the data extracted from the aforementioned diffraction experiments[184,196−200] strongly support the picture that OH^-(aq) does indeed prefer to accept four HBs. Neutron diffraction predicts that the respective water molecules are noncoplanar whereas AIMD predicts a predominantly square-planar arrangement, as depicted in Figure 4a. In addition, the diffraction data give clear evidence for a fifth, weak bond donated by the OH^- hydrogen. Based on these investigations, ref 198 draws the following conclusion: "It is demonstrated that the symmetry argument between H^+ and OH^- [*i.e. the mirror image concept*] cannot be used, at least in the liquid phase at such high concentrations, for determining the hydroxide hydration shell." (quoted from ref 198).

In addition to neutron and X-ray diffraction, the most recent investigations using spectroscopic techniques yield complementary support of an OH^-(aq) solvation shell in the spirit of dynamical hypercoordination. Fourier transform infrared (FTIR) spectroscopy of the OD band stemming from HDO isotopically diluted in H_2O was employed to investigate selected alkali metal hydroxide solutions.[202,203] No evidence was found for the existence of a stable $H_3O_2^-$ complex in these basic solutions, which is consistent with the short-lived

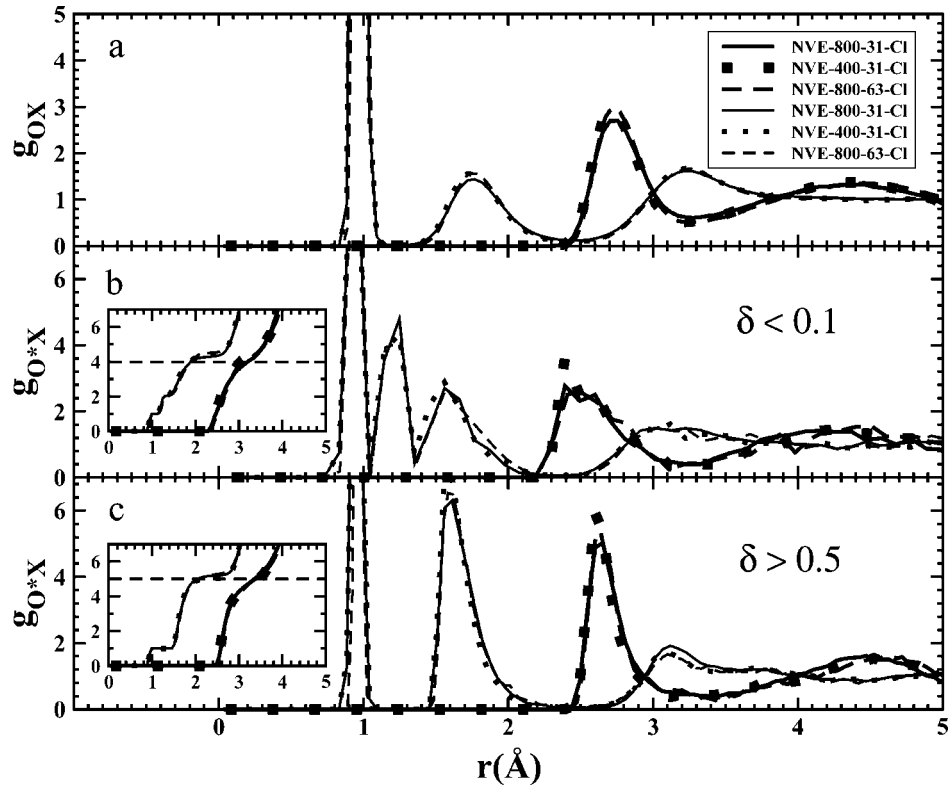

Figure 5. Radial distribution functions, $g(r)$, of OH^-(aq) predicted by the dynamical hypercoordination mechanism with reference to all oxygen atoms (a, top), O* for $|\delta| \leq 0.1$ Å (b, center), and O* for $|\delta| \geq 0.5$ Å (c, bottom), where thick and thin lines refer to X = O and X = H partner atoms, respectively; see the caption of Figure 2a and section 5.1 for definitions and labeling conventions. The insets in parts b and c show the corresponding running coordination numbers, $n(r)$, where the dashed horizontal lines mark the preferred total coordination numbers of four and five water molecules in the first solvation shell of O* in the active ($|\delta| \leq 0.1$ Å) and resting ($|\delta| \geq 0.5$ Å) states, respectively. Standard parameter setting, solid lines; half the fictitious electron mass, dotted lines; double the system size, dashed lines. Based on data from refs 16 and 134.

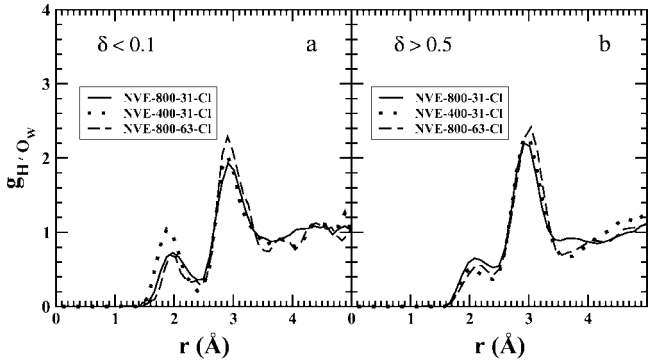

Figure 6. Radial distribution functions, $g(r)$, of OH^-(aq) predicted by the dynamical hypercoordination mechanism of $H'O_w$ for $|\delta| \leq 0.1$ Å (a, left) and $|\delta| \geq 0.5$ Å (b, right); see caption of Figure 2a and section 5.1 for definitions and labeling conventions. Left panel (a): standard parameter setting, solid line; half the fictitious electron mass, dotted line; double the system size, dashed line. Right panel (b): standard parameter setting, solid line; classical canonical ensemble, dotted line; quantum canonical ensemble, dashed line. Based on data from refs 16, 134, and 135.

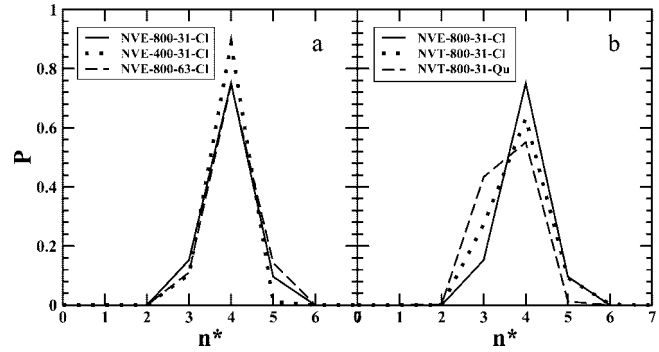

Figure 7. (a, left) Hydrogen bond probability distributions of OH^-(aq) predicted by the dynamical hypercoordination mechanism involving O* as acceptor, $P(n^*)$, comparing standard parameter settings (solid line), half the fictitious electron mass (dotted line), and double the system size (dashed line), all in the classical microcanonical ensemble. (b, right) Same $P(n^*)$ distribution as in part a but comparing standard (classical microcanonical) parameter settings (solid line), a classical canonical ensemble (dotted line), and a quantum canonical ensemble (dashed line). Based on data from refs 16, 134, and 135.

transient solvation complex according to the dynamical hypercoordination mechanism. The existence of a weak interaction with a single water molecule at the hydrogen site of OH^-, i.e. the donated hydrogen bond by the hydroxyl hydrogen required in dynamical hypercoordination, was confirmed by the FTIR spectral data as well.[202] Furthermore, X-ray absorption spectroscopy of aqueous KOH solutions has been carried out at two concentrations.[204] Comparison between the experimental data and *ab initio* calculations suggests that hydroxide exists in a hypercoordinated solvation state with respect to the number of accepted hydrogen bonds; however, it is clearly spelled out that unambiguous identification was not possible at that time.[204]

The interaction of hydroxide with solvation water was studied directly using core-level photoelectron emission spectroscopy in a jet of NaOH and KOH aqueous solution.[205] Exploiting the phenomenon of "intermolecular Coulombic decay" (ICD), it was shown that the hydrated hydroxide anion behaves very differently from more typical anions such

Table 1. Diffusion Coefficients in Units of 10^{-9} m^2/s (corresponding to units of 10^{-1} $Å^2/ps$) Obtained from the Slopes of the Mean-Square Displacements Obtained from the Dynamical Hypercoordination Mechanism Comparing a Larger System Size N and a Smaller Fictitious Electron Mass μ to the Standard Parameter Setting ($N = 31$ water molecules and $\mu = 800$ a.u.) Reported in the Second Column[a]

quantity	$N = 31/\mu = 800$	$N = 63$	$\mu = 400$
D_{OH^-}	1.92	1.02	2.53
$D_{H_2O}^{separate}$	0.25		
$D_{H_2O}^{same}$	0.47	0.40	0.48
$D_{OH^-}/D_{H_2O}^{same}$	4.09	2.55	5.27

[a] Note that the deuterium mass is used for H throughout. The data $D_{H_2O}^{separate}$ are obtained from separate pure bulk water runs (only available for $N = 31$ with $\mu = 800$), and $D_{H_2O}^{same}$ are obtained from the dynamics of the tagged "nonsolvation shell water molecules" in the simulations that include the hydroxide ion defect. Based on data from ref 16.

as the halides F^-(aq) and Cl^-(aq) in terms of solvation-shell structure. In particular, OH^-(aq) is capable of *transiently donating* a hydrogen bond to surrounding water molecules: "This is indeed observed experimentally, and directly confirms that hydration of OH^- involves different types of hydrogen bonds. No such distinction exists for the halide anions, which are hydrogen-bond acceptors only. We conclude that the resonance spectral structure observed in this study must be a microscopic signature of the OH^-(aq) hydrogen-bond donor." (quoted from ref 205). Thus, in agreement with other recent experimental studies of aqueous hydroxide solutions, the findings in ref 205 support the notion that the (dynamically hypercoordinated) hydration structure of OH^-(aq) cannot be inferred from that of the hydrated excess proton.[205] In particular, "A direct and model-independent consequence of this interpretation of the unique spectral features is that it calls for a OH^-(aq) hydration pattern similar to the one invoked[4,5] [*these references correspond to refs 16 and 135 in this review*] in one of the two competing mechanisms [*i.e. dynamical hypercoordination according to section 3.3*] put forward to explain the anomalously fast transport of OH^- in aqueous solution." (quoted from ref 205); "The alternative transport mechanism is based on the "proton-hole" concept[2,21] [*these references correspond to refs 164 and 167 in this review*], which treats the hydroxide ion as a water molecule with a missing proton and OH^- transport as the mirror image process of proton structural diffusion. [...] Our findings are not in agreement with the predictions of the proton-hole concept." (quoted from ref 205); and finally, "As noted above, a plethora of experimental data support the presence of different coexisting OH^- hydration structures in aqueous solution as demanded by the first of the OH^- transport mechanisms [*i.e. dynamical hypercoordination according to section 3.3*] discussed." (quoted from ref 205).

Most recently, femtosecond pump−probe and two-dimensional IR experiments have been applied in conjunction with computer simulation to probe the O−H stretch of dilute HDO in aqueous solutions of NaOD dissolved in heavy water.[206] The solutions range in concentration from 2.6 to 10.6 M NaOD in D_2O, which corresponds roughly to the concentrations used in neutron diffraction experiments,[197−200] and the amount of H_2O dopant was only about 1 vol %. These time-resolved experiments[206] provide detailed insights into the lifetime of the intermediate $H_3O_2^-$ complex, $[HO\cdots H\cdots OH]^-$, in basic solution, which is the mirror image analogue of the $H_5O_2^+$ (Zundel) complex, $[H_2O\cdots H\cdots OH_2]^+$, in acidic solution. In particular,[206] these "results show the fleeting existence of Zundel-like $H_3O_2^-$ states that arise in the course of structural diffusion of the hydroxide ion" (quoted from ref 206) and they furthermore "indicate that this state exists transiently for 2−3 vibrational periods during the transfer of the proton" (quoted from ref 206). Interestingly, based on the accompanying simulations (based on an empirical valence bond model developed from the "charged ring" force field model[183]), it is suggested that the collective electric field in the direction of PT is a better order parameter than coordination numbers for describing the dynamics of the Zundel-like state. These authors[206] also state, in reference to recent Car−Parrinello calculations,[134] "These simulations found 2 principal time scales that contribute to the proton transfer rate, a fast time scale of 180 fs that corresponds to 'proton rattling' events in which the proton returns to the original oxygen atom after a series of PT events within a Zundel-like state, and a slower 1.7-ps process that acts to gate the formation of Zundel-like configurations (10) [*this reference corresponds to ref 134 in this review*]. Given that the simulations use a fully deuterated bath, the time scale for proton rattling agrees well with our experimentally observed value of 110 fs." (quoted from ref 206). Thus, vibrational spectroscopy confirms the *transient nature* of the Zundel-analogue complex, $H_3O_2^-$, which accords well with the presence of a maximum (or saddle-point in higher dimensions) at $\delta \approx 0$ on the free energy profile along the PT coordinate δ, as depicted in the upper left panel of Figure 18 and in Figure 23 (to be discussed in detail at a later stage). The transient existence of these $[HO\cdots H\cdots OH]^-$ complexes is a distinct feature of the dynamical hypercoordination mechanism, as shown in the lower panel of Figure 4. By contrast, in the mirror image picture, the $H_3O_2^-$ complex is predicted to be a stable state in OH^-(aq), in closer analogy to the $H_5O_2^+$ complex in the H^+(aq) system.

At variance with the aforementioned liquid state experiments, microsolvation studies using aqueous hydroxide clusters paint a different picture. In particular, thermochemical[187] as well as spectroscopic[192,195] studies of small clusters, $OH^-\cdot(H_2O)_n$ with $n \leq 7$ and $n \leq 5$, respectively, suggest only three accepted HBs in the first shell so that additional water molecules are relegated to the second solvation shell. At first sight, this appears to agree with the traditional Lewis picture based on the existence of three lone pairs that accept one HB each. However, in contradiction with this experimentally deduced cluster scenario and early computational studies,[218] there is growing theoretical evidence that the *equilibrium* structure of the $n = 4$ cluster, i.e. the global minimum of the Born−Oppenheimer potential energy surface, might indeed have *four* accepted molecules in the *first* shell.[211,219−223] On a cautionary note, it is mentioned that several investigations[224,225] have demonstrated that the minute total energy differences between the two solvation motifs of the order of only 0.01−0.1 kcal/mol are quite sensitive to various computational details. Most interestingly, it has also been shown, by including zero-point and thermal motions on the shallow potential energy surface,[222,223,226] that vibrations and entropy can be sufficiently large to expel a water from the first to the second shell.[219,222,223] All this demonstrates that (quantum−thermal) fluctuations might play a decisive role in determining the preferred solvation pattern even in the limit of small clusters at low temperatures.

This phenomenon is substantiated by explicit AIMD simulations[211] of an isolated $OH^-\cdot(H_2O)_6$ cluster at 110 and 220 K where an averaging effect of the two structural motifs

with four or three accepted HBs in the first shell is observed, i.e. (4 + 2) and (3 + 3) populations of the (first + second) solvation shell; see section 6.2 for a thorough discussion of these revealing simulations. Most interesting, the IR spectra obtained are temperature dependent, as the lower temperature spectrum retains a spectroscopic separation between the 4-fold and 3-fold coordinated OH^- cores. This brings the experimental and theoretical cluster studies into qualitative agreement because experiments can never directly probe the equilibrium structure. In addition, this delicate energy versus entropy interplay might also explain why precise thermochemical data[194] do not support the observation of "magic numbers" n reported much earlier,[187] in particular from $n = 3$ to $n = 4$; in addition, magic numbers of $n = 11$ and *larger* have been observed[188] by studying $OH^-\cdot(H_2O)_{n=0-59}$ clusters which were classified to be "...weak and appear most of, but not all of, the time" (quoted from ref 188). Instead, the new data[194] yield a *continuous* dissociation *energy* as a function of cluster size, while a closing of the first solvation shell at a magic number of $n = 3$ was proposed earlier based on a *discontinuous* drop of the dissociation *enthalpy*.[187] Thus, only the earlier experiment would suggest closure of the first solvation shell with three water molecules around OH^- and thus preference of a $OH^-\cdot(H_2O)_3$ cluster with three accepted HBs.

Apart from these considerations of fluctuation effects, one could ask at the outset if small- or medium-size clusters, $OH^-\cdot(H_2O)_n$, can serve at all as a reliable model for fully hydrated OH^-, i.e. OH^-(aq), which will be addressed in section 6.2. In small clusters, additional water molecules beyond the first shell do not form a HB with the hydroxyl hydrogen but prefer, instead, to form HBs with first-shell solvation water molecules.[211,222,223] In particular, finite-temperature AIMD simulations[211] of IR spectra using the $OH^-\cdot(H_2O)_6$ microsolvation cluster invariably show a free OH stretch attributable to the hydroxide core. This is clearly different from the bulk situation, where the existence of a weak HB donated by the hydroxyl hydrogen is now experimentally well established.[184,196−200,202,205]

Thus, "We conclude by noting that our observation of a transient hydrogen bond donated by OH^-, in conjunction with the hypercoordinated structures discerned in neutron and X-ray diffraction studies of macroscopic OH^- aqueous solutions[10−12] [*these references correspond to refs 197, 198, and 184 in this review*], suggests a hydroxide solvation behavior distinctly different from that inferred from spectroscopic studies on gas-phase $OH^-\cdot(H_2O)_n$ clusters where the weak hydrogen-donor bond is unable to form[27] [*this reference corresponds to ref 195 in this review*]. This difference highlights the importance of long-range water-solvent behavior and also the need for sophisticated experiments in the bulk liquid phase to help formulate and test detailed descriptions of bulk aqueous solution properties." (quoted from ref 205).

Despite all the experimental evidence in favor of dynamical hypercoordination of OH^-(aq) based on diffraction and spectroscopy, there is currently no space- and time-resolved experimental technique available that can resolve all these issues in *molecular detail*. Fortunately, there is old electrochemical data that can shed light on the controversy from a very different angle. It is well established[1] by conductivity measurements that the mobility of H^+(aq), and thus the derived diffusion coefficient, is significantly larger than that of OH^-(aq): 36.23 versus 20.64 $\times 10^{-8}$ $m^2/(s\ V)$ at 298 K, according to the data reported in ref 1. Using the Nernst−Einstein equation, these mobilities translate into the well-known diffusion coefficients for H^+(aq) and OH^-(aq) of 9.31 and 5.30 $\times 10^{-9}$ m^2/s, respectively.[1,227] Both diffusion coefficients are anomalously large, since they exceed, by far, those of typical simple ions in ambient water,[1] for instance 1.33 and 2.03 $\times 10^{-9}$ m^2/s for Na^+(aq) and Cl^-(aq), respectively, which are known to migrate hydrodynamically *via* the vehicular diffusion mechanism. Recalling that the self-diffusion coefficient of water is 2.26 $\times 10^{-9}$ m^2/s, it is evident that diffusion of OH^-(aq) is much faster than water self-diffusion but also slower than H^+(aq) migration. The diffusion coefficients for the fully deuterated systems are 7.03 and 3.27 $\times 10^{-9}$ m^2/s, respectively, for $D^+(aq^D)$ and $OD^-(aq^D)$ at 301 K[87] (or 6.69 and 3.12 $\times 10^{-9}$ m^2/s at 298 K) and 1.86 $\times 10^{-9}$ m^2/s for the self-diffusion of D_2O at 298 K[228,229] (see also ref 230).

These data imply that, apart from rather small H/D isotope effects[228,87,229] on the diffusion coefficients (i.e., about 1.4, 1.7, and 1.2 for H^+(aq), OH^-(aq), and H_2O self-diffusion, respectively), deuteration only reduces the impact of quantum fluctuations in a quantitative way without altering the basic qualitative fact that $D_{H^+} > D_{OH^-} > D_{H_2O}$. In this context, it is noted that this H/D isotope effect is *more pronounced* for OH^-(aq) compared to H^+(aq). Similarly, the kinetic H/D isotope effects for PT rate constants $k_\pm$ between H_2O and H_3O^+ and between H_2O and OH^- as measured by ^{17}O spin relaxation NMR are found to be 1.6 ± 0.2 and 2.8 ± 0.4 for k_+ and k_-, respectively, under ambient conditions.[87] The same observation is reported based on isotopic fractionation of H and D between water and H^+(aq) versus OH^-(aq). The equilibrium constants for the isotope exchange equilibria $H_2O + H_2DO^+ \rightleftharpoons HDO + H_3O^+$ and $H_2O + OD^- \rightleftharpoons HDO + OH^-$ are 0.96 ± 0.02 and 4.21 ± 0.27, respectively, according to refs 231 and 232. Thus, basic aqueous solutions feature *larger* H/D isotope effects when compared to the acidic case.

As advocated in ref 16, comparing OH^-(aq)/H^+(aq) diffusion coefficient *ratios*, in particular for the fully deuterated systems, to the corresponding experimental numbers should provide a robust test for scrutinizing simulated scenarios *qualitatively*, irrespective of quantitative deviations. Although we shall go into greater detail later in section 5.3, the presolvation concept gives us a preliminary glimpse into expected trends of the mirror image and dynamical hypercoordination mechanisms. Assuming the mirror image mechanism, let us consider the case in which OH^-(aq) favors 3-fold coordination of its oxygen by accepting three HBs *and* donates an additional HB *via* its hydroxyl hydrogen, as depicted in Figure 2b and suggested in ref 167. This implies that OH^- would naturally possess a solvation pattern like that of a bulk water molecule and, as such, would always be perfectly presolvated and thus primed for PT, as explained in section 3.2. As a result, ultrafast structural diffusion would be expected if such a solvation shell pattern held for OH^-(aq). Indeed, extremely high PT rates have been observed in ref 167, which have been confirmed and quantified in terms of calculated diffusion coefficients independently in ref 16 using a similar simulation protocol. For dynamical hypercoordination, on the other hand, the presolvation concept predicts no PT in the square-planar majority state $H_9O_5^-$ sketched in Figure 2e or depicted in Figure 4a. This resting state must first be activated by cleaving one of its accepted HBs and strengthening the

donated HB, as explained in section 3.3. The time needed to transform the resting $H_9O_5^-$ complex to the active $H_7O_4^-$ complex limits the rate of PT and thus structural diffusion.[16] Finally, for *static* hypercoordination, OH^- always accepts four HBs at its oxygen site and is, thus, never prepared for PT according to the presolvation concept (see section 3.4). This scenario leaves standard hydrodynamic diffusion of such rigid solvation complexes as the predominant migration mechanism in water, much like simple anions. As a result, the presolvation concept predicts in this case a diffusion coefficient that is smaller than the self-diffusion coefficient of water.[16] These vastly different predictions of diffusion coefficients and their dependence on the solvation pattern of OH^-(aq) will be analyzed carefully later in section 5.3. The main conclusion to be drawn at this stage is the following: In light of widely accepted diffusion coefficients[1] obtained from conductivity measurements, charge migration in the mirror image picture is much too fast, and in the static-hypercoordination picture, it is much too slow.

4. Investigating Structural Diffusion in the "Virtual Lab": Techniques and Validation

4.1. Conceptual Approach

As discussed in the previous section, different solvation patterns and structural diffusion mechanisms for OH^-(aq) have been proposed based on theoretical considerations and computer simulations. Even the most advanced current experiments, on the other hand, cannot yield direct insights into the molecular details of structural diffusion and charge migration mechanisms. A promising route to advance this important field is to confront the aforementioned theoretical scenarios with solid experimental conclusions aiming at eradicating all mechanistic models that are inconsistent with the available data and, hopefully, singling out a scenario that conforms with all available experimental results. Particularly valuable will be a comparison of structural diffusion of OH^-(aq) versus H^+(aq) based on a consistent set of AIMD simulations that reproduces all proposed mechanisms.

Several AIMD studies of OH^- in ambient water have been carried out[16,69,102−104,134,135,167,178−180,182,184] using popular but different density functionals such as PW91,[233] BLYP,[234,235] and HCTH.[236] In addition, these functionals have been used in a host of studies of associated liquids and solutions in general, specifically including H^+(aq). Although these functionals yield the same structural diffusion mechanism for H^+(aq), they were found to favor different coordination states for OH^- in water and, as a result, distinct structural diffusion mechanisms. The particular selection of electronic structure methods, therefore, permits one to examine how the transport mechanism changes when different solvation shell structures dominate over others, allowing the presolvation concept[135] to be used to explain these experiments in a kind of "virtual lab".[237] We have employed this strategy previously[16,134] and review the results here. In addition, we performed analogous simulations of bulk water and H^+(aq) mainly to extract diffusion coefficient *ratios* for all functionals[16] and to compare the proton transport kinetics[134] of H^+(aq) to the various scenarios proposed for OH^-(aq). Such an extensive data set is a prerequisite to carry out a *comprehensive* and *comparative* analysis of the respective structural, dynamical, kinetic, and diffusive properties obtained by the different scenarios.

4.2. Electronic Structure Methods

The functionals employed belong to the family of semilocal density functionals that are obtained within the generalized gradient approximation (GGA). BLYP has been used successfully in many AIMD studies of HB systems such as liquid water,[238−244] including protonated water clusters,[245] methanol,[246,247] and ammonia,[248−250] among a plethora of others. Both BLYP and PW91, which are derived from very different density functional design strategies, were used in recent OH^-(aq) studies (refs 16, 69, 134, 135, 178−180, 182, and 184 and ref 167, respectively). The PBE[251] and revPBE[252] functionals, which were also used previously for this system,[167] are very similar to PW91, since they belong to the same density functional family, so that they are not considered further; note that revPBE[252] has been abbreviated rPBE in ref 167 and that a further PBE modification, commonly denoted as RPBE,[253] was also tested for liquid water.[254] Finally, the third functional, HCTH, represents yet another family of functionals and is known to describe liquid water quite well.[236,240]

Based on AIMD simulations of neat liquid water using such GGAs, it appears that temperature can have a pronounced effect on its dynamical properties in the relevant temperature range[240,255−257] whereas (radial) structure seems to be affected much less. In particular, the computed self-diffusion coefficient of bulk water as a function of temperature is found to compare well with the experimental results,[255,256] but only if the temperature is scaled down by about 20−30%; the system size effect on this quantity is found to be marginal within the range of 32, 64, and 128 H_2O molecules[256] employed. However, it has also been suggested that basis-set truncation errors can have a significant effect on the structure[258] and dynamics[259] of water within the AIMD scheme. In light of these results, the present study will focus on comparative analyses. In particular, diffusion coefficient *ratios* at a given temperature are computed and compared to the experimental ratios. Taking the ratio, any temperature shift that might exist will largely cancel out in small temperature intervals, as can be seen when assuming, for instance, a simple activated process scenario, i.e. $D_X(T) = D_X^0 \exp[-E_X^a/k_BT]$, where E_X^a is the activation energy, in order to approximate the temperature dependence of diffusion coefficients in aqueous solutions[260] for a given species X. Furthermore, it has been shown that defects in the HB network topology help to activate self-diffusion to such an extent that the diffusion coefficient is mainly *determined* by the network topology, with the actual temperature becoming a secondary influence.[256] In the present study, there is always an excess charge defect present which disturbs the surrounding HB network sufficiently, and hence, an overall enhanced diffusivity can be expected.

4.3. Simulation Techniques and Protocol

All data underlying the discussion of the following sections stem from a series of previous AIMD simulations[16,120,122,134,135,178,261] that have been performed consistently during the last ten years using the efficient Car−Parrinello technique[262] (see refs 263−266 for a monograph, Lecture Notes, and reviews) as implemented in the CPMD package.[267] The excess charge due to the defect was compensated by the well-established uniform background method,[263,264] and a 9.865 Å periodic cubic supercell with one OH^- (or H^+) ion and 31 (or 32) water molecules has been typically used in the liquid phase (apart

from reference simulations using 63 water molecules and simulations including counterions as specified further below). The electronic structure was represented within plane wave/pseudopotential Kohn−Sham density functional theory.[263−266] In all simulations, the core electrons were treated via atomic pseudopotentials. For the BLYP and HCTH functionals, Troullier−Martins norm-conserving pseudopotentials[268] with a cutoff of 70 Ry were used. The PW91 simulations employed Vanderbilt's ultrasoft pseudopotentials[269,270] at 30 Ry to be consistent with previous PW91 simulations[167] that also used this pseudopotential type (in addition to employing the closely related projector augmented wave (PAW) scheme[271] for the PBE and revPBE runs, *vide ante*). The fictitious electron mass was $\mu = 800$ au, and the mass of deuterium was used throughout (except in *ab initio* path integral calculations and apart from reference simulations using $\mu = 400$ au to be discussed below) with a 5 au time step. The deuterium mass is used for well-known technical reasons;[263,264] however, the light isotope nomenclature, i.e. "proton", "hydrogen", "OH", "H_2O", etc., will be used throughout this paper.

It is stressed again, in view of recent and ongoing discussions and claims in the literature,[129,167,211,255,272−274] that properly performed Car−Parrinello simulations, in the sense of establishing both adiabaticity and energy conservation throughout the runs, as intrinsically required by the algorithm[275] (see also refs 263−266), yield, within the statistical error bars, the same structural results as (i) Car−Parrinello runs with *very* small fictitious electron masses, (ii) iterative Born−Oppenheimer molecular dynamics, and (iii) *ab initio* Monte Carlo simulations, as convincingly demonstrated for bulk water.[239,241,276] Furthermore, the OH^-(aq) simulation results of ref 167 obtained from Born−Oppenheimer AIMD have been consistently reproduced in refs 16 and 134 using the Car−Parrinello approach to AIMD, as employed earlier[102−104,135,178] and outlined in this review. Importantly, this implies that the qualitatively different OH^-(aq) solvation and charge migration scenarios found in ref 135 versus ref 167 should not be traced back to differences in Born−Oppenheimer and extended Lagrangian (i.e., Car−Parrinello) AIMD propagation techniques, as alluded to in refs 167 and 211. Clearly, in Car−Parrinello propagation, dynamical properties are renormalized due to "dressing" the moving nuclei by the additional inertia of the orbitals that must be dragged along their trajectories[277,271] (see ref 263 for a thorough discussion). This phenomenon is known to lead to a systematic red-shift of vibrational frequencies and thus of bands in IR spectra (see e.g. section 2.4.3 in ref 264 for a discussion and, for example, refs 278 and 279 for early applications of a simple correction scheme proposed earlier in ref 271).

Various technical aspects of performing proper AIMD propagation and sampling have been addressed in detail in a recent monograph[263] (see, in particular, sections 2.4.3−2.4.5, 2.4.9, 2.5, and 2.6 of ref 263) and thus are not reviewed here. These simulation issues, however, must be kept distinct from any systematic errors that are introduced by using nonexact electronic structure methods, which is the case in all AIMD simulations, which necessarily rely on approximate density functional or wave function based levels of electronic structure theory. The effects of the particular choice of the density functional on both static and dynamic properties of liquid water have been analyzed systematically in many papers (see, e.g., refs 238, 240, 242, and 244), and in addition, temperature shifts[240,255−257,276] due to using an approximate functional and artifacts arising from incomplete basis sets[258,259] have been quantified.

Because of the importance of preparing proper initial conditions that are representative of the equilibrium distribution and, therefore, allowing proper sampling of phase space in the rather short times accessible to AIMD simulations, we pause briefly to discuss this issue. In particular, an improperly prepared initial configuration can lead to artificial trapping of charge defects, and the latter can very easily self-localize in a medium with a high dielectric constant, thereby leading to nondiffusive behavior. Indeed, trapping of H^+(aq) defects in AIMD simulations has been reported in the literature.[274] Here, the systems on which most of the reported data[16,134] are based were taken from the final stages of long quantum simulations using the same simulation protocol, i.e. refs 120 and 135 for H^+(aq) and OH^-(aq), respectively. These runs had, themselves, been initialized using the final configurations from the pioneering classical AIMD simulations[102−104] of both H^+(aq) and OH^-(aq). Importantly, the simulations reported in refs 120 and 135 have been run with so-called "massive" Nosé−Hoover chain thermostats[280] that are coupled *separately to all* available nuclear degrees of freedom, in addition to thermostatting the electrons, in order to thermalize the systems most efficiently. Hence, the initial configurations used in refs 16 and 134 constitute perhaps the most thoroughly equilibrated of any configuration ever used in an AIMD calculation of OH^-(aq) and H^+(aq) to date. In addition, these *microcanonical* AIMD simulations[16,134] used for dynamical analyses add up for a total of about half a nanosecond of AIMD simulation time.

4.4. Quantum Effects via Ab Initio Path Integrals

Quantum effects such as zero-point motion and tunneling potentially play an important role in hydrogen-bonded systems, since they involve light atoms such as hydrogen or deuterium.[13] Nuclear quantum effects in chemically complex molecular systems such as charge defects in the three-dimensional HB network of aqueous solutions can be accounted for within the framework of *ab initio* path integrals.[139] This technique[139−142] is a unification of the efficient Car−Parrinello AIMD approach[262] and state-of-the-art path integral molecular dynamics[281] as implemented in the CPMD package.[263,264,267] Only a few aspects need to be addressed here, since applications of *ab initio* path integrals in the realm of HB systems are in widespread use to study liquids,[120,122,135] solids,[282−285] molecules,[261,286] and clusters,[287,288] and have been a specific focus of a recent review,[13] whereas technical issues have been discussed in ample detail in refs 263 and 264. Important in the context of discussing structural diffusion and kinetics is the caveat that it is currently only possible to compute structural properties in the condensed phase rigorously *via ab initio* path integrals. The problem of computing dynamical properties from path integral formulations of quantum time-correlation functions, although unsolved as yet, is an active area of research in the framework of approximate methods.[14,142] For this reason, the analysis of nuclear quantum effects in aqueous systems using *ab initio* path integrals is restricted to distribution functions and free energy profiles as reported in refs 122, 135, and 261.

In these pioneering quantum simulation studies of both H^+(aq)[120,122] and OH^-(aq),[135] where *all degrees of freedom were treated quantum-mechanically*, the electrons were kept

in their instantaneous ground-state (within the framework of the Born−Oppenheimer approximation and the Car−Parrinello propagation scheme) using the BLYP functional, whereas the nuclei moved at the specified physical temperature. The system size was again one OH^- defect solvated by 31 water molecules (or one H^+ and 32 waters), the canonical ensemble was established at 300 K using massive Nosé−Hoover chain thermostats[280] of length three attached separately to each Cartesian degree of freedom, and the Trotter discretization[263,264] was eight beads for the quantum runs. Sampling efficiency was enhanced *via* the staging or normal mode formulations of path integral molecular dynamics.[281] These schemes involve transformations of the primitive Cartesian variables to mode (staging or normal) variables and an adjustment of the fictitious bead masses so that all modes have the same fundamental frequency and move on the same time scale. In addition, the fictitious orbital motion was thermostatted to a fictitious kinetic energy of the electrons of 0.01 au using a separate Nosé−Hoover chain thermostat on the Kohn−Sham orbitals for each Trotter discretization and a chain length of three. In order to assess the quantum effects most directly, analogous Car−Parrinello simulations using classical nuclei with the masses of H and O atoms were also performed in the *canonical* ensemble at 300 K. Apart from this difference in ensembles and the use of the physical isotope mass for both H and O, the technical details of these reference simulations considered in section 6 (published in refs 120, 122, and 135) are similar to the microcanonical simulations described in section 4.3, which constitute the main body of data underlying this review. These consistent data sets allow one to compare in a meaningful way the behavior of OH^-(aq) to H^+(aq) on equal footing as far as structures and free energies as well as quantum and ensemble effects are concerned, which will be the focus of section 6.1. Furthermore, there are also consistent *ab initio* path integral data from gas phase studies of both $OH^-\cdot(H_2O)$ and $H_3O^+\cdot(H_2O)$ solvation complexes at 300 K available[261] which will be compared directly to the corresponding condensed phase data[120,122,135] in section 6.2, thus addressing some aspects of microsolvation versus bulk solvation.

4.5. Computing Infrared Spectra

The IR spectra in section 6.3 are computed within linear response theory from the Fourier transform of the dipole−dipole autocorrelation function. The corresponding linear absorption coefficient $\alpha(\nu)$ at frequency ν is obtained via

$$\alpha(\nu) = \frac{2\pi\nu \tanh(\beta\hbar\pi\nu)}{3\hbar c V n(\nu)\epsilon_0} \int_{-\infty}^{\infty} \mathrm{d}t\, e^{2\pi i\nu t} \langle \hat{\mathbf{M}}(t)\cdot\hat{\mathbf{M}}(0) + \hat{\mathbf{M}}(0)\cdot\hat{\mathbf{M}}(t)\rangle \quad (1)$$

where $\hat{\mathbf{M}}(t)$ is the total dipole moment operator, c is the speed of light, V is the system volume, ε_0 is the vacuum permittivity, $n(\nu)$ is the index of refraction, and $2\pi\nu = \omega$. In practice, no satisfactory methods exist for computing the fully quantum-mechanical dipole−dipole correlation function, and it is necessary to resort to classical approximations. In the present study, the following approximation has been used

$$\alpha(\nu) = \frac{2\pi\nu \tanh(\beta\hbar\pi\nu)}{3\hbar c V n(\nu)\epsilon_0} \int_{-\infty}^{\infty} \mathrm{d}t\, e^{2\pi i\nu t} \langle \mathbf{M}(t)\cdot\mathbf{M}(0)\rangle_{\mathrm{cl}} \quad (2)$$

where the quantum correlation function has been replaced by the classical one but $\tanh(\beta\hbar\pi\nu)$ has been retained as an approximate quantum correction, although we note that more sophisticated quantum correction schemes exist.[289−292] An advantage of AIMD is the direct availability of the electronic component of the dipole moment from the electronic structure. Due to the use of periodic boundary conditions, this component is computed using the Berry phase approach,[293,294] according to which the electronic component of the dipole moment in a cubic supercell at the Γ-point of the Brillouin zone is given by

$$M_{\mathrm{elec}}^{(\gamma)} = -\frac{eL}{\pi}\mathrm{Im}\ \ln \det(R^{(\gamma)}) \quad (3)$$

where γ indexes the three spatial components, and $R^{(\gamma)}$ is a matrix given by

$$R_{ij}^{(\gamma)} = \langle \psi_i | e^{-2\pi i r_\gamma / L} | \psi_j \rangle \quad (4)$$

where $\{|\psi_i\rangle\}$ are the Kohn−Sham orbitals and $r_\gamma = x,\ y,\ z$. The spectra presented in section 6.3 were obtained from carefully equilibrated (using Nosé−Hoover chain thermostatting[280]) microcanonical *NVE* AIMD simulations[178] of aqueous KOH solutions at 1.5 and 13 M concentration (obtained from 1 dissociated KOH with 32 water molecules and 8 dissociated KOHs with 27 waters, respectively, in periodic supercells) using the BLYP functional. The fictitious electron mass was 600 au, and the mass of deuterium was used for hydrogen, as is customary, both of which induce systematic shifts in the IR spectra, as explained in section 4.3. The Fourier inversion according to eq 2 was accomplished using maximum entropy methods. However, more recently, the use of orbital localization techniques[295−297] has yielded simpler and more efficient schemes for obtaining the correlation functions and corresponding spectra.

4.6. Estimating Systematic Errors: System Size, Fictitious Electron Mass, Ensembles, Quantum Effects, Counterions, and Concentration

When using *ab initio* computer simulations, checks on (i) system size, (ii) fictitious electron mass parameter, (iii) statistical-mechanical ensemble differences, (iv) quantum-mechanical fluctuations, (v) counterions, and (vi) defect concentration are necessary in order to estimate the systematic errors introduced by using (i) a certain number of solvent molecules, (ii) a certain finite mass parameter, (iii) microcanonical versus canonical sampling, (iv) the classical approximation to nuclear motion, (v) no counterions, and (vi) a single charge defect, that underly the generation of the primary source of AIMD data. The first point is necessary in order to probe whether the solvation shell structure is *qualitatively* affected by the number of solvent molecules used in the simulations according to the so-called "standard setup", as defined in section 4.3. The second issue, whether the fictitious electron mass parameter[262−264] had been chosen sufficiently small in previous Car−Parrinello simulations, was questioned in the recent literature[255,273] (and reiterated in refs 129, 272, and 274). However, the issue was refuted shortly thereafter.[239,241,276] Nevertheless, this technical aspect of Car−Parrinello simulations was suggested[166,167] as a possible reason for the qualitative disagreement between various AIMD studies of OH^-(aq) that used slightly different protocols (see refs 16, 69, 103, 104, 134, 135, 178−180,

182, and 184 versus ref 167). The third check concerns proper and efficient statistical ensemble sampling. For the canonical ensemble, the "massive" Nosé−Hoover chain thermostatting method has been shown to improve sampling efficiency.[281,298] Only when explicit dynamical properties (kinetics, IR spectra, ...) are sought should the microcanonical ensemble be employed. Fourth, quantum effects due to the light hydrogens have been shown to play some role in structural diffusion in both acidic[120,122] and basic[135] solutions. Fifth, all experiments necessarily include counterions whereas the standard simulations are carried out using a uniform, compensating charge background, as is usually done in such cases.[263,264] Finally, current diffraction and spectroscopic experiments are typically performed at fairly high acid or base concentrations (up to solute/solvent ratios of 1:3), whereas about 1:30 is used in the standard simulations.

All of these cross-checks will be carried out for the most important combination of system and setup: OH^-(aq) with the BLYP functional using classical nuclei (with the deuterium mass for H) in the microcanonical ensemble. In order to check the influence of system size, the number N of molecules has been doubled from 31 water molecules to 63 H_2O, both hosting one OH^- defect and subject to periodic boundary conditions using a cubic supercell. Note that this also amounts to decreasing the concentration of the solution, since there is still only one negative excess charge in the large system. Second, the fictitious electron mass μ needed in Car−Parrinello propagation[262,275] has been decreased to half its value, i.e. from 800 to 400 au, still using the deuterium mass for hydrogen but a time step of only 3 au to ensure proper integration of the Car−Parrinello equations of motion (see refs 263−266).

A gross comparison is already obtained at the level of the total radial distribution functions, $g_{OO}(r)$ and $g_{OH}(r)$. They are depicted in Figure 5a for the standard setup used to investigate the dynamical hypercoordination scenario, as well as for the benchmark simulations using a large system and a small electron mass. The peak positions are essentially identical, and the intensities, i.e. the heights of the peaks, are very similar considering the expected statistical errors of such simulations. The same conclusion is drawn from the refined radial analysis around the OH^-(aq) charge defect O* in the two limits, $|\delta| \leq 0.1$ Å and $|\delta| \geq 0.5$ Å in parts b and c, that analyze the OH^-(aq) environment in both the active and resting states, respectively, as sketched in Figure 2g and e and depicted in the bottom and top panels of Figure 4, respectively. Most importantly, the preferred solvation number of the two limiting complexes, i.e. the plateau value of the running coordination number shown in the insets of panels b and c, is virtually identical for the three parameters choices. This is also supported by both the radial distribution functions of the HB donor site, $g_{H'O_w}(r)$ shown in Figure 6a for the active state, and the HB probability distribution function $P(n^*)$ involving O* as an acceptor presented in Figure 7.

Beyond their impact on structure, the effect of the standard choice of N and μ on dynamic properties must be investigated as well. Here, their influence on diffusion coefficients is presented, while relaxation times and rates will be examined in more detail in sections 5.5 and 5.6. It is seen from the data in Table 1 that changing either the system size or the fictitious electron mass parameter by a factor of 2 changes the ratio of the diffusion coefficient of OH^-(aq) versus the approximate self-diffusion coefficient of water from about

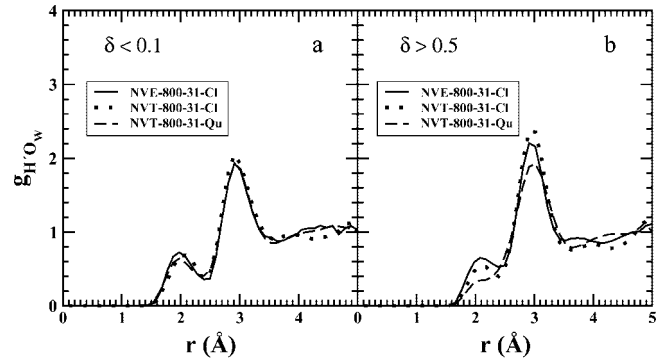

Figure 8. Radial distribution functions, $g(r)$, of OH^-(aq) obtained from the dynamical hypercoordination mechanism of $H'O_w$ for $|\delta| \leq 0.1$ Å (a, left) and $|\delta| \geq 0.5$ Å (b, right) using the (standard) classical microcanonical ensemble (solid), the classical canonical ensemble (dotted), and the quantum canonical ensemble (dashed); see caption of Figure 2a and section 5.1 for definitions and labeling conventions. Based on data from refs 16, 134, and 135.

$D_{OH^-}/D_{H_2O}^{same} \approx 4$ to about 3 and 5, respectively. Thus, the same qualitative picture is obtained with the refined parameters as with the standard setup. Note that the former has a significantly more substantial associated computational overhead. Similarly, using a new kinetics analysis framework[134] (see section 5.5), relaxation times and PT rates have been compared for OH^-(aq) within the dynamical hypercoordination mechanism. The comparison ultimately leads to the same conclusion, that is, that the standard protocol yields qualitatively reliable predictions of the dynamics.

Concerning the comparison of ensemble choice and classical versus quantum effects, it is noted that ref 135 reports *canonical* classical and quantum results for OH^-(aq), while refs 16 and 134 report microcanonical simulation data. The pertinent canonical simulation protocol is summarized in section 4.4; it is only reiterated here that the system size was again one OH^- in 31 H_2O and that the physical H and O masses have been used for H and O atoms in both the quantum and classical canonical simulations. The effect of switching from the classical microcanonical *NVE* to the classical canonical *NVT* ensemble, where sampling is much more efficient, is found to be negligibly small, as demonstrated in Figure 8. The figure shows a comparison of radial distribution functions $g_{H'O_w}(r)$ of the HB donor site for the dynamical hypercoordination mechanism. The same conclusion is obtained from the respective probability distribution function $P(n^*)$ involving O* of OH^-(aq) as HB acceptor, as demonstrated by Figure 7b. It will be shown that quantum fluctuations, (iv), do not dramatically affect the local *structures* relevant to charge migration in aqueous systems but do influence PT *free energies*.[13,120,122,135] This important aspect, however, will not be discussed in this largely technical section. Rather, it will be taken up in section 6.1 in conjunction with a detailed comparison of the impact nuclear quantum effects have on PT in OH^-(aq) and in H^+(aq).

Issues (v) and (vi) above, i.e. neglect of countercation effects and use of a single OH^- in a periodic box of 31 water molecules, will be scrutinized in section 6.3 with respect to data obtained from a 1.5 M aqueous KOH solution;[178] note that one OH^- in 31 H_2O molecules corresponds to a concentration of about 1.5 M. In a nutshell, detailed analyses in section 6.3 will show that including the counterion K^+, as is present in any experiment, affects neither the solvation shell structure nor the PT free energy of the dynamical

hypercoordination mechanism at any significant level in comparison to the standard approach.

Clearly, the crux of all these cross-checks in terms of structure, dynamics, and free energies is that the "standard" simulation method, setup, and protocol are sufficient to provide reliable data for involved analyses which can be directly confronted with experimental conclusions.

5. From Solvation Shell Structure to Diffusion and Kinetics: Scrutinizing the Different Mechanisms

5.1. Preliminaries

Several independent analysis approaches will be presented in order to investigate in molecular detail the implications of three different charge migration mechanisms discussed in the literature. As noted in section 3, these mechanisms could be derived within the unifying presolvation concept, which was summarized in section 2 using H^+(aq) as its showcase example. Fortunately, as explained in section 4, the three OH^-(aq) mechanisms can be "generated" with AIMD by using different density functionals; in particular, the well-known PW91 functional yields a traditional mirror image mechanism, BLYP predicts dynamical hypercoordination, whereas the HCTH functional leads to static hypercoordination. This allows us to dissect the various mechanistic proposals from section 3 in the sense of a "virtual lab approach"[237] to the structural diffusion question, with the ultimate aim of judging the different scenarios based on numerous recent experiments (as reviewed in section 3.5).

Here, we give a brief summary of the analysis to be performed. First, those properties of each mechanism that are intimately related to the *structure* of the solvation shell, including the coordination patterns of OH^-(aq) in equilibrium and close to PT events, will be discussed in section 5.2. Second, the *diffusion* properties are investigated in section 5.3 with the aim of determining how the diffusion coefficient of OH^- in water compares to that of H_3O^+ and to the self-diffusion of H_2O. Here, we stress again that only perdeuterated systems are considered for the reasons given in section 4 (see also the experimental data presented in section 3.5). Third, the three qualitatively different OH^-(aq) diffusion *mechanisms* sketched out in Figure 2 are extracted in molecular detail from these AIMD simulations in section 5.4. Fourth, the *kinetics* of PT and structural diffusion of OH^- are quantified in terms of a set of population time-correlation functions in section 5.5 and connected to the derived mechanistic pictures with the aid of various lifetimes, rates, and relaxation times. Fifth, the *rotational relaxation* time of OH^-(aq) relative to that of the water molecules themselves is computed for the three different scenarios and compared to recent experimental data in section 5.6. Sixth, the importance and possible implications of *quantum effects* and *microsolvation* on both OH^-(aq) and H^+(aq) are addressed in sections 6.1 and 6.2, respectively. Finally, the possible effects of *counterions* and increased *concentration* on the dynamical hypercoordination mechanism for OH^-(aq) are discussed in section 6.3.

As a result of these comparisons, the dynamical hypercoordination mechanism can be singled out as predicting structural and dynamical properties of aqueous basic solutions that are consistent with experimental data.

In order to locate, follow, and analyze the OH^- charge defect in the HB network, which is designated $(O^*H')^-$ for this purpose, the respective oxygen O* and the covalently bound hydrogen H′ must be identified for each configuration in the trajectories that are generated by the AIMD simulations (see Figure 2a for the labeling scheme used). Note that H′ can, in principle, donate a HB to a nearby water molecule, i.e. schematically $[O^*H'\cdots OH_2]^-$. For each HB involving O*, a displacement coordinate, $\delta = R_{O_aH} - R_{O_bH}$, is defined, where R_{O_aH} and R_{O_bH} are the distances between the shared proton and the two oxygens. A small value of $|\delta|$ indicates a propensity for PT, and a PT coordinate δ is defined in each configuration by selecting the HB with the smallest $|\delta|$ value. This particular HB, i.e. schematically $O^*\cdots H^*\bar{O}$, is considered to be the "most active" HB or the most likely HB to experience PT,[120,135] and the water molecule with $\bar{O}$ as its oxygen has a propensity for donating the proton H* upon transfer; note that, in the case of charge defects in acidic solution and thus in H^+(aq) diffusion, H* is the excess proton that is covalently bound to O*, i.e. schematically $O^*H^*\cdots\bar{O}$, so that $\bar{O}$ is the proton-receiving oxygen. Thus, the PT coordinate is given by $\delta = R_{O^*H^*} - R_{\bar{O}H^*}$ and $R_{OO} = R_{O^*\bar{O}}$ is the oxygen−oxygen distance of the most active HB. Separate consideration of instantaneous complexes with small and large values of $|\delta|$ allows analysis of the local structural changes during PT. Here we have chosen $|\delta| \geq 0.5$ Å and $|\delta| \leq 0.1$ Å to filter out, respectively, those configurations corresponding to the equilibrium state and those close to PT events. Finally, unspecified (solvent) water molecules are designated by O_w and H_w.

5.2. Solvation Shell Structures

A general picture of the OH^- solvation shell in bulk solution is provided by the O^*O_w and O^*H_w radial distribution functions obtained for all three mechanisms, which, as shown in the insets of Figure 9, turn out to be quite similar. In particular, all mechanisms yield the expected contraction of the first solvation shell around the defect with respect to the average O_w-O_w distance in pure bulk water,[236,238−240] in qualitative agreement with neutron diffraction.[196] However, this contraction effect is clearly more pronounced for mirror image solvation than for hypercoordination. The running coordination numbers of O^*O_w (and O^*H_w) yield 4.2, 4.8, and 4.7 (and 3.5, 4.0, and 4.0) at the first minimum for mirror image solvation, dynamical hypercoordination, and static hypercoordination, respectively. This analysis is refined in the main panels of Figure 9 by investigating the HBs involving H′ separately for configurations close to PT events ($|\delta| \leq 0.1$ Å) and in the opposite limit of strongly bound OH^- units ($|\delta| \geq 0.5$ Å). It is crucial to observe that the HB donated by the charge defect, that is $H'\cdots O_w$, is always present in the case of mirror image solvation, irrespective of the dynamical situation. This is revealed by a pronounced *peak* that is present around 1.8−2.0 Å in *both* δ-limits according to Figure 9. In contrast, in the dynamical hypercoordination picture, the H′ HB is most pronounced for small $|\delta|$, whereas the peak degenerates into a broad plateau for large $|\delta|$.

For all three mechanisms, the *most probable* number of HBs donated by H′ (not shown) is unity, with only slightly different *average* H′ coordination numbers $\langle n' \rangle$ of about 0.67, 0.72, and 0.61 for mirror image, dynamical, and static hypercoordination, respectively; note the accidental interchange of the PW91 and BLYP numbers reported in ref 16.

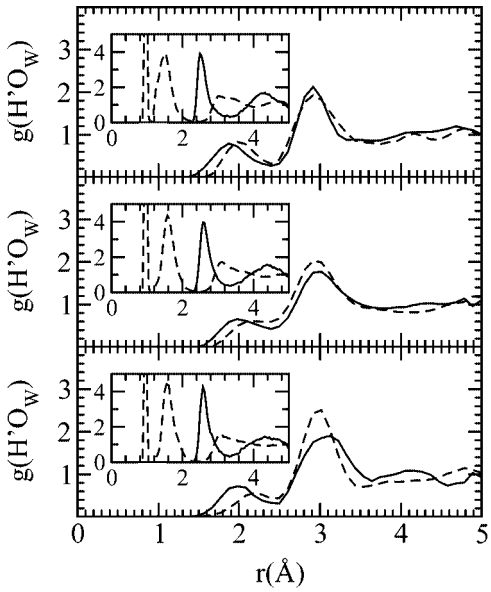

Figure 9. Radial distribution functions, $g(r)$, of OH^-(aq) of $H'O_w$ obtained from the traditional mirror image mechanism (a, top), the dynamical hypercoordination mechanism (b, center), and the static hypercoordination mechanism (c, bottom) for $|\delta| \leq 0.1$ Å (solid) and $|\delta| \geq 0.5$ Å (dashed); see caption of Figure 2a and section 5.1 for definitions and labeling conventions. The insets show the corresponding full O^*O_w and O^*H_w (including the H′ hydrogen) radial distribution functions as solid and dashed lines, respectively. Reprinted with permission from ref 16. Copyright 2006 American Chemical Society.

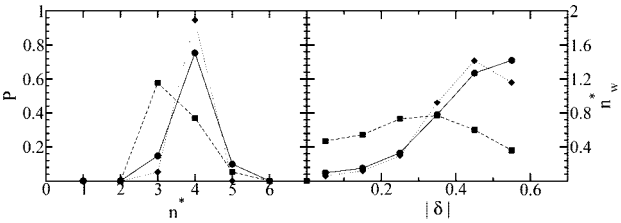

Figure 10. (a, left) Hydrogen bond probability distributions of OH^-(aq) involving O* as acceptor, $P(n^*)$, obtained from the traditional mirror image mechanism (squares, dashed), the dynamical hypercoordination mechanism (circles, solid), and the static hypercoordination mechanism (diamonds, dotted). (b, right) Weighted O* coordination number (see text) as a function of $|\delta|$, $n_w^*(|\delta|)$, obtained from the traditional mirror image mechanism (squares, dashed), the dynamical hypercoordination mechanism (circles, solid), and the static hypercoordination mechanism (diamonds, dotted); here $|\delta| \leq 0.1$ Å, $0.1i < |\delta| < 0.1(i + 1)$, $i = 1-4$, and $|\delta| \geq 0.5$ Å. The linear connections between the data points only serve as an optical guideline. Based on data from refs 16 and 134.

This implies that the *time-averaged* H′ coordination is quite similar in all mechanisms, and thus, the H′ coordination must *vary in time* in view of the different small and large δ-limits evidenced by Figure 9. Importantly, the number of accepted HBs, i.e. the O* coordination number, differs qualitatively according to Figure 10a. In the case of the mirror image scenario, the most probable state is that with three accepted waters, whereas both dynamical and static hypercoordination favor 4-fold coordination; the average coordination numbers $\langle n^* \rangle$ are 3.5, 4.0, and 4.0 for mirror image, dynamical, and static hypercoordination, respectively. This qualitative difference of the O* solvation is analyzed in more detail in Figure 10b using an O* coordination number $n_w^*(|\delta|)$ that is plotted as a function of the PT coordinate $|\delta|$ and weighted by the fraction of configurations that contribute to each $|\delta|$-

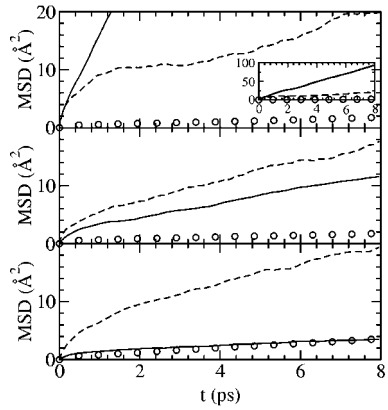

Figure 11. Mean-square displacement of O* for OH^- (solid) or for H_3O^+ (dashed) and of O_w for H_2O (circles) from H^+(aq), OH^-(aq), and pure water simulations as a function of time, MSD(t), obtained from the traditional mirror image mechanism (a, top), the dynamical hypercoordination mechanism (b, center), and the static hypercoordination mechanism (c, bottom); the inset in part a covers the full y-range needed in order to display the maximum value of $MSD(t_{max}) \approx 100$ Å^2 reached for PW91 at the end of an 8 ps time window. Water self-diffusion is obtained from independent bulk simulations; note that the deuterium mass is used for H throughout. Reprinted with permission from ref 16. Copyright 2006 American Chemical Society.

window. For dynamical hypercoordination, $n_w^*(|\delta|)$ is at its largest far from PT events ($|\delta| \gg 0$) and decreases significantly close to PT, i.e. as $|\delta| \rightarrow 0$, signifying that there is a clear change in the coordination number when the proton is transferred and that the low-coordination intermediate states visited during PT are only visited transiently. In stark contrast, $n_w^*(|\delta|)$ does not vary much along $|\delta|$ within the mirror image scenario, implying that the number of accepted HBs by O* is essentially independent of PT; note that $n_w^*(|\delta| \approx 0)$ even exceeds $n_w^*(|\delta| \gg 0)$ according to this scenario.

The data in Figures 9 and 10, capture three distinctly different solvation patterns that have been proposed in the literature and thus lie at the heart of the controversy. This rich database allows one to perform a "virtual experiment"[237] to test each mechanistic scenario: classic Lewis-type 3-fold coordination of O*, dynamical hypercoordination, and static hypercoordination. As will be shown in the following, these quite subtle changes in the solvation shell *structure* will result in vastly different charge migration *dynamics* and *kinetics*.

Before proceeding, let us stress that the $H'\cdots O_w$ HB exists in all three charge migration scenarios, although with slightly different characteristics. This implies that there is no theoretical basis to mechanism pictures that do not take this HB into account. Moreover, the existence of the $H'\cdots O_w$ HB calls into question the reliability of *small* microsolvated clusters, which involve only accepted HBs, as models for the bulk solvation and transport of OH^-(aq) in basic solution (see sections 3.5 and 6.2).

5.3. Structural Diffusion versus Self-Diffusion

The mean-square displacements in Figure 11 demonstrate that in all three cases an astonishingly similar behavior for both water self-diffusion and proton structural diffusion is observed. Note that, in order to compute the mean-square displacement, not only is the minimum image convention *not* applied to the calculation of a distance $|\mathbf{r}_i(t) - \mathbf{r}_i(0)|$, but also any proton transfer events that occur across the periodic boundary must be "unfolded" by explicitly translating the position of O* by a box length in the appropriate direction.

Table 2. Diffusion Coefficients in Units of 10^{-9} m^2/s (i.e. 10^{-1} $Å^2/ps$) Obtained from the Slopes of the Mean-Square Displacements Shown in Figure 11 Obtained from the Traditional Mirror Image Mechanism (MIM), the Dynamical Hypercoordination Mechanism (DHM), and the Static Hypercoordination Mechanism (SHM)[a]

quantity	MIM	DHM	SHM	experiment
D_{OH^-}	18.5	1.92	0.44	3.12
D_{H^+}	3.24	2.83	3.25	6.69
D_{H_2O}	0.30	0.25	0.64	1.86
D_{OH^-}/D_{H^+}	5.88	0.68	0.14	0.47

[a] Water self-diffusion is obtained from corresponding separate bulk simulations; note that the deuterium mass is used for H throughout and that the reported experimental data[87,228,229] are those of the fully deuterated systems as well. Based on data from ref 16.

In addition, note that, in stark contrast to recently published results on $H^+(aq)$ diffusion,[274] the simulation protocol used here clearly leads to diffusive motion of the charge defect *in all cases studied*, as the figure demonstrates (see section 4 and ref 16 for original data). A similar conclusion has been drawn in ref 69 based on investigating the mean-square displacement of the hydroxide as a function of time (see Figure S1 in the Supporting Information of ref 69).

For $OH^-(aq)$, on the other hand, dramatic *qualitative differences* are readily observed. The dynamical hypercoordination scenario predicts a mean-square displacement with a smaller slope in the linear regime than that of $H^+(aq)$ but larger than that of pure water. Within static hypercoordination, the structural diffusion of $H^+(aq)$ exceeds that of $OH^-(aq)$, but the latter is of the same magnitude (or even slightly slower) than water self-diffusion. Finally, $OH^-(aq)$ structural diffusion according to the mirror image mechanism is found to be exceedingly fast, in agreement with previous simulations and conclusions[167] obtained within this scenario. As Figure 11 (top panel) indicates, $OH^-(aq)$ diffusion overshoots that of $H^+(aq)$ by a considerable amount. This phenomenon becomes particularly evident when examined on an appropriate scale (see inset in the top panel of Figure 11).

Keeping in mind known difficulties in obtaining accurate *absolute values* for diffusion coefficients from such relatively short simulations and small system sizes, one should compare their *ratios* to experimental data, as argued in section 4; note that the deuterium mass is used for H throughout. Experimentally,[1,87,228−230] it is well established that $H^+(aq)$ structural diffusion is the fastest diffusion process in ambient water, followed by $OH^-(aq)$ structural diffusion and finally by water self-diffusion (see section 3.5). In particular, migration of $H^+(aq)$ is more than two times faster than that of $OH^-(aq)$ for the perdeuterated systems (see Table 2 for data). Clearly, out of the three scenarios investigated, only dynamical hypercoordination, which features a 4-fold coordination pattern for $OH^-(aq)$ with transient 3-fold coordination during PT, is able to reproduce these very basic experimental facts. By contrast, the mirror image mechanism, in which the hydroxide is consistently held in a water-like coordination topology (three accepted HBs and one donated), actually *reverses* the relative magnitude of the $OH^-(aq)$ and $H^+(aq)$ diffusion coefficients, yielding a ratio $D_{OH^-}/D_{H^+} \approx 6$ instead of ≈ 0.5 as observed experimentally! This is clearly a highly unphysical situation. Finally, static hypercoordination, which overemphasizes the 4-fold coordination of O*, yields a $OH^-(aq)$ diffusion that is comparable or even slower than water self-diffusion, which is also clearly unphysical.

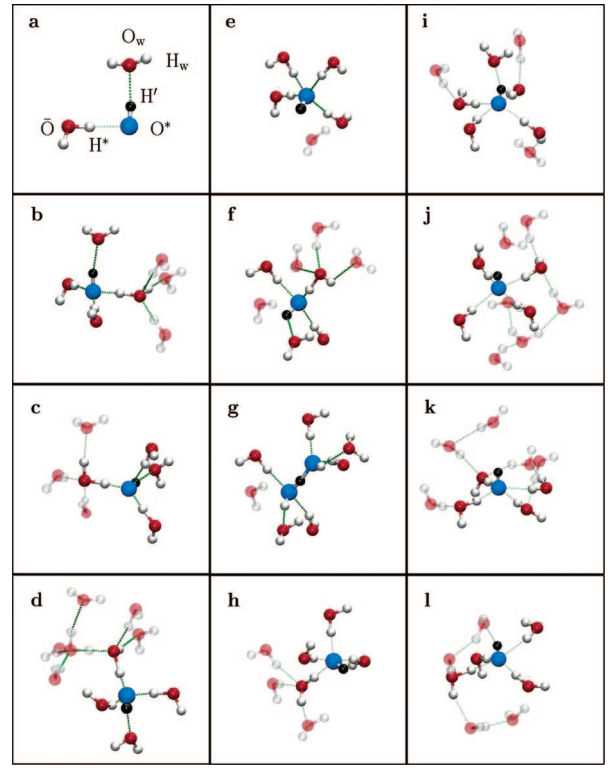

Figure 12. Different charge migration mechanisms of OH^- in bulk water, $OH^-(aq)$, obtained from representative configurations sampled from *ab initio* molecular dynamics trajectories; see Figure 2 for the corresponding schemes. (a) Labeling convention of the defect site. Traditional mirror image mechanism, b−d; dynamical hypercoordination mechanism, e−h; and static hypercoordination mechanism, i−l. Only the most important species in the periodic simulation supercell are shown, the defect is highlighted in blue and black, water molecules beyond the first hydration shell are transparent when shown, and the coordinate system is fixed in space for all frames of a given sequence. Reprinted with permission from ref 134. Copyright 2006 American Physical Society.

5.4. Molecular Analyses of Charge Migration Mechanisms

From the above analyses, three *different* $OH^-(aq)$ charge transport mechanisms, which are consistent with the corresponding averaged structural data, can be extracted from the trajectories, as will be shown below. They are displayed in Figure 12 in terms of *de facto* sampled snapshot configurations arranged such as to parallel the simplified schematic renderings presented in Figure 2.

As analyzed in section 5.2 (see in particular Figure 9a therein), the simulations show that solvation according to the mirror image mechanism strongly favors three accepted HBs by O* in addition to a fourth one that is frequently donated by the OH^- hydrogen H′. This exact situation is shown by the representative configuration selected for Figure 12b. In this tetrahedral environment, a neighboring water molecule (right part of the frame) can readily transfer a proton to OH^- upon a suitable fluctuation, which results in the arrangement shown in Figure 12c. But even at the new vertex site, OH^- is perfectly tetrahedrally solvated and, therefore, in a perfect state to receive a proton from one of *its* first shell water molecules. This leads readily to the next PT event, as depicted in panel d of Figure 12. Thus, not only does the coordination pattern predicted by mirror image solvation lead to a scenario where OH^- is nearly always perfectly embedded in the HB network of bulk water like

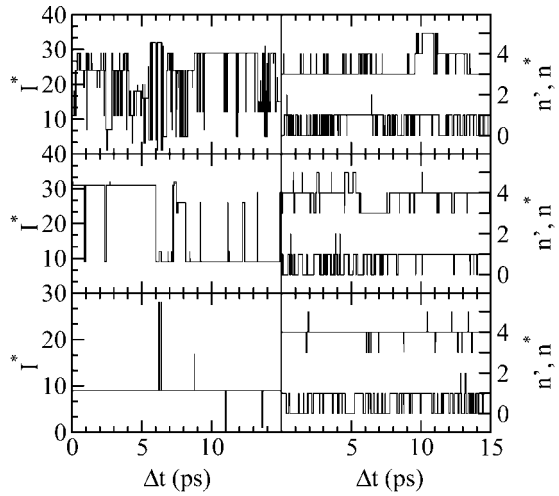

Figure 13. Index of the OH^- oxygen O*, I*, and the instantaneous number of its accepted and donated HBs, n^* (upper curve), and n' (lower curve), respectively, of OH^-(aq) shown for segments of the trajectories obtained from the traditional mirror image mechanism (a, top), the dynamical hypercoordination mechanism (b, center), and the static hypercoordination mechanism (c, bottom). Reprinted with permission from ref 16. Copyright 2006 American Chemical Society.

any *intact* water molecule, but the presolvation concept is able to predict the mechanism that results from this fact. When OH^-(aq) accepts three HBs and donates one as its most likely coordination pattern, it is not a *topological defect* at all, since it can be integrated perfectly into an ideal three-dimensional network like any intact water molecule. This means, in particular, that no coordination number change is required in order to prepare it to receive a proton in a PT reaction. Hence, the protons and thus the defect can move through the network "quasi-ballistically" with little or no hindrance. This is borne out in Figure 13a, in which one can follow the dynamics of the defect in the space of the water molecule numbers involved. More important is the observation, accessible with the aid of Figure 13a, that PT events and HB fluctuations in the first shell of OH^-(aq) are largely uncorrelated, which is consistent with earlier observations reported in ref 167. This analysis explains naturally why PT occurs on an ultrafast time scale in the mirror image scenario advocated in ref 167, in which OH^- predominantly accepts three HBs and donates one. It also answers qualitatively the question: "Rationalizations why the simulation rates [*which refers to computed PW91 and revPBE diffusion coefficients reported in the previous paragraph therein*] are higher than observed experimental rates would be highly speculative" (quoted from ref 167) raised in ref 167, i.e. why the diffusion coefficient of OH^- is unphysically large compared to both H_2O self-diffusion and H^+(aq) structural diffusion (see Figure 11a and Table 2). This statement will be quantified later in section 5.5 based on a comprehensive analysis of PT kinetics that governs charge migration according to the mirror image scenario.

In the static hypercoordination scenario, structural analysis of the first solvation shell in section 5.2 clearly shows that OH^-(aq) almost always accepts four HBs in addition to donating one (see in particular Figures 9c and 10). This leads to a saturated solvation shell such as the one chosen in panel i of Figure 12. Thus, very different from the mirror image scenario, in static hypercoordination, OH^- is rarely solvated in such a way as to receive an additional proton *via* PT from a water molecule that donates a HB to O*. The resulting charge defect dynamics depicted in Figure 13c make clear that *structural* diffusion is extremely *slow* in the sense that the identity of O* rarely changes on a time scale of about 10 ps. Moreover, switches of the O* identity and thus PT are highly correlated with switches from four to three accepted bonds around O*. In conjunction with the slow diffusive dynamics in Figure 11c, this suggests that here OH^- moves mainly like a simple ion, i.e. by carrying a rather tightly bound and bulky solvation shell with it. This means that diffusion occurs essentially via HB fluctuations that exchange water molecules in the *second* solvation shell around OH^-. This mechanism is nicely represented by the sampled snapshot sequence (i) → (j) → (k) → (l) shown collectively in Figure 12. These findings, which will be quantified in section 5.5 in terms of kinetics parameters, explain straightforwardly why the diffusion coefficient of OH^- in water obtained within this scenario is *slower* than that of H_2O in water (see also section 3). Thus, the static hypercoordination mechanism produces mainly slow vehicular diffusion of a long-lived solvation aggregate, $[OH^- \cdot (H_2O)_n]$(aq), interrupted by fast structural diffusion steps, with the latter, however, being rare events.

Turning finally to the scenario emerging from *dynamic* hypercoordination of OH^-(aq), this peculiar coordination pattern of OH^- predicts a mechanism based on both hypercoordination and dynamical solvation shell changes. In particular, a resting state (characterized by four accepted and no donated HBs) and an active state (with three accepted and one donated HB) are involved that have been characterized in section 5.2 in terms of their structures (it is stressed that these solvation patterns are subject to fluctuations and local disorder effects and, thus, should only be considered as idealized structures or limiting forms much like the Eigen and Zundel complexes in the H^+(aq) case). It is important to emphasize that the most probable state is clearly the resting state with four bonds in a square-planar arrangement; such a situation was selected for Figure 12e. Note that a water molecule might already be located somewhat close to H′ without however being hydrogen-bonded, which is included as a transparent molecule in Figure 12e. The trigger for a PT event is a fluctuation in the second solvation shell of O* that reduces the number of accepted HBs from four to three in the *first shell* of OH^- by HB cleavage, and simultaneously, another HB is donated by H′, as can be seen in the series of frames e and f in Figure 12. Only in this active state of roughly tetrahedral configuration, characterized by three accepted and one donated HB, is the proton-receiving species, i.e. OH^-, presolvated like a regular water molecule. In this state, a proton from a neighboring water molecule (in the upper right corner of panel g in Figure 12) can transfer to the OH^- of panel Figure 12f. As a result of this PT event, the charge defect is shifted along a HB and, after the newly formed defect acquires a fourth HB, is located, in a 4-fold coordinated state, at a neighboring vertex site, as shown in Figure 12h. There, it relaxes to a resting state configuration (not shown) such as the one of panel e of Figure 12. This nontraditional mechanism[135] leads to the active but not overly fast charge defect dynamics depicted in Figure 13b; a similar observation was reported more recently in ref 69 (see Figure S1 in the Supporting Information of ref 69). The data clearly reveal—in accord with the presolvation concept—that first shell coordination number changes of O* from four to three accepted bonds, in addition to the donation of another HB by H′, are strongly correlated with PT events. This implies

a rate-limitation by those HB fluctuations that ultimately breaks an accepted bond in the *first solvation sphere* of O* in conjunction with donating a HB by H′. Before revealing the details in section 6.3 on concentration dependence, we briefly note here that the same nontraditional mechanism is found in simulations with counterions using KOH[178] and NaOH solutions;[179,180] these simulations also reproduce the measured IR and Raman spectra.[213]

We close this section by comparing the simulation results to theoretical predictions of the classic mirror image picture. Let us assume for a moment that the proton hole mechanism could proceed without involvement of the H′···O_w donated HB, in the sense of not including this ingredient explicitly in the discussion of the mechanism.[164] Thus, in this mechanism, the OH^-(aq) accepts three HBs and donates none and, therefore, is never coordinated like a bulk water molecule, even during PT (see Figure 3 in ref 164 for the rate-limiting step). Here, the following must be stressed: (i) the PT step, which would require HB cleavage between first and second solvation shell members as in H^+(aq) according to the presolvation concept, would produce a nascent water molecule in a less favorable 3-fold solvation pattern; (ii) *all* simulations consistently predict that the H′···O_w HB must be donated when the proton is transferred. Therefore, it appears that there is little substantive evidence to support mechanistic proposals that do not consider donation of a HB by OH^-(aq). As an experimental corollary of this statement, *small* $OH^-\cdot(H_2O)_n$ microsolvated clusters in the gas phase, known *not* to form this particular H′···O_w HB (see e.g. refs 192, 195, 211, 219, 221−223, and 226), are unlikely to be a useful system class to help understand charge migration in *bulk* aqueous bases, in agreement with the previous discussion of the recent experimental findings in section 3.5 (see also section 6.2).

5.5. Population Correlation Functions: Connecting Solvation Shell Dynamics to Proton Transfer Kinetics

Having rationalized qualitatively the three different mechanisms in section 5.4, the comparison can be quantitatively confirmed by establishing a unifying kinetic model. The preceding analysis clearly suggests that, given the assumptions of the three charge migration scenarios, the mechanisms to which they lead can be predicted using the presolvation concept. In short, the OH^- ion must be presolvated like a bulk water molecule before it can receive a proton from a water molecule in the first solvation shell. Where the three scenarios differ dramatically is the amount of activation needed to achieve the "prepared" state. That is, the rate-determining step, equilibrium concentrations, and interconversion dynamics of the most important solvation complexes differ substantially between the three pictures. Despite these differences, it is certainly reasonable to assume that PT, and hence the structural diffusion process, in each case can be traced back to some physical time scale(s) intrinsic to the particular model, i.e. to the particular structural diffusion mechanism.

In order to scrutinize the different mechanisms in terms of the underlying detailed kinetics, we employ the powerful machinery of population time-correlation functions,[299,300] which has been successfully applied to HB dynamics.[152,299−307] Here, we have developed a set of population indicator functions whose time correlations allow PT and charge migration processes in general HB systems to be analyzed and connected to the underlying solvation or HB patterns.

We begin our description of the formalism by introducing a set of populations, projectors, and correlation functions that account for the different defect types and the different solvation shell patterns in question. These functions are specified in terms of appropriate indicator or population functions, denoted $h(t)$ and $H(t)$, defined as follows: $h(t) = 1$ if a given oxygen is O* at time t and $h(t) = 0$ otherwise and $H(t) = 1$ if O* retains its identity *continuously* up to time t (see Figure 12a for the labeling convention used here). Using these indicator functions, we define an intermittent time correlation function as

$$C_i^{OO}(t) = \frac{\langle h(0)\, h(t)\rangle}{\langle h\rangle} \tag{5}$$

which yields the probability of finding the same O* at times $t = 0$ and t, irrespective of any possible identity change in the interim period. We also introduce a continuous correlation function

$$C_c^{OO}(t) = \frac{\langle h(0)\, H(t)\rangle}{\langle h\rangle} \tag{6}$$

which yields the probability that O* retains its identity over a time interval of length t.

In the calculation of such correlation functions, so-called "proton rattling" events, in which a proton is transferred from O* into the first solvation shell but then returns to the original O*, can be either included or excluded. Including them allows ultrafast dynamics accessible to femtosecond experiments to be extracted, as carried out successfully in ref 97 for the H^+(aq) case. However, since rattling events do not contribute to an overall net displacement of the structural defect, excluding them provides a clearer picture of the net transport mechanism. Accordingly, the average O* lifetime can be obtained from

$$\tau_{exch} = \int_0^\infty C_c^{OO}(t)\, dt \tag{7}$$

which is the average time needed for PT to O* from a first solvation shell water molecule, and correspondingly, $1/\tau_{exch}$ is the average PT rate. The decay of $C_i^{OO}(t)$, on the other hand, depends not only on $1/\tau_{exch}$ but also on the rate of the reverse process.

In order to disentangle the coupled forward/backward kinetics, a projector g is defined as follows: $g(t) = 1$, if an oxygen atom, which was O* at $t = 0$, either remains O* or is found in the first hydration shell of O* at time t (and $g(t) = 0$ otherwise). Thus, the projected nearest-neighbor correlation function

$$C_{nn}^{OO}(t) = \frac{\langle h(0)[1 - h(t)]g(t)\rangle}{\langle h\rangle} \tag{8}$$

measures the probability of finding an oxygen atom in the hydration shell of O* at time t, given that it was itself the O* site at time $t = 0$. Including the reverse reaction leads to the rate equation

$$\frac{dC_i^{OO}(t)}{dt} = -k_1^{PT} C_i^{OO}(t) + k_{-1}^{PT} C_{nn}^{OO}(t) \tag{9}$$

Table 3. Various Relaxation Times and Inverse Rates (all given in ps) for OH^-(aq), Excluding Rattling Events, as Defined in the Text, Obtained from the Traditional Mirror Image Mechanism (MIM), the Dynamical Hypercoordination Mechanism (DHM), and the Static Hypercoordination Mechanism (SHM)[a]

mechanism	τ_{exch} $1/k_1^{PT}$	$\tau_{exch}^{OO\text{-}3}$ $\tau_{exch}^{OO\text{-}4}$	$\tau_{fast\text{-}1}$ $\tau_{fast\text{-}2}$	$a_{fast\text{-}1}$ $a_{fast\text{-}2}$	τ_{slow} $1/k_1^{HB\text{-}O^*}$	τ_{fast}^{mm} $1/k_{-1}^{HB\text{-}H'}$
MIM	1.16	0.52	0.11	0.14	2.6	0.11
	0.74	2.50	0.66	0.52	1.9 (2.15)	0.50
DHM	3.20	0.65		0.00	4.0	0.13
	3.20	3.95	0.40	0.06	5.6 (2.20)	0.30
SHM	15.6			0.00	15.0	0.15
	13.8	15.6		0.00	14.0 (1.40)	0.30

[a] Note that the deuterium mass is used for H throughout. The hydrogen bond lifetime for bulk water, $1/k_1^{HB\text{-}O_w}$, is given in parentheses following the $1/k_1^{HB\text{-}O^*}$ data. Based on data from ref 134.

with k_1^{PT} and k_{-1}^{PT} being the forward and backward PT rate constants, respectively.

In the case of charge transport, a second process in which the proton is transferred out of the first solvation shell with a rate constant k_2^{PT} is assumed to occur, and once there is such an event, it is assumed that the proton does not return to the original O* on a time scale shorter than the decay time of $C_i^{OO}(t)$. Under this assumption, a second rate equation for $C_{nn}^{OO}(t)$ can be written down,

$$\frac{dC_{nn}^{OO}(t)}{dt} = -(k_2^{PT} + k_{-1}^{PT})C_{nn}^{OO}(t) + k_1^{PT}C_i^{OO}(t) \tag{10}$$

thus "closing" the complete set of kinetic equations and the solution of eq 9 together with eq 10 yields the following biexponential form

$$C_i^{OO}(t) = \frac{1}{\lambda}[(\lambda - k_1^{PT} + K)e^{-(k_1^{PT}+K-\lambda)t/2} + (\lambda + k_1^{PT} - K)e^{-(k_1^{PT}+K+\lambda)t/2}]$$
$$C_{nn}^{OO}(t) = \frac{k_1^{PT}}{\lambda}[e^{-(k_1^{PT}+K-\lambda)t/2} - e^{-(k_1^{PT}+K+\lambda)t/2}] \tag{11}$$

where

$$\lambda = \sqrt{(k_1^{PT} - K)^2 + 4k_1^{PT}k_{-1}^{PT}} \tag{12}$$

and $K = k_2^{PT} + k_{-1}^{PT}$. Note that the first exponential in each of the correlation functions in eq 11 leads to a slow decay while the second one leads to fast decay. Hence, two time scales naturally emerge from the proposed framework. The forward and backward rate constants k_1^{PT} and k_{-1}^{PT} were obtained using a least-squares fit of the correlation functions to eq 9 in the time interval from $t = 0$ to $t = 6$ ps from the AIMD trajectories of H^+(aq). Since $C_i^{OO}(t)$ and $C_{nn}^{OO}(t)$ both decay according to a biexponential law, then it can be shown that the continuous correlation function $C_c^{OO}(t)$ does as well. Thus, in the proceeding analysis, $C_c^{OO}(t)$ can be fit to a solution of the form

$$C_c^{OO}(t) = a_{slow}e^{-t/\tau_{slow}} + a_{fast}e^{-t/\tau_{fast}} \tag{13}$$

When several solvation shell patterns exist, as is the case with OH^-(aq), then the above theory must be generalized to include rate constants k_{-1,n_j}^{PT} and corresponding correlation functions $C_{nn}^{OO-n_j}(t)$ for each solvation complex with coordination number n_j, where j indexes the number of distinct solvation complexes; note that this idea could be extended to distinguish different solvation shell structures for a given coordination number. The full set of coupled kinetic equations becomes

$$\frac{dC_i^{OO}(t)}{dt} = -k_1^{PT}C_i^{OO}(t) + \sum_{j=1}^{p} k_{-1,n_j}^{PT}C_{nn}^{OO\text{-}n_j}(t)$$
$$\frac{dC_{nn}^{OO\text{-}n_j}(t)}{dt} = -(k_2^{PT} + k_{-1,n_j}^{PT}) + C_{nn}^{OO\text{-}n_j}(t) + k_1^{PT}C_i^{OO}(t), \quad j = 1, ..., p \tag{14}$$

and depends on the number p of such complexes that are taken into account. In the case of OH^-(aq), $p = 2$, corresponding to the 3-fold and 4-fold coordinated complexes. Thus, there are two projected correlation functions $C_{nn}^{OO\text{-}3}$ and $C_{nn}^{OO\text{-}4}$ for $n_1 = 3$ and $n_2 = 4$, and the solution of the three coupled rate equations yields a triexponential form. Together, the above relations define a very general and fairly flexible novel formalism[134] that allows one to study the *kinetics* of structural diffusion in quantitative terms based on lifetimes, relaxation times, and transfer rates.

The average PT rates extracted from this general formalism are found to differ considerably for the three mechanisms according to the data collected in Table 3. Here, proton rattling is excluded, since the primary focus is on the structural diffusion process at this stage. As expected from the previous analyses and mechanistic considerations, the mirror image and static hypercoordination scenarios provide the fastest and slowest rates, respectively, whereas the dynamical hypercoordination mechanism falls in between the two. Within the mirror image scenario, the decay properties of $C_c^{OO}(t)$ as shown in Figure 14a are best described by a linear triexponential ansatz,

$$C_c^{OO}(t) = a_{slow}e^{-t/\tau_{slow}} + a_{fast\text{-}1}e^{-t/\tau_{fast\text{-}1}} + a_{fast\text{-}2}e^{-t/\tau_{fast\text{-}2}} \tag{15}$$

similar to eq 13, with again one slow but two fast relaxation times, τ_{slow}, $\tau_{fast\text{-}1}$, and $\tau_{fast\text{-}2}$, and corresponding weights $a_{slow} + a_{fast\text{-}1} + a_{fast\text{-}2} = 1$. For the mirror image and dynamical hypercoordination scenarios, both fast and slow processes are found with relaxation times in the ranges of $\tau_{fast} \approx 0.5$ ps and $\tau_{slow} = 3-4$ ps, which essentially amount to 1 order of magnitude difference between the two processes. The crucial difference is, however, the weights: the *fast processes* are *negligible* in the case of dynamical hypercoordination, $a_{fast\text{-}1} + a_{fast\text{-}2} = 0.06$, whereas they are *dominant* within the mirror image mechanism $a_{fast\text{-}1} + a_{fast\text{-}2} = 0.66$. In the case of static hypercoordination, there is actually *no fast process* at all; that is, $a_{fast\text{-}1} + a_{fast\text{-}2} \approx 0$ within the statistical accuracy

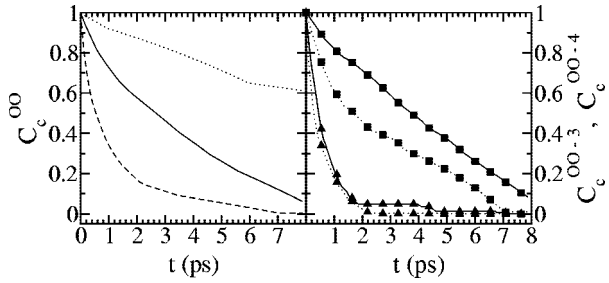

Figure 14. (a, left) Continuous correlation function, C_c^{OO}, of OH^-(aq) obtained from the traditional mirror image mechanism (dashed), the dynamical hypercoordination mechanism (solid), and the static hypercoordination mechanism (dotted). (b, right) Continuous correlation functions of OH^-(aq) for O* accepting exactly three (triangles), C_c^{OO-3}, or four (squares), C_c^{OO-4}, hydrogen bonds at the time origin $t = 0$ obtained from the traditional mirror image mechanism (dashed) and the dynamical hypercoordination mechanism (solid); C_c^{OO-3} could not be determined for the static hypercoordination mechanism due to insufficient statistics (see also text and Table 3). Based on data from ref 134.

of the underlying data, but $\tau_{slow} \approx 16$ ps corresponds to an *extremely slow* relaxation.

Having found such dramatic quantitative differences, the next task is to assign physical processes to these numbers. Guided by the mechanistic insights from section 5.4, the impact of the solvation pattern can now be elucidated in quantitative detail. To facilitate this, the continuous function $C_c^{OO}(t)$ is defined separately for those OH^-(aq) where O* accepts exactly either three or four HBs at time $t = 0$, respectively; these are denoted as C_c^{OO-3} and C_c^{OO-4}, respectively, in Figure 14b. The PT rates extracted, denoted as $1/\tau_{exch}^{OO-3}$ and $1/\tau_{exch}^{OO-4}$, respectively, are compiled in Table 3. Interestingly, upon comparing both τ_{exch}^{OO-4} and τ_{exch}^{OO-3} to the fast and slow processes (i.e., to τ_{fast-1}, τ_{fast-2}, and τ_{slow}), the *slow time scale* τ_{slow} is consistently found to be associated with PT from a *4-fold coordinated* OH^-(aq) with lifetime τ_{exch}^{OO-4} *for all three scenarios*. On the other hand, it is the lifetime τ_{exch}^{OO-3}, and thus the *3-fold coordinated* OH^-(aq) species, that can be linked exclusively to the *fast processes* with time scales τ_{fast-1} and τ_{fast-2}. Most importantly, however, the relation $\tau_{fast} \approx \tau_{exch}^{OO-3} \ll \tau_{exch}^{OO-4} \approx \tau_{slow}$ strongly supports the basic premise of the presolvation concept: PT occurs preferentially if the proton-receiving species is properly solvated *independently* of the particular mechanism (provided, of course, it allows at all for PT events to occur).

In order to correlate these different time scales with more elementary dynamical processes in the liquid, the bulk HB lifetimes, $1/k_1^{HB-O_w}$, which measure the stability of HBs, were obtained *via* the standard procedure.[301] The underlying population correlation functions (see, e.g., ref 301 for definitions) have been calculated from the trajectories of the corresponding neat water simulations in order to avoid artifacts due to the presence of charge defects. The analysis reveals that the HB relaxation of the bulk liquid is quite similar for the three cases according to the lifetimes reported in Table 3 (where these $1/k_1^{HB-O_w}$ data are shown in parentheses). Clearly, such small differences in the bulk HB dynamics cannot explain the vastly different diffusion behavior generated for OH^-(aq) by the three mechanisms. In the next step, the lifetimes of HBs existing (at time $t = 0$) between the defect site, O*, and first shell solvation water only, denoted $1/k_1^{HB-O*}$, were computed in an analogous fashion. Here, within each mechanistic picture, the values of $1/k_1^{HB-O*}$, τ_{slow}, and τ_{exch}^{OO-4} are found to be similar, as the data in Table 3 indicate. This is consistent with the idea that fluctuations of HBs between OH^- and water molecules in its *first shell* drive structural diffusion for both dynamic and static hypercoordination scenarios. However, comparison of the three numbers between the different mechanism pictures shows that they vary considerably. In the static hypercoordination case, for example, this HB lifetime is unusually long, $1/k_1^{HB-O*} \gg 1/k_1^{HB-O_w}$, implying that the first shell is very tightly bound to OH^-. This strongly supports the existence of rather long-lived solvation shell aggregates centered around OH^-, i.e. $[OH^- \cdot (H_2O)_n](aq)$ with $n \approx 4$, and thus a *dominant* contribution of vehicular diffusion in this case. Although hypercoordination is observed in both cases, the first solvation shell around the defect O* is a dynamical object in the successful scenario, whereas it is rigid in the other.

For the mirror image scenario, in stark contrast, the two HB lifetimes exceed by far (and thus do not match) the fast relaxation times observed in this case, $1/k_1^{HB-O_w} \approx 1/k_1^{HB-O*} \gg \tau_{fast-1}$ and τ_{fast-2}. On the other hand, it has already been shown that the fast relaxation times are the dominant contributions to PT in the mirror image mechanism, as $a_{fast-1} + a_{fast-2}$ amounts to more than 60%. Thus, there must be other processes that can be correlated with the PT rate in this case. A much faster process than HB breaking and making is the ultrafast reorientational motion in the solvation shell of OH^-. This is probed by the *short-time* decay contribution to the orientational correlation function, defined by

$$C^{mm}(t) = \frac{\langle \mathbf{m}(t) \cdot \mathbf{m}(0) \rangle}{\langle \mathbf{m}^2 \rangle} \qquad (16)$$

whose decay can be quantified with the associated relaxation time τ_{fast}^{mm}. Here, $\mathbf{m}(t)$ is the purely geometric dipole vector of a water molecule at time t (not to be confused with $\mathbf{M}(t)$ defined in eqs 1 and 2, which must be obtained from electronic structure calculations of the bulk system, *vide infra*), and the average is performed over water molecules found in the first hydration shell of OH^-(aq) at time $t = 0$.

The time scale of reorientation obtained from eq 16 is essentially identical for all three cases, according to Table 3. This underlines once again that the basic HB structure and dynamics of the liquid are similar in each picture. But the crucial observation is that this time scale, τ_{fast}^{mm}, matches only the ultrafast component of the PT rate in the mirror image scenario, τ_{fast-1}, since there is no such ultrafast component at all in the PT kinetics of both dynamic and static hypercoordination. Finally, consider the rate constant for formation of the donated HB involving the hydrogen H′ of OH^-(aq), called $k_{-1}^{HB-H'}$, which is computed from a suitably adapted kinetics formalism. Its inverse is found to match τ_{fast-2} for mirror image and dynamical hypercoordination mechanisms in Table 3; note that the static hypercoordination case only features a slow channel to PT, τ_{slow}. Thus, once the *donated* HB is formed through the OH^- hydrogen, H′, PT is induced by ultrafast reorientational motion of the surrounding water molecules. In other words, the $H' \cdots O_w$ donated HB needs to be formed first to properly presolvate the OH^- before PT can occur. Both these mechanisms are fast processes so that this analysis quantifies, in terms of molecular level kinetics, "...why the simulation rates [*which refer to PW91 and revPBE data reported in the previous paragraph*] are higher than observed experimental rates" (quoted from ref 167) for OH^-(aq) migration according to the mirror image mechanism of ref 167.

Table 4. Various Relaxation Times and Inverse Rates (all given in ps) for OH^-(aq), Including Rattling Events, as Defined in the Text, Obtained from the Traditional Mirror Image Mechanism (MIM), the Dynamical Hypercoordination Mechanism (DHM), and the Static Hypercoordination Mechanism (SHM)[a]

mechanism	τ_{exch} $1/k_1^{PT}$	τ_{exch}^{OO-3} τ_{exch}^{OO-4}	τ_{fast} a_{fast}	τ_{slow} a_{slow}
MIM	0.27	0.08	0.06	0.60
	0.09	0.54	0.61	0.39
DHM	1.35	0.16	0.18	1.70
	0.59	1.55	0.20	0.80
SHM	1.78			1.76
	1.65	1.80	0.00	1.00

[a] Note that the deuterium mass is used for H throughout. Based on data from ref 134.

The full picture is completed by quantifying proton rattling. The data in Table 4 show that the associated time scale is, for all cases, considerably faster when OH^- accepts three HBs in comparison to the 4-fold coordinated state, since $\tau_{exch}^{OO-4} \gg \tau_{exch}^{OO-3}$ always holds; rattling cannot be detected for static hypercoordination within the available statistics, since OH^- is rarely found in the active 3-fold solvated state. Complementary to this decomposition in terms of solvation shell patterns is the decay analysis of $C_c^{OO}(t)$ in the time-domain; a biexponential fit describes all cases satisfactorily, and including a third channel does not yield a distinct third relaxation time. Interestingly, it is found that, for all mechanisms, the slow time scale τ_{slow} closely matches the time τ_{exch}^{OO-4} that 4-fold coordinated complexes spend on average without any PT, be it rattling or real PT contributing to charge defect migration (i.e., mirror image mechanism, 0.60 versus 0.54; dynamical hypercoordination, 1.70 versus 1.55; static hypercoordination, 1.76 versus 1.80). Most important, however, is the observation that only for the mirror image mechanism, are the two time scales τ_{fast} and τ_{slow} (i.e., 0.06 and 0.60) essentially identical to τ_{fast-1} and τ_{fast-2} (i.e., 0.11 and 0.66) found for real PT and thus structural diffusion according to Table 3. This crucial finding implies the unphysical conclusion, pertinent *only* to the mirror image mechanism, that rattling and structural diffusion occur on the *same* time scale within this picture.

The impact systematic errors due to finite system size and fictitious electron mass have on structural and diffusive properties according to the dynamical hypercoordination mechanism has already been shown in section 4.6 not to change the qualitative picture. This cross-checking is made complete in the following by deducing rough error margins on relaxation times and rates of PT by doubling the system size N and by decreasing the fictitious electron mass parameter μ to half its standard value (see Table 5).

In the dynamical hypercoordination of OH^-(aq), the active 3-fold coordinated species features proton rattling on an average time scale in the range of $\tau_{exch}^{OO-3} \approx 160-310$ fs, which compares well with the fast decay component $\tau_{fast} \approx 120-350$ fs of $C_c^{OO}(t)$ (see Table 5). Again, the qualitative picture remains unaltered, although the underlying (ultrafast!) time scales themselves can change easily by a factor of 2. In the 4-fold solvated resting (majority) complex, on the other hand, OH^-(aq) lives on average for about $\tau_{slow} \approx 1.7-2.1$ ps without *any* PT event occurring, which correlates well with the time scale of structural diffusion. Furthermore, the short and long time scales obtained for the relaxation of the 3-fold complexes are $\tau_{fast}^{OO-3} \approx 30-70$ fs and $\tau_{slow}^{OO-3} \approx 220-450$ fs, respectively, whereas these time scales are $\tau_{fast}^{OO-4} \approx 340-420$ fs and $\tau_{slow}^{OO-4} \approx 1.8-2.4$ ps, respectively, for the 4-fold solvation pattern when considering the errors obtained from the biexponential analysis of C_c^{OO-3} and C_c^{OO-4}, respectively. Clearly, the slower component of the 3-fold species is, within the error margins, identical to the faster component of the lifetime of the complexes that accept four HBs. Also here, numbers are found to change, but their relative order, which is relevant for the qualitative mechanistic picture, is not affected.

The extremely short lifetime of about $\tau_{fast}^{OO-3} \approx 50 \pm 20$ fs is quite distinct and is known to result from a very efficient decay of those transiently created OH^-(aq) defects that are properly presolvated for PT upon accepting three HBs (see Figure 12g). There is hope that time-resolved experiments of the sort pioneered previously for H^+(aq) systems[91,92,95,97,98,100,101] together with the use of more dilute solutions will provide clues by which the time scale of approximately 160 fs that has been detected in a quite concentrated 10 M solution of NaOD in D_2O previously[193] can be disentangled; note that this concentration corresponds to a ratio of hydroxide anions to water molecules of about 1:5.2, which is known to decrease the coordination number of the OH^- solvation shell compared to more dilute references.[178,190,197,200] The aforementioned 160 fs time scale has been tentatively assigned to deuteron hopping[193] whereas a different explanation in terms of overtone transitions due to transient $H_3O_2^-$ species is offered in ref 206. Indeed, the observed time scale of 110 fs assigned to such short-lived complexes has been attributed in ref 206 to the time scale of PT, including proton rattling events as predicted in Table 2 of ref 134, i.e. to $\tau_{fast} \approx 180$ fs or $\tau_{exch}^{OO-3} \approx 160$ fs as reprinted in Table 4 of this manuscript. Based on the present assessment of systematic errors (see Table 5), one must consider error intervals of $\tau_{fast} \approx 120-350$ fs and $\tau_{exch}^{OO-3} \approx 160-310$ fs for these time scales, and one must remember that the experimental time scales are expected to be shorter because the present simulations are fully deuterated[134] while the experiments are not. Nevertheless, detecting the fastest time scale possible, i.e. $\tau_{fast}^{OO-3} \approx 50 \pm 20$ fs, arising from the OH^-(aq) defects that accept three HBs as the presolvated precursor to PT, remains a challenge for future ultrafast experiments.

In conclusion, this thorough analysis of various HB, reorientational, solvation shell, and PT dynamics not only confirms but also quantifies in terms of rates and time scales the three different migration mechanisms derived in section 5.4 and depicted in Figure 12. In addition, the presolvation concept[135] applied to OH^-(aq) in section 3 is shown to hold, since it predicts the correct behavior, which is consistent with the extracted microscopic kinetic models for *all* charge transport mechanisms considered in this review. The charge migration kinetics clearly exposes how the microscopic dynamics of the solvation shell around OH^- in water leads to artificially fast and slow structural diffusion of OH^-(aq) in the mirror image and static hypercoordination scenarios, respectively. It also quantifies how the intricate solvent shell dynamics govern the conversion of the resting majority state (which accepts four HBs in a roughly square-planar arrangement) to the active state ready for PT (which accepts only three HBs but in a tetrahedral arrangement), according to the dynamical hypercoordination mechanism. It is this solvation shell dynamics that allows for faster diffusion of OH^-(aq) compared to the self-diffusion of water (in contrast to static hypercoordination) but at the same time limits the rate of structural diffusion (in contrast to mirror image

Table 5. Various Relaxation Times and Inverse Rates (all given in ps) for OH^-(aq) Including Rattling Events as Defined in the Text Obtained from the Dynamical Hypercoordination Mechanism Comparing a Larger System Size N and a Smaller Fictitious Electron Mass μ to the Standard Parameter Setting ($N = 31$ water molecules and $\mu = 800$ au) Reported in the First Row[a]

parameter	τ_{exch} $1/k_1^{PT}$	$\tau_{exch}^{OO\text{-}3}$ $\tau_{exch}^{OO\text{-}4}$	τ_{fast} τ_{slow}	$\tau_{fast}^{OO\text{-}3}$ $\tau_{slow}^{OO\text{-}3}$	$\tau_{fast}^{OO\text{-}4}$ $\tau_{slow}^{OO\text{-}4}$
$N = 31, \mu = 800$	1.35	0.16	0.18 (0.20)	0.05 (0.42)	0.40 (0.18)
	0.59	1.55	1.70 (0.80)	0.22 (0.58)	1.80 (0.82)
$N = 63, \mu = 800$	1.70	0.27	0.35 (0.20)	0.03 (0.12)	0.42 (0.25)
	1.00	1.90	2.10 (0.80)	0.30 (0.88)	2.40 (0.75)
$N = 31, \mu = 400$	1.64	0.31	0.12 (0.10)	0.07 (0.46)	0.34 (0.05)
	0.98	1.80	1.80 (0.90)	0.45 (0.54)	1.90 (0.95)

[a] Note that the deuterium mass is used for H throughout. The weights a_i obtained by biexponential fits are given in parentheses; see text for details. Based on data from ref 134.

solvation). This is the underlying reason why dynamical hypercoordination solvation predicts diffusion coefficients of OH^- versus H^+(aq) versus self-diffusion of water in accord with experimental mobility data presented in section 3.5 and analyzed in section 5.3. Last but not least, the detailed kinetics data reported in the tables of this section are expected to help in guiding analyses of future time-resolved ultrafast spectroscopic experiments of OH^-(aq) such as those performed earlier for H^+(aq) systems.[91,92,95,97,98,100,101] A promising first step in this direction are recent time-resolved pump−probe and two-dimensional IR experiments,[206] in which a measured femtosecond decay time has been correlated with a particular microscopic time scale for PT events in OH^-(aq) as predicted in ref 134.

5.6. Rotational Relaxation

The rotational motion of a molecule in bulk solution can be determined experimentally by measuring the following rotational anisotropy function[308]

$$r(t) = \frac{S_{||} - S_{\perp}}{S_{||} + 2S_{\perp}} \tag{17}$$

where $S_\perp$ and $S_{||}$ are signals measured in directions perpendicular and parallel to the pump polarization. In the absence of couplings between molecular rotations and other degrees of freedom and for a long enough time delay between the pump and probe pulses so as to avoid any overlap between them, this rotational anisotropy function can be expressed in terms of a rotational correlation function as follows[309]

$$r(t) = 0.4C_2(t) \tag{18}$$

where $C_2(t) = \langle P_2(\mathbf{u}(0)\cdot\mathbf{u}(t))\rangle$; here $P_2(x)$ is the second-rank Legendre polynomial, $P(x) = (3x^2 - 1)/2$, and $\mathbf{u}(t)$ is the unit vector along the molecular vector of interest, so that $\mathbf{u}(0)\cdot\mathbf{u}(t) = \cos\theta(t)$ defines the angle between this vector at times 0 and t (which is the O−H axis of the hydroxide ion in the following).

Quite recently, a spectroscopic study of the temporal decay of the rotational anisotropy of OH^- in water has been carried out[67] and yielded a time constant of 1.9 ps for the long-time decay of $r(t)$. In addition, recent time-dependent vibrational spectroscopic studies have reported time scales of 2.6 ps[310−312] and 3.0 ps[313] for the long-time rotation of HOD in (pure) light and heavy water, respectively. Considering that the above long-time values carry a weight of about 80−85%[310,312] and that the short-time inertial relaxation occurs very fast with a time scale in the range of 100 fs or less,[311] the above long-time results for liquid water are consistent with earlier NMR relaxation studies which reported a time scale of approximately 2 ps for the integrated relaxation time of rotational motion in light water.[314−316] Hence, for the *long-time* diffusive part of the dynamics, OH^- in water shows a *faster* rotational relaxation than that of water molecules in the bulk.

Table 6. Rotational Relaxation Times (weights) of OH^-(aq) and Bulk Water Molecules (all given in ps) Obtained from the Traditional Mirror Image Mechanism (MIM), the Dynamical Hypercoordination Mechanism (DHM), and the Static Hypercoordination Mechanism (SHM)[a]

quantity	MIM	DHM	SHM	experiment
$\tau_{r\text{-}fast}^{OH^-}$ ($a_{r\text{-}fast}^{OH^-}$)	0.18 (0.24)	0.12 (0.12)	0.05 (0.07)	
$\tau_{r\text{-}slow}^{OH^-}$ ($a_{r\text{-}slow}^{OH^-}$)	3.05 (0.16)	6.70 (0.28)	17.50 (0.33)	1.9
$\tau_{r\text{-}fast}^{H_2O}$ ($a_{r\text{-}fast}^{H_2O}$)	0.08 (0.08)	0.10 (0.10)	0.11 (0.10)	
$\tau_{r\text{-}slow}^{H_2O}$ ($a_{r\text{-}slow}^{H_2O}$)	17.50 (0.32)	11.50 (0.30)	5.75 (0.30)	2.6
$\tau_{r\text{-}slow}^{OH^-}/\tau_{r\text{-}slow}^{H_2O}$	0.17	0.58	3.04	0.73

[a] Note that the deuterium mass is used for H throughout. The rotational relaxation times of water molecules in the bulk are obtained from separate pure bulk water simulations. The experimental values of hydroxide and water rotational relaxation correspond to those of OH^- (ref 67) and HOD in light water,[310−312] respectively. Note that $a_{r\text{-}fast} + a_{r\text{-}slow} = 0.4$, in order to satisfiy eq 18. Based on trajectories from ref 134.

In order to compare the predictions of the three different charge migration mechanisms to experimental data, the decay constants τ_r of the rotational anisotropy of OH^-(aq) have been obtained from eq 18, as summarized in Table 6. In addition to calculating the rotational relaxation time of hydroxide in water, we have obtained the corresponding rotational relaxation time of the water molecules from analogous pure water simulations. Since the calculated decay of $r(t)$ includes both short-time inertial and long-time diffusive relaxation, the entire decay has been fit to a biexponential function of the form

$$r(t) = a_{r\text{-}fast}e^{-t/\tau_{r\text{-}fast}} + a_{r\text{-}slow}e^{-t/\tau_{r\text{-}slow}} \tag{19}$$

such that $a_{r\text{-}fast} + a_{r\text{-}slow} = 0.4$, thus satisfying eq 18. The calculated relaxation times and associated weights for the mirror image, dynamical hypercoordination, and static hypercoordination mechanisms are included in Table 6, where they are also compared to the available experimental results. Note that the theoretical results of OH^- rotation are obtained by excluding the rattling effects. In fact, as in the case of translational diffusion, inclusion of such rattling effects only alters the short-time part of the rotational dynamics, while the long-time diffusive part of the dynamics, which is the main focus of this section, remains essentially unaltered. It should also be noted that the rotational times obtained for

Table 7. Rotational Relaxation Times (weights) of OH^-(aq) and Bulk Water Molecules (all given in ps) Obtained from the Dynamical Hypercoordination Mechanism Comparing a Larger System Size N and a Smaller Fictitious Electron Mass μ to the Standard Parameter Setting ($N = 31$ water molecules and $\mu = 800$ au) Reported in the Second Column[a]

quantity	$N = 31/\mu = 800$	$N = 63$	$\mu = 400$
$\tau_{r\text{-}fast}^{OH^-}$ ($a_{r\text{-}fast}^{OH^-}$)	0.12 (0.12)	0.05 (0.08)	0.04 (0.07)
$\tau_{r\text{-}slow}^{OH^-}$ ($a_{r\text{-}slow}^{OH^-}$)	6.70 (0.28)	3.80 (0.32)	5.72 (0.33)
$\tau_{r\text{-}fast}^{H_2O\text{-}same}$ ($a_{r\text{-}fast}^{H_2O\text{-}same}$)	0.14 (0.10)	0.10 (0.07)	0.10 (0.08)
$\tau_{r\text{-}slow}^{H_2O\text{-}same}$ ($a_{r\text{-}slow}^{H_2O\text{-}same}$)	9.80 (0.30)	10.90 (0.33)	10.10 (0.32)
$\tau_{r\text{-}slow}^{OH^-}/\tau_{r\text{-}slow}^{H_2O\text{-}same}$	0.68	0.35	0.57

[a] Note that the deuterium mass is used for H throughout. The $\tau_r^{H_2O\text{-}same}$ and $a_r^{H_2O\text{-}same}$ data are obtained from the dynamics of the tagged "nonsolvation shell water molecules" in the simulations that include the hydroxide ion defect. Note that $a_{r\text{-}fast} + a_{r\text{-}slow} = 0.4$ in order to satisfiy eq 18. Based on trajectories from ref 134.

pure bulk water are in accord with those reported earlier for the same functional.[317]

As for the case of translational diffusion analyzed in section 5.3, the computed rotational diffusion of water itself is slower than is found experimentally. Once again, therefore, the more meaningful quantity to compare to experiment is the *ratio* of the rotational constants of OH^- and H_2O, i.e. $\tau_{r\text{-}slow}^{OH^-}/\tau_{r\text{-}slow}^{H_2O}$, as given in the last row of Table 6. It is clear from this table that only the dynamical hypercoordination mechanism provides a ratio for the rotational relaxation times that is meaningful when compared to experiments. This is in stark contrast to the mirror image scenario, which predicts a significantly smaller value for this ratio. Not unexpectedly, the static hypercoordination leads to a value that is clearly too large. In conclusion, rotational motion of OH^- in water is much too fast in the mirror image picture and too slow in the static hypercoordination scenarios, which is consistent with the findings from the kinetics analysis.

We further note that structural diffusion allows OH^-(aq) to rotate much more efficiently compared to simple molecular anions in water because the orientation of the O−H axis necessarily changes significantly during each PT event, as evidenced by panels e−h in Figure 2 or Figure 12, as a result of charge migration. Since few orientational changes are expected to occur when OH^-(aq) stays as a hypercoordinated species, while major reorientation does take place during structural diffusion, it is expected that the slower diffusive component of the reorientational time of OH^- would roughly correspond to the lifetime of the hydrated OH^-(aq) in its resting state, i.e. the time spent when OH^- accepts four HBs in a roughly square-planar arrangement, as depicted in Figure 4a, before it undergoes PT. This is indeed found to be the case for all three scenarios investigated, where the relation $\tau_{r\text{-}slow}^{OH^-} \approx \tau_{slow} \approx \tau_{exch}^{OO\text{-}4}$ holds to a good extent (see Tables 3 and 6). This underlines the internal consistency of these vastly different analyses of the dynamics; however, one must keep in mind that the lifetime $\tau_{exch}^{OO\text{-}4}$ of this resting state, being inactive with respect to PT, is much too short in the mirror image picture and too long in the static hypercoordination scenario.

Finally, the effects of finite system size N and finite fictitious electronic mass μ on the rotational relaxation times of OH^-(aq) are investigated for the dynamical hypercoordination mechanism in Table 7, as done before for the diffusion and kinetics analyses. Since separate pure bulk water simulations are only available for the so-called "standard setup" as defined in section 4.3, the rotational relaxation times of water molecules have been obtained from those molecules which are outside the solvation shell of OH^- in the simulations that include the hydroxide ion defect. This is a good approximation, in view of the fact that these values are close to those obtained from separate pure bulk water simulations within the standard setup, i.e. $\tau_{r\text{-}fast}^{H_2O\text{-}same} = 0.14$ ps $\approx \tau_{r\text{-}fast}^{H_2O} = 0.10$ ps and $\tau_{r\text{-}slow}^{H_2O\text{-}same} = 9.8$ ps $\approx \tau_{r\text{-}slow}^{H_2O} = 11.5$ ps (data from Tables 7 and 6, respectively). As before, it is seen that the relaxation times and especially the ratios of the rotational relaxation times of hydroxide and water molecules change only insignificantly for the larger system or for the system with the smaller fictitious electronic mass, when compared to those obtained with the standard setup using $N = 31$ and $\mu = 800$ au.

This analysis supports the main conclusions drawn above regarding the vastly different rotational relaxation time of OH^-(aq) relative to that of the water molecules according to the mirror image, dynamical hypercoordination, and static hypercoordination mechanisms. In particular, rotational relaxation of OH^-(aq) is much too fast within the mirror image scenario and exceedingly slow for static hypercoordination, whereas it is consistent with experimental data for the dynamical hypercoordination mechanism.

6. Examining Dynamical Hypercoordination: The Role of Quantum Effects, Microsolvation, and Counterions

The discussion thus far has focused on the elucidation of the dynamics and the role of particular solvation complexes in the structural diffusion mechanism aided by the presolvation concept. In this section, the possible influence of nuclear quantum effects both in the bulk[135] and on microsolvated clusters[261] will be assessed, and the bulk and clusters cases will be compared to each other. We will also investigate the influence of counterions[178] on both the solvation and charge transport dynamics of hydroxide in bulk solution. Quantifying quantum effects is useful in view of the well-known but still surprising observation that the H/D isotope effects on conductivity, mobility, and diffusion coefficients[1] as well as on the underlying PT rates[87] are *larger in basic solutions* than in acidic solutions (see section 3 for the pertinent numbers). From simulations that include nuclear quantum effects, it is possible to compare in detail the solvation structure and PT free energy of OH^-(aq) relative to those of H^+(aq). In addition, it is instructive to investigate how the hydroxide and hydronium ions behave once they are microsolvated with a single water molecule, i.e. $OH^-\cdot(H_2O)$ and $H_3O^+\cdot(H_2O)$ in the gas phase. These complexes are particularly useful, as their symmetry allows for facile PT between the involved molecular moieties. This will provide insights into how the free energy profile along the PT coordinate δ, and thus the effective PT barrier, changes upon full solvation of both OH^- and H^+ in the aqueous liquid phase. Finally, assessment of concentration effects on the OH^-(aq) system and into possible perturbations of IR spectra induced by counterions is necessary in order to address claims in the literature which connect the presence of certain features in measured IR spectra to specific structural and mechanistic ideas. All these investigations are only carried out for the scenario that is consistent with experimental data, i.e. the dynamical hypercoordination mechanism.

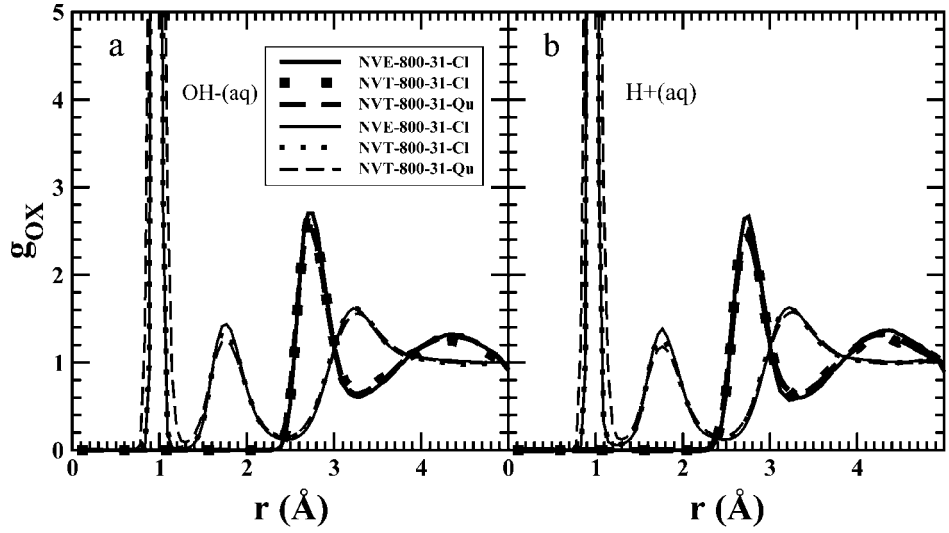

Figure 15. Radial distribution functions, $g(r)$, of OH^-(aq) obtained from the dynamical hypercoordination mechanism and of H^+(aq) in the left and right panels, respectively, with reference to all oxygen atoms using the (standard) classical microcanonical ensemble (solid), the classical canonical ensemble (dotted), and the quantum canonical ensemble (dashed), where thick and thin lines refer to X = O and X = H partner atoms, respectively. Based on data from refs 16, 120, 122, 134, and 135.

6.1. Nuclear Quantum Effects: Zero-Point Motion and Tunneling in OH^-(aq) versus H^+(aq)

The analysis of radial distribution functions can serve as a first step to look into quantum effects. Consider Figure 15, which shows the radial distribution functions g_{OO} and g_{OH}, involving all O−O and O−H pairs in the OH^-(aq) and H^+(aq) solutions in panels a and b, respectively. The major difference between the quantum and classical canonical data of both the OH^-(aq) and H^+(aq) systems lies in the intramolecular OH peak close to 1 Å. This peak is broader and less sharp in the quantum case, which is simply due to quantum-mechanical zero-point vibrations, i.e. an expected and relatively trivial quantum dispersion effect. It is noted in passing that this effect is, of course, even more pronounced for the H−H correlations themselves, which are not shown here. Furthermore, both the *overall* g_{OO} and g_{OH} distribution functions are very similar for OH^-(aq) and H^+(aq), including the peak heights. This shows that the perturbation of the *overall radial structure* due to these two different types of charge defects is not that pronounced at concentrations involving 31 water molecules and one OH^- or 32 waters and one H^+. In addition, the radial distribution functions between the classical AIMD simulations obtained for both OH^-(aq) and H^+(aq) in the microcanonical *NVE* ensemble[16,134] (using the deuterium mass for H) and the classical data obtained several years earlier in the canonical *NVT* ensemble[120,122,135] (using the hydrogen mass for H) with massive Nosé−Hoover chain thermostatting,[280] both at room temperature, are essentially identical.

This picture, and thus the comparison, becomes richer when the conditional radial distribution functions of the OH^-(aq) and H^+(aq) defects in their active and resting states are analyzed. These distributions are obtained by considering again the $|\delta| \leq 0.1$ Å and $|\delta| \geq 0.5$ Å limiting cases, respectively. These functions are shown in Figure 16 with reference to the proton-receiving oxygen, which is O* for OH^-(aq) in the left panels and $\bar{O}$ for H^+(aq) in the right panels, according to the labeling convention in Figure 2a and the definition from section 5.1. The opposite case, i.e. the proton-donating oxygen being $\bar{O}$ for OH^-(aq) and O* for H^+(aq) in the left and right panels, respectively, is presented in Figure 17. Clearly, the solvation pattern of OH^-(aq) and H^+(aq) is different in both limits. This is nicely demonstrated by means of the running coordination numbers $n(r)$ in the two limiting cases, i.e. $|\delta| \leq 0.1$ Å and $|\delta| \geq 0.5$ Å in the upper and lower panels, respectively. The HB donated by the hydroxyl H′ to the oxygen site O_w of a nearby water molecule is analyzed in Figure 8. This analysis illustrates the point that the probability of finding this particular HB increases between the resting state (see Figure 4a for a representative snapshot) shown in panel b and the active complex (see Figure 4b) in the $|\delta| \approx 0$ limit in the left panel a. Although not a strong effect, quantum fluctuations actually increase this difference slightly by washing out the small peak around 2 Å to a shoulder in the $|\delta| \gg 0$ regime. Overall, the influence of nuclear quantum effects on the structure of both defects in aqueous solution turns out to be rather weak, as convincingly demonstrated by Figures 16, 17, and 8.

In contrast to their effect on structural properties, quantum fluctuations have a more pronounced influence on the free energetics of PT along HBs (see ref 285 for a systematic *ab initio* path integral study on PT in the bulk solid and ref 318 for a systematic experimental assessment of IR-spectroscopic consequences using finite systems in the gas phase). In Figure 18, the free energy profile of PT along the δ coordinate is shown for OH^-(aq) in the upper left panel. The classical free energy profile possesses a barrier of approximately 1.3 kcal/mol, i.e. about $2k_BT$ units at 300 K, which is reduced to roughly 0.3 kcal/mol in the quantum free energy profile.[135] This implies that the classical value is about twice the thermal energy under ambient conditions, whereas the quantum barrier is only half that value under the same conditions. Despite this significant reduction due to quantum effects, the quantum free energy profile still retains a substantial double-well character, contrary to the H^+(aq) case[122] depicted in the upper right panel. In the acidic solution there is basically no barrier to proton motion between O* and $\bar{O}$ within the statistical accuracy; in the classical limit, this barrier is close to the thermal energy, ≈0.6 kcal/mol. Thus, at the quantum level, the H^+ topological defect cannot be characterized entirely in terms of either Zundel (i.e., $|\delta| \leq 0.1$ Å) or Eigen

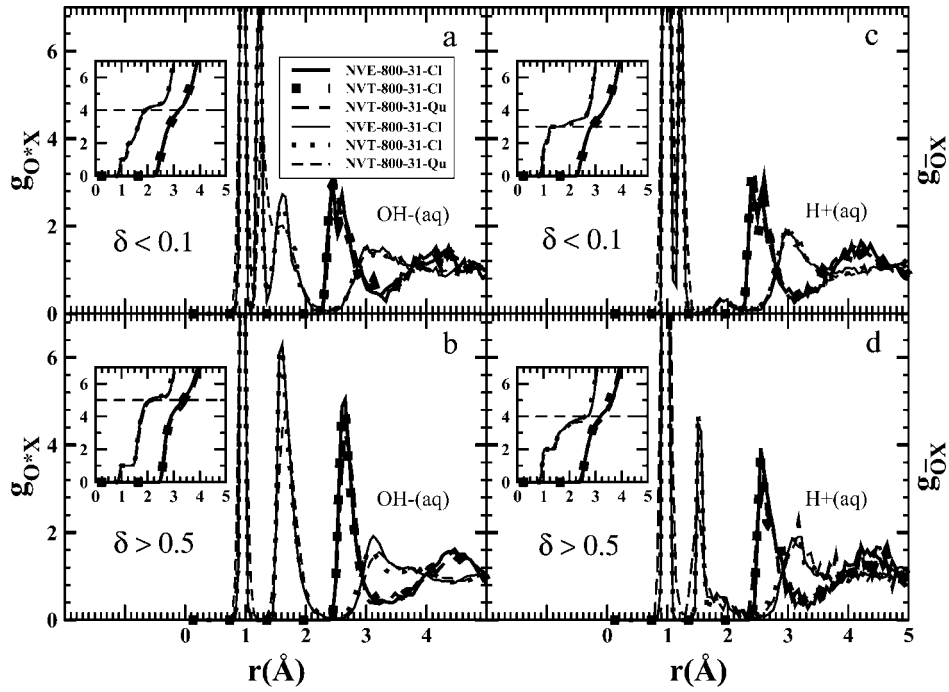

Figure 16. Radial distribution functions, $g(r)$, of OH^-(aq) obtained from the dynamical hypercoordination mechanism and of H^+(aq) in the left and right panels, respectively, for $|\delta| \leq 0.1$ Å and for $|\delta| \geq 0.5$ Å in the top and bottom panels, respectively, using the (standard) classical microcanonical ensemble (solid), the classical canonical ensemble (dotted), and the quantum canonical ensemble (dashed). In both cases, the functions are shown with reference to the *proton-receiving oxygen* upon PT, which is O* for OH^-(aq) and $\bar{O}$ for H^+(aq), where thick and thin lines refer to X = O and X = H partner atoms, respectively; see the caption of Figure 2a and section 5.1 for definitions and labeling conventions. The insets show the corresponding running coordination numbers, $n(r)$, where the dashed horizontal lines mark the preferred coordination numbers in the first solvation shell of the state where $|\delta| \leq 0.1$ Å (i.e., n equals four in OH^-(aq) and three in H^+(aq)) and the state where $|\delta| \geq 0.5$ Å (i.e., n equals five in OH^-(aq) and four in H^+(aq)) in the top and bottom panels, respectively. Based on data from refs 16, 120, 122, 134, and 135.

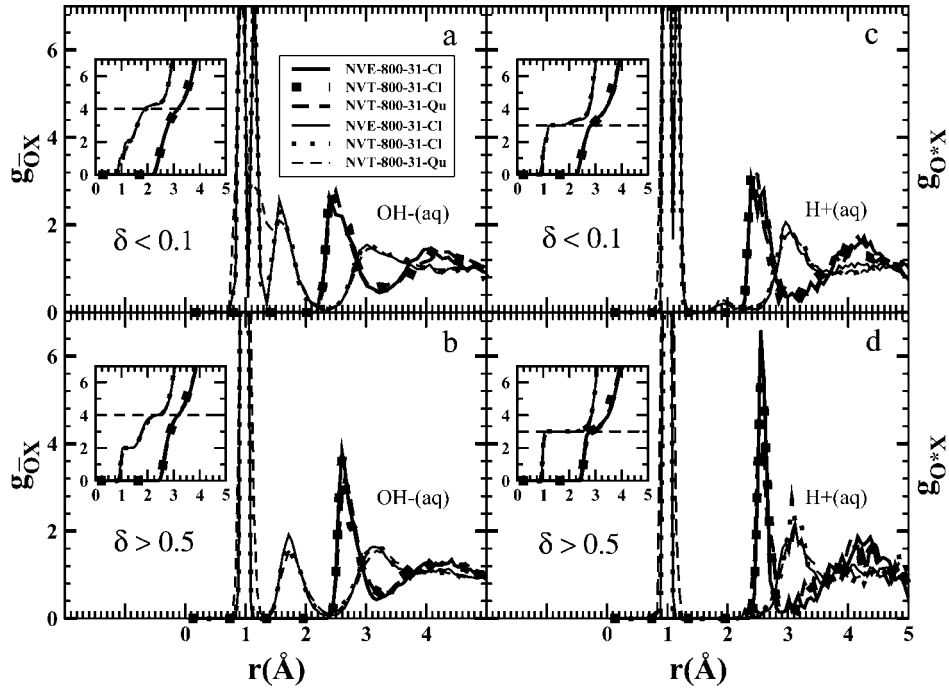

Figure 17. Radial distribution functions, $g(r)$, of OH^-(aq) obtained from the dynamical hypercoordination mechanism and of H^+(aq) in the left and right panels, respectively, for $|\delta| \leq 0.1$ Å and for $|\delta| \geq 0.5$ Å in the top and bottom panels, respectively, using the (standard) classical microcanonical ensemble (solid), the classical canonical ensemble (dotted), and the quantum canonical ensemble (dashed). In both cases, the functions are shown with reference to the *proton-donating oxygen* upon PT, which is $\bar{O}$ for OH^-(aq) and O* for H^+(aq), where thick and thin lines refer to X = O and X = H partner atoms, respectively; see the caption of Figure 2a and section 5.1 for definitions and labeling conventions. The insets show the corresponding running coordination numbers, $n(r)$, where the dashed horizontal lines mark the preferred coordination numbers in the first solvation shell of the state where $|\delta| \leq 0.1$ Å (i.e., n equals four in OH^-(aq) and three in H^+(aq)) and the state where $|\delta| \geq 0.5$ Å (i.e., n equals four in OH^-(aq) and three in H^+(aq)) in the top and bottom panels, respectively. Based on data from refs 16, 120, 122, 134, and 135.

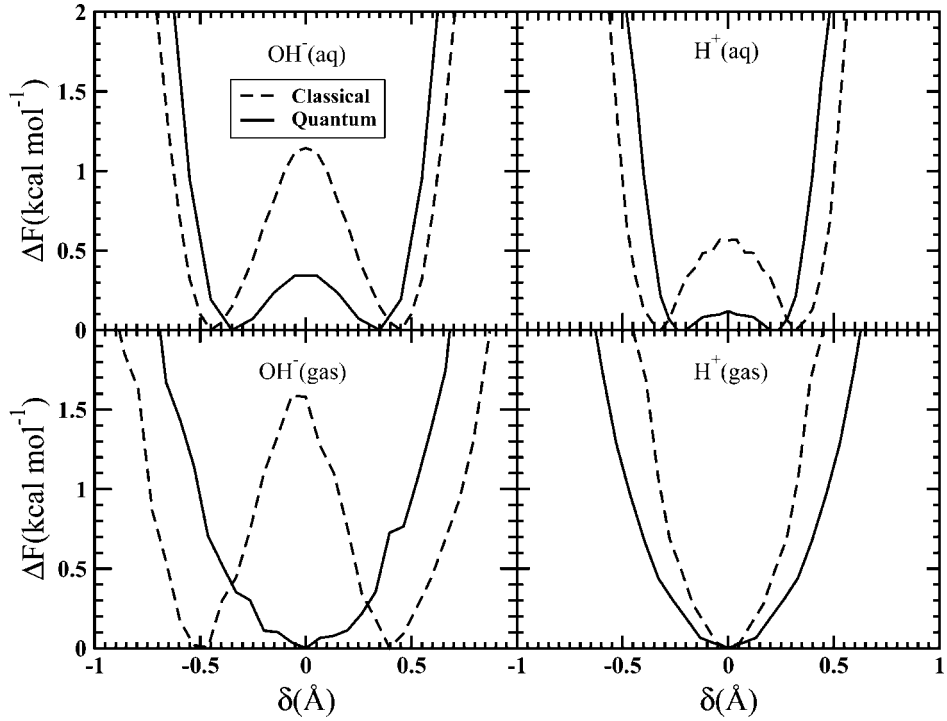

Figure 18. Canonical (Helmholtz) free energy profile at 300 K along the proton transfer coordinate δ of the OH^- and H^+ systems in the left and right panels, respectively, using the classical canonical ensemble (dashed) and the quantum canonical ensemble (solid). The condensed phase data of OH^-(aq) obtained from the dynamical hypercoordination mechanism and of H^+(aq) are shown in the top panels whereas the gas phase data of the corresponding $OH^-\cdot(H_2O)$ and $H_3O^+\cdot(H_2O)$ microsolvation complexes corresponding to $[HO\cdots H\cdots OH]^-$ and $[H_2O\cdots H\cdots OH_2]^+$, respectively, are shown in the bottom panels. Note that the thermal energy is $k_BT \approx 0.6$ kcal/mol at 300 K. Based on data from refs 120, 122, 135, and 261.

($|\delta| \geq 0.5$ Å) cations but interconverts the complexes in a barrierless fashion, thus approaching them only in the sense of idealized or limiting structures.[120]

The free energy characteristics highlight another of the striking differences between the acidic and basic cases, and thus structural diffusion of OH^-(aq) and H^+(aq). Most importantly, the free energy difference has a profound implication on the character of the proton-centered complexes at $\delta \approx 0$ Å, viz. the free energy maximum in OH^-(aq), implying that the $H_3O_2^-$ complex is a short-lived, transient complex.[135] In the acidic case, on the other hand, the Zundel complex $H_5O_2^+$ is clearly not a transition state, but the defect is highly "fluxional" instead.[120] This contradicts the mirror image picture, wherein the $H_3O_2^-$ complex is postulated to be a relatively stable complex analogous to the $H_5O_2^+$ complex in the H^+(aq) case, which would imply the presence of a *minimum* in the free energy surface around $\delta \approx 0$ Å instead of the observed *local maximum*.

Based on the free energy profiles, can we rationalize the fact that the H/D isotope effects on diffusion coefficients reported in section 3.5 are more pronounced for OH^-(aq) than for H^+(aq)? For OH^-(aq), assuming a fluctuation occurs that places the system in the active $H_7O_4^-$ state shown Figure 4b, PT from a first solvation shell water molecule to the OH^- through one of the HBs in this complex will still be unfavorable unless the newly formed water molecule has the correct bend angle of ≈104°. If rigorously true, this would require this $H_7O_4^-$ complex to be in an "ideal" tetrahedral structure before the proton could transfer. Following this idea, it is clear that not only is the PT coordinate δ defined in section 5.1 needed for characterizing the PT process but also the angle θ between the O*−H′ and O*−$\bar{O}$ vectors. In Figure 19, the two-dimensional probability distribution function $P(\delta, \theta)$ based on the data from ref 135 is shown for quantum and classical nuclei in panels a and b, respectively. As can be seen in the figure, the simulation using classical nuclei leads to a significant "funneling" of the angle θ as $|\delta| \rightarrow 0$ into a narrow region around 104°. In the calculation with quantum nuclei, this funneling is much less pronounced, suggesting that quantum effects lead to a finite probability for the proton to transfer even if the structure of the $H_7O_4^-$ complex is not in an ideal tetrahedral geometry. Such a pronounced "corner-cutting"[135] has no analog in the acidic case and could possibly explain the more significant lowering of the effective PT free energy barrier for OH^-(aq) versus H^+(aq) upon inclusion of quantum effects on nuclear motion (compare the upper left to the upper right panel in Figure 18). Although explicit isotopic substitution simulations were not performed, we suggest that the observed differences between the quantum and classical results could relate to the fact that H/D isotope effects on PT rates, $k_\pm$, are larger for OH^-(aq) than for H^+(aq).

In conclusion, nuclear quantum effects are seen to influence the PT free energetics and, consequently, the relative stability and lifetimes of proton-centered complexes. Despite these effects, quantum fluctuations do not change the essential picture of the structural diffusion process for either the acidic or basic and acidic solution cases. This suggests that AIMD simulations using classical nuclei, beginning with those first carried out in the early 1990s,[102−104] retain their utility as a tool to investigate qualitatively the structure of charge defects in aqueous solution.

6.2. Condensed Phase Effects: OH^- and H^+ in Solution versus Microsolvation

It has been suggested that small clusters, consisting of an OH^- or H_3O^+ core ion microsolvated by a few water

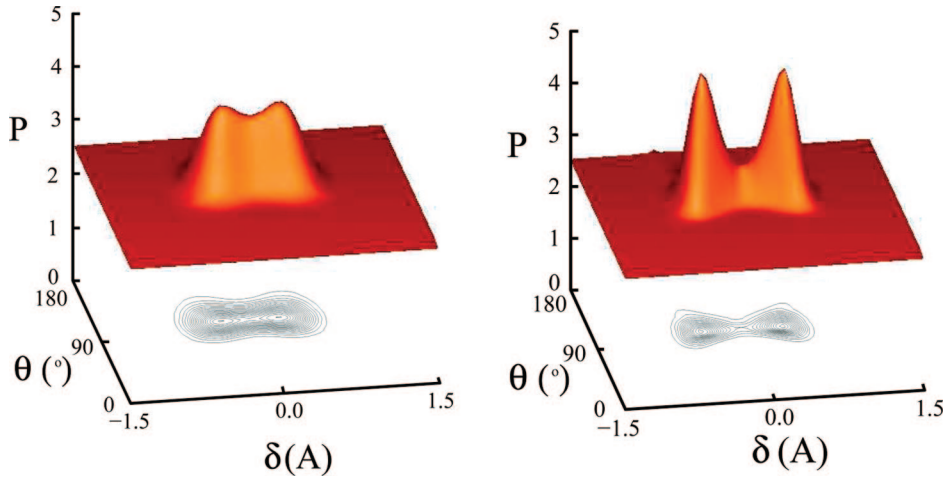

Figure 19. Normalized two-dimensional probability distribution function, $P(\delta, \theta)$, of the proton transfer coordinate, δ, and the angle, θ, between the OH^- covalent bond axis and the O*−O vector for quantum (a, left) and classical (b, right) simulations of $OH^-(aq)$ obtained from the dynamical hypercoordination mechanism; see the caption of Figure 2a and section 5.1 for definitions and labeling conventions. Reprinted with permission from ref 135. Copyright 2002 Nature Publishing Group.

molecules in the gas phase, can be used to draw conclusions about the bulk solvation and charge migration properties of $OH^-(aq)$ and $H^+(aq)$, respectively. Various experimental and theoretical studies on the solvation of OH^- have been based on this assumption, explicitly or implicitly, such as those reported in refs 187, 195, 221−223, and 226 to name just a few. In this section, the influence of the condensed phase environment on the PT free energy is examined first for the most extreme cases of single OH^- or H_3O^+ ions hydrogen-bonded to one water molecule in a vacuum, i.e. $OH^-\cdot(H_2O)$ and $H_3O^+\cdot(H_2O)$, which correspond to the negative and positive Zundel-type complexes $H_3O_2^-$ and $H_5O_2^+$, respectively. These are denoted schematically as $[HO\cdots H\cdots OH]^-$ and $[H_2O\cdots H\cdots OH_2]^+$. Clearly, one cannot expect these minimally hydrated examples to represent true microsolvation studies that use half a dozen or more water molecules (see refs 187, 195, 221−223, and 226), but it is, nevertheless, instructive to compare minimally solvated complexes to the full bulk in order to assess the role of solvent fluctuations. Following this comparison, we will examine the influence of microsolvation on the PT mechanism itself using an $OH^-(H_2O)_n$ cluster with $n = 6$ water molecules based on recent AIMD simulations.[211]

The free energy profiles along the δ coordinate, which describe proton motion along the single HB in the minimally solvated $H_3O_2^-$ and $H_5O_2^+$ complexes in vacuum,[261] are shown in the left and right bottom panels of Figure 18, respectively. It is instructive to compare the bulk solvation free energy profiles of $OH^-(aq)$ in the upper-left panel with those of $H_3O_2^-$ in the gas phase at 300 K (see lower-left panel of Figure 18). In the gas phase, there exists a free energy barrier of approximately 1.6 kcal/mol along the classical PT free energy profile in the $H_3O_2^-$ complex at room temperature, where $k_BT \approx 0.6$ kcal/mol; the underlying bare (Born−Oppenheimer) energy barrier obtained from structure optimization is only ≈0.14 kcal/mol within the same level of electronic structure theory according to ref 261. However, this barrier at $\delta = 0$ was shown in ref 261 to disappear completely if nuclear quantum effects are considered; that is, the local maximum turns into a global minimum at $\delta = 0$ in the quantum free energy profile at 300 K (see the solid line in the upper-left panel of Figure 18). We note, in passing, that this early prediction has been confirmed from the one-dimensional ground-state nuclear wave function along this HB obtained *via* sophisticated coupled cluster calculations.[319] These calculations show that the ground state is energetically located above the bare barrier of 0.9 ± 0.3 kJ/mol (corresponding to about 0.2 kcal/mol). More recent *ab initio* path integral simulations,[320] explicit full-dimensional quantum dynamics calculations,[321,322] and a combined experimental−theoretical study[323] all support the predicted[261] HB centering ("symmetrization") of bare $H_3O_2^-$ due to quantum fluctuation effects.

In contrast to the case of the gas phase, there is a non-negligible free energy barrier to PT of roughly 0.3 kcal/mol at room temperature and, therefore, an underlying double-well structure when both bulk solvation and nuclear quantum effects are included (see the upper left panel in Figure 18). Thus, the full picture is a rather intricate one: (i) the Born−Oppenheimer potential energy surface of $OH^-\cdot(H_2O)$ in a vacuum features a double-well character, a small but finite (Born−Oppenheimer) barrier, and the usual (asymmetric) HB as its equilibrium structure; (ii) the barrier *increases* in a vacuum when thermal (classical) fluctuations are included at room temperature, yielding a much more pronounced double-well PT free energy profile and asymmetric HB; (iii) the (free energy) barrier vanishes in a vacuum after adding quantum fluctuations at 300 K, which leads to a single-well profile and thus to HB symmetrization or centering phenomenon (i.e., the proton is preferentially located at the midpoint of the HB at $\delta = 0$ rather than near one of the two oxygens); (iv) finally, in the condensed phase, a (quantum free energy) barrier for $OH^-(aq)$ emerges which again leads to a double-well PT profile as a result of the intricate interplay of quantum, thermal, and bulk solvation effects.

The upper and lower right panels in Figure 18, corresponding to the condensed and gas phases, respectively, suggest that the H^+ case is slightly less involved. The main features of these panels are as follows: (i) the Born−Oppenheimer potential energy surface $H_3O^+\cdot(H_2O)$ in a vacuum exhibits a single-well structure without any (Born−Oppenheimer) barrier and thus a symmetric or centered HB; (ii) thermal (classical) fluctuations at room temperature still support a single-well (free energy) profile and thus a centered HB; (iii) adding quantum fluctuations at 300 K does not change the picture but just adds more broadening; (iv) finally, in the condensed phase, the quantum PT profile turns out to

be relatively flat and anharmonic around $\delta = 0$, thus causing the "Eigen ⇔ Zundel fluxionality" of H^+(aq) (see section 2 and Figure 1 in particular) due to the interplay of quantum, thermal, and bulk solvation effects.

Comparing the gas and condensed phase results emphasizes the importance of solvent polarization effects[108,111,147−151] for H^+(aq) and, especially, for OH^-(aq). The comparison raises general concerns when microsolvated cluster studies are used to extrapolate solution behavior. Of particular importance, current microsolvation experiments on hydroxide clusters[195] miss the subtle but essential feature of the OH^- HB donation propensity. Therefore, they miss an essential ingredient in the full bulk charge migration mechanism of OH^-(aq). The donated HB is also not captured by quantum chemical calculations or by AIMD simulations of small microsolvated clusters,[211] which, for the same reason, limits their utility in elucidating the condensed phase behavior of OH^-(aq). These shortcomings must, however, be set apart from the current understanding obtained from a host of diffraction and spectroscopic experiments carried out in the condensed phase that provide strong support for dynamical hypercoordination, i.e. the capability of OH^-(aq) to donate a HB by its hydrogen[184,202,205] and accept four HBs by its oxygen[184,196−200] in the bulk, as discussed in section 3.5.

In summary, the findings obtained from one-to-one comparisons of the free energies along the PT coordinate δ of the $H_3O_2^-$ and $H_5O_2^+$ complexes in a vacuum versus OH^-(aq) and H^+(aq) emphasize the dramatic differences that can exist between microsolvated gas phase and fully solvated condensed phase measurements and the potential dangers of deriving properties about one phase from the data collected for the other. In particular, the interplay of fluctuations and polarization effects plays a critical role here.

The next question to be addressed is the extent to which medium-sized clusters, i.e. $OH^-\cdot(H_2O)_n$ with $n \gg 1$, can serve as models for the fully hydrated OH^- anion, OH^-(aq). In small clusters, additional water molecules beyond the first shell are known not to form a HB with the hydroxyl hydrogen but preferentially form HBs with first-shell solvation water molecules.[222,223] Explicit AIMD simulations[211] of IR spectra using an $OH^-\cdot(H_2O)_6$ microsolvation cluster invariably show that a free OH stretch stemming from the hydroxide core contributes to the corresponding peak at approximately 3800 cm^{-1}; this peak would undergo a significant red shift if the hydroxyl hydrogen were involved in hydrogen-bonding. If the hydroxyl hydrogen were involved in hydrogen-bonding for a significant fraction (but not 100%) of the configurations, there could still possibly be a weak shoulder in the infrared spectrum at 3800 cm^{-1}. Given such a situation, the question arises if PT is still possible under conditions of microsolvation. Interestingly, these finite-temperature simulations[211] indeed feature a PT event from step **E** to **F** in Figure 2 of ref 211 that eventually interconverts an initial cluster with four accepted HBs in a roughly square-planar first shell (i.e., the 4 + 2 structure **A**) into another such 4 + 2 structure **H**. Closer inspection of Figure 2 of ref 211 (together with the animation 101205.mpg in the Supporting Information of ref 211 starting from a 4 + 2 structure similar to the one depicted in Figure 1b of ref 211) seems to reveal that PT occurs only after a 3 + 3 structure, **E**, has been formed by fluctuations (*via* intermediate steps **B**, **C**, and finally **D**, which is already a 3 + 3 structure). This means that PT from **E** to **F** occurs when the proton-receiving species (OH^-) accepts only three HBs in a locally tetrahedral arrangement! In this particular system, PT takes place from a first-neighbor water molecule (marked by the blue oxygen atom in **E**) to the OH^- such that the nascent water molecule in structure **F** (now marked by the brown oxygen) is solvated like a water molecule at the water/vapor interface having one dangling (i.e., free or single-donor) OH bond, according to the conceptual discussion in ref 137 (see refs 75 and 76 for quantitative details). This particular HB motif is known to be the preferred majority termination involving intact water molecules at the water/vapor interface.[75,76,137] Furthermore, the nascent OH^- defect in **F** (now marked by the blue oxygen) appears to accept three HBs right after the PT event; that is, it is another 3 + 3 species. Finally, the cluster rearranges, as a consequence of PT and thus OH^- dislocation along the special HB, *via* structure **G** to **H**, where the oxygen site of the newly formed OH^- defect again accepts four HBs in its first shell to restore it to its original state in **A**.[211]

The second animation in the Supporting Information of ref 211 (101435.mpg) starts from a qualitatively different structure in that the OH^- core now accepts only three HBs (and donates none as usual), i.e. a 3 + 3 conformation such as the one shown in Figure 1a of ref 211. Here, PT occurs readily by transferring a proton from a neighboring water molecule to the OH^-, which results in a nascent water molecule with a single dangling OH bond. At its new position, the OH^- again accepts three HBs in a locally tetrahedral coordination pattern in which the hydroxyl OH bond still remains unsolvated (i.e., dangling/free). This implies that the two partner oxygens connected by this particular HB, i.e. the proton-receiving O* and proton-donating $\bar{O}$ sites, are *both* in locally tetrahedral solvation environments with the corresponding OH bonds dangling as they would at the liquid/vapor interface. Thus, given that the OH moieties both "dangle" at the edge of the cluster, both oxygen sites are properly presolvated by accepting only three HBs, and this allows the proton to rattle easily along the connecting HB, as indeed observed several times in the second animation. Since, in this environment, the proton-receiving OH^- finds itself essentially always in a properly presolvated state, accepting only three but never four HBs, the negative charge defect moves forth-and-back at a relatively high PT rate!

The detailed analysis of this system also clarifies the point that PT involving only $n = 6$ water molecules around OH^- can be understood in terms of the presolvation concept after properly taking into account the necessary reduced coordination of all involved species at a "water/vapor interface" in this microsolvated setup. Unlike in bulk solution, the hydroxyl hydrogen sites are *never* observed to be hydrogen-bonded in these AIMD simulations, which implies that the resting state is a bare $OH^-\cdot(H_2O)_4$ complex with four accepted HBs in a roughly square-planar arrangement, whereas the active state is the $OH^-\cdot(H_2O)_3$ state in a roughly tetrahedral arrangement; in both cases, the dangling OH bond must be considered to be the preferred "interfacial-like termination" of the hydroxide anion. This observation can be viewed as the result of a compromise: When an $OH^-\cdot(H_2O)_n$ cluster is small enough that the OH^- defect must necessarily meet the cluster boundary and cannot form a complete bulklike solvation shell, it will preferentially be found with a state in which it accepts three HBs. It is possible, therefore, that, at the interface of a basic solution, OH^- might have a weak attraction to the interface, as

suggested in recent sum-frequency generation measurements.[28] Although fascinating and stimulating within the realms of cluster and interfacial studies, the restricted mechanism seen in AIMD simulations at microsolvation conditions[211] is distinctly different from the bulk situation. In the latter, the existence of a weak HB donated by the hydroxyl hydrogen H′ is now experimentally well established[184,196−200,202,205] and its involvement in charge migration is clearly manifest in AIMD simulations carried out at bulk solvation conditions (see section 5).

In summary, these AIMD simulation studies of somewhat larger microsolvated $OH^-\cdot(H_2O)_n$ complexes additionally support the earlier conclusions drawn from experiments in section 3.5 that one can "...conclude by noting that our observation of a transient hydrogen bond donated by OH^-, in conjunction with the hypercoordinated structures discerned in neutron and X-ray diffraction studies of macroscopic OH^- aqueous solutions[10−12] [*these references correspond to refs 184, 197, and 198 in this review*], suggests a hydroxide solvation behaviour distinctly different from that inferred from spectroscopic studies on gas-phase $OH^-\cdot(H_2O)_n$ clusters where the weak hydrogen-donor bond is unable to form[27] [*this reference corresponds to ref 195 in this review*]. This difference highlights the importance of long-range water-solvent behaviour, and also the need for sophisticated experiments in the bulk liquid phase to help formulate and test detailed descriptions of bulk aqueous solution properties." (quoted from ref 205).

6.3. Counterion and Concentration Effects: Computing IR Spectra for OH^-(aq)

Before we conclude, two final issues pertinent to the study of aqueous solutions, namely the influence of counterions and concentration on PT and structural diffusion, are addressed. All preceding bulk analyses focused on a single isolated defect in the HB network at relatively low concentration, which does not account for the putative role of positive counterions. However, relevant experiments, including IR and Raman spectroscopy,[213] vibrational pump−probe spectroscopy,[193] and neutron diffraction,[196−200] are typically carried out under high concentration conditions and, obviously, include the counterions in one-to-one proportion with OH^-. The availability of such data and the need to understand the influence of counterions and concentration render additional simulation studies necessary. In this vein, studies performed on aqueous basic KOH and NaOH solutions[178−180] will be reviewed (see, e.g., refs 324−328 for similar AIMD simulations where the effects of counterions and concentration on H^+(aq) charge defects were studied).

The computed IR spectra obtained from AIMD simulations[178] of KOH solutions at concentrations of 1.5 and 13 M using classical nuclei (and the deuterium mass for H) are presented in Figure 20; it is noted in passing that these spectra, as well as the general conclusions drawn, are in accord with those obtained using NaOH in other AIMD studies.[179,180] The dilute case corresponds to the KOH to H_2O ratio 1:32, similar both to the standard AIMD simulations of OH^-(aq) (except now the simulation box contains an additional K^+ counterion) and to the lowest concentration, 1:28, studied by neutron diffraction.[200] The high concentration of 13 M corresponds to a KOH to H_2O ratio of about 1:3, which is the highest concentration investigated by neutron diffraction[197,198] and is close to concentrations used for standard (14 M) and time-resolved (13 M) IR spectroscopy.[193,213] The spectrum obtained from the 13 M solution in Figure 20 shows all of the features of the experimental spectrum of 14 M KOH.[213] Although the spectra cannot be superimposed and the frequencies cannot be directly compared because the calculations use deuterium while the experiments do not, the overall shape of the computed spectrum is in good agreement with the experiment, as demonstrated in ref 178 (see the insets of Figures 3 and 4). It is instructive to compare the IR spectra from Figure 20 with Figure 4a of ref 178, which shows the power spectrum at 1.5 and 13 M concentrations obtained from the Fourier transform of the velocity autocorrelation function, together with the reported Raman spectra.[213] The power spectrum contains a combination of IR and Raman intensities and, therefore, cannot be directly compared to an actual Raman spectrum. However, given that the IR intensity at 2400 cm^{-1} is suppressed, the power spectrum should be dominated by the Raman contribution. Thus, the sharp peak in the power spectrum at 2400 cm^{-1} is a suggestive feature that merits special attention.

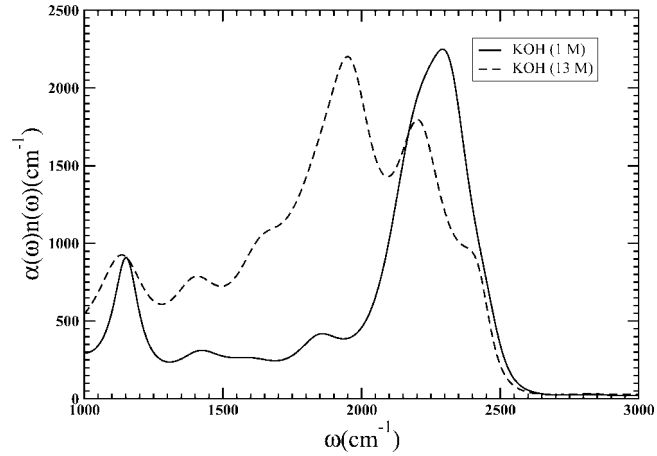

Figure 20. Computed infrared spectra of OH^-(aq) with counterions in aqueous KOH solutions at concentrations of 1.5 M (solid line) and 13 M (dashed line) for the frequency range 1000−3000 cm^{-1}; note that the deuterium mass is used for H. Reprinted with permission from ref 178. Copyright 2006 American Chemical Society.

In order to understand the IR and power spectra and the differences between them, we focus on the three main features of the IR spectrum of the 13 M solution, namely, the shoulder at 2400 cm^{-1} and the two peaks at 2190 and 1950 cm^{-1}. The shoulder can be assigned unambiguously to the O*H′ stretching mode of the (fully deuterated) hydrated hydroxide in solution. The peak at 1950 cm^{-1} can be shown to correspond to the vibrations of OH bonds donated directly to O*, while the peak at 2190 cm^{-1} corresponds to the remaining OH vibrations. The high-frequency shoulder in the IR spectrum of the 13 M solution appears as a sharp peak in the Raman spectrum, a fact that was suggested to support the traditional mirror image picture. Here, we argue in favor of another interpretation that is consistent with the dynamical hypercoordination structural diffusion mechanism of OH^-(aq) described in section 3.3. The fact that the hydroxide ion can donate a weak hydrogen bond (see Figures 4b, 6a, and 8a) for a significant fraction of the total time, according to dynamical hypercoordination in Figure 13b, indicates that, during these intervals, the O*H′ stretching mode experiences a red shift, thereby weakening the contribution of the O*H′ stretch mode (see Figures 4a, 6b, and 8b) in the IR spectrum, which is quasi-free for only

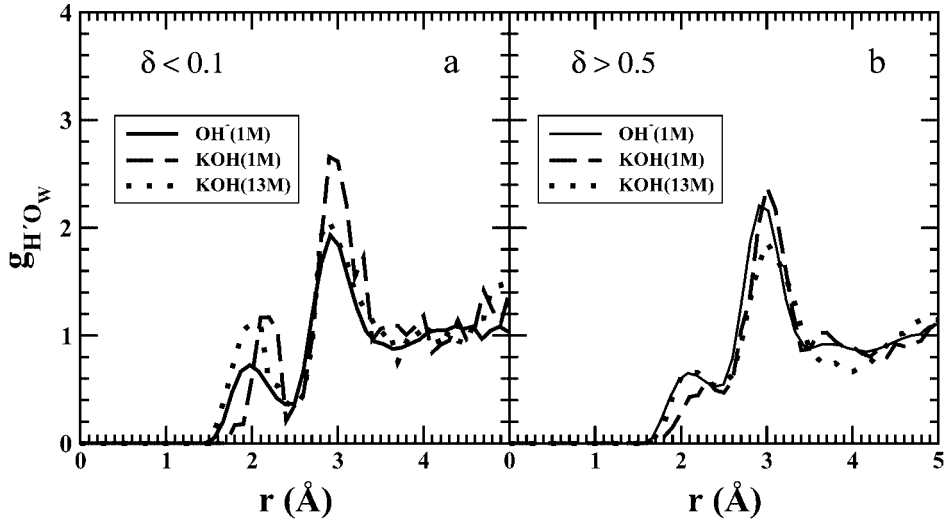

Figure 21. Radial distribution functions, $g(r)$, of OH^-(aq) of $H'O_w$ for $|\delta| \leq 0.1$ Å (a, left) and $|\delta| \geq 0.5$ Å (b, right) without counterions for a single OH^- anion in water obtained from the dynamical hypercoordination mechanism (solid), with counterions for a 1.5 M KOH solution (dashed) as well as for a 13 M KOH solution (dotted); see the caption of Figure 2a and section 5.1 for definitions and labeling conventions. Based on data from refs 16 and 178.

a small fraction of the total time. Consequently, a "full" IR peak at 2400 cm^{-1} is not expected. However, as long as O*H′ is a quasi-free stretch for some fraction of the time, it will appear as a strong signal in the Raman spectrum, in contrast to what is observed in the IR spectrum. This interpretation is consistent with the wealth of more recent experiments[184,196−200,202,205] that support dynamical hypercoordination of OH^-(aq) in general and the capability of O*H′ to donate a HB by its H′ hydrogen in particular (see section 3.5).

In Figure 21, the $H'O_w$ radial distribution functions are shown for the active and resting states (using the usual two δ windows, i.e. $|\delta| \leq 0.1$ Å and $|\delta| \geq 0.5$ Å, respectively) for the high and low concentration KOH solutions as well as for the standard OH^-(aq) simulation of dynamical hypercoordination without any counterion (cf. Figures 6 and 8). This analysis shows that, independent of concentration and counterion, the $H'O_w$ peak around 2 Å is less prominent when the hydroxide ion is in the hypercoordinated, resting state in panel b, thus accepting four HBs by its oxygen. This peak is clearly more prominent in the active state when OH^-(aq) accepts only three HBs in panel a. Counterions even seem to enhance the peak in the small δ-regime somewhat. Interestingly, it has been stressed in the more recent neutron diffraction studies[197,198,200] using LiOH, NaOH, and KOH solutions that the *donated* HB by H′ does not depend strongly on concentration (see section 3.5), in agreement with the AIMD simulations.[178] In contrast, the number of HBs *accepted* by O* is found to depend significantly on concentration in these experiments *and* in AIMD simulations.[178] The latter issue is examined here in more detail using the O*X (X = O and H) radial distribution functions and their running coordination numbers for the two δ-windows at both KOH concentrations compared to the standard OH^-(aq) simulation of dynamical hypercoordination, in which no counterion is present (see Figure 22). These radial distribution functions and coordination numbers show a suppression of the hypercoordinated complex corresponding to the majority, resting state in the 13 M solution. In particular, for $|\delta| \geq 0.5$ Å, the average coordination number drops to 4.6, whereas it is roughly 5.0 in the 1.5 M solution. This AIMD prediction is in accord with subsequent experimental findings of a systematically decreasing number of accepted HBs with increasing concentration of aqueous alkali solutions using neutron diffraction techniques,[197,198,200] as discussed in detail earlier in section 3.5. As in the experiment,[198] the AIMD simulations[178−180] predict no significant change of the hydroxide solvation shell when a different counterion (Na^+ instead of K^+) is employed. A similar finding was reported in passing in a study[69] devoted to solvated electron production in water by reaction of neutral hydrogen with hydroxide. In ref 69, one OH^- charge defect and one $H^•$, i.e. a solvated neutral hydrogen atom,[66] were hosted simultaneously in a periodic supercell containing 32 water molecules (one simulation was performed with 64 water molecules), which has the same concentration as one OH^- and one K^+ in a box of 32 waters.[178] In particular, it was concluded in ref 69 that "The introduction of the $H^•$ atom in the close vicinity of the hydroxide anion does not alter the picture of the isolated hydroxide anion as depicted by Tuckerman et al.[41] " (quoted from ref 69; note that ref 41 therein is ref 135 in this manuscript).

The free energy profiles in Figure 23 at 1.5 and 13 M KOH show that, despite this reduction in the population of complexes accepting four HBs, corresponding to the resting state in the dynamical hypercoordination mechanism, PT is, nevertheless, less probable at high concentration, since the barrier of about 1.3 kcal/mol at 1.5 M is found to increase to approximately 1.8 kcal/mol at 13 M concentration. Examination of the contributing configurations reveals that this increase in the barrier at 13 M arises from structural *distortions* of complexes that accept three HBs, which are the active states in dynamical hypercoordination. As this distortion is found to hinder PT, an inevitable increase in the PT barrier is the result (see ref 178 for more details).

Still, there is an additional twist when comparing the solvation and charge migration at 13 M to the lower concentration case. As Figure 24 shows, at 13 M, the solvation structure of *ordinary* water molecules themselves is significantly distorted compared to the case at 1.5 M. Again, this is in qualitative agreement with experimental findings[197,198] based on water−water radial distribution functions of NaOH solutions which show a distortion of the HB network and an eventual collapse of the second

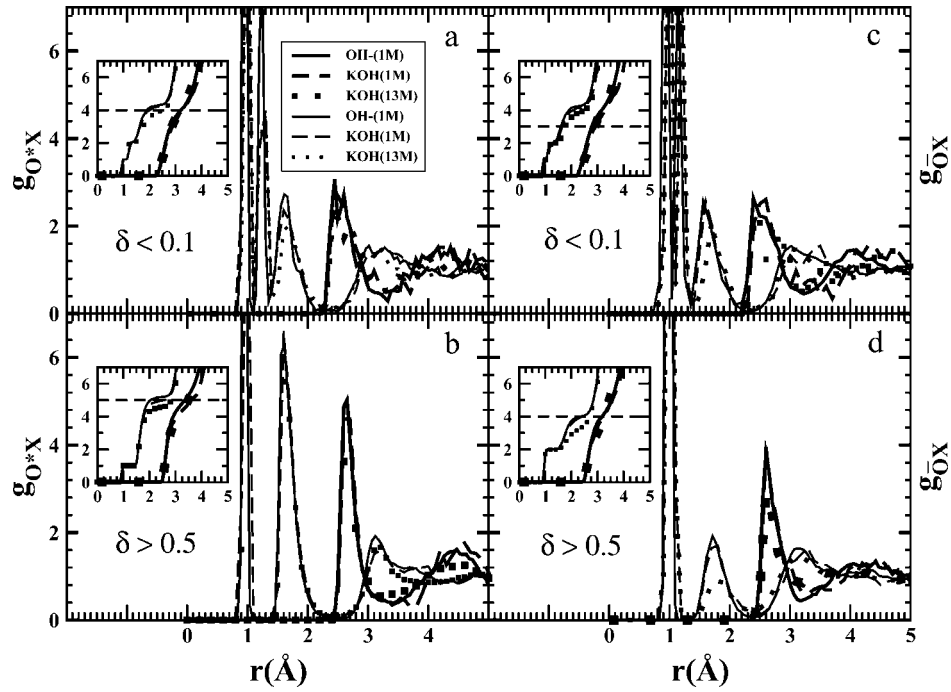

Figure 22. Radial distribution functions, $g(r)$, of OH^-(aq) with respect to O* (left panels) and $\bar{O}$ (right panels) for $|\delta| \leq 0.1$ Å and for $|\delta| \geq 0.5$ Å in the top and bottom panels, respectively, without counterions for a single OH^- anion in water obtained from the dynamical hypercoordination mechanism (solid), with counterions for a 1.5 M KOH solution (dashed) as well as for a 13 M KOH solution (dotted); see the caption of Figure 2a and section 5.1 for definitions and labeling conventions. Here, O* is the *proton-receiving* oxygen, and $\bar{O}$ is the *proton-donating* oxygen. The insets show the corresponding running coordination numbers, $n(r)$, where the dashed horizontal lines mark the preferred coordination numbers. Based on data from refs 16 and 178.

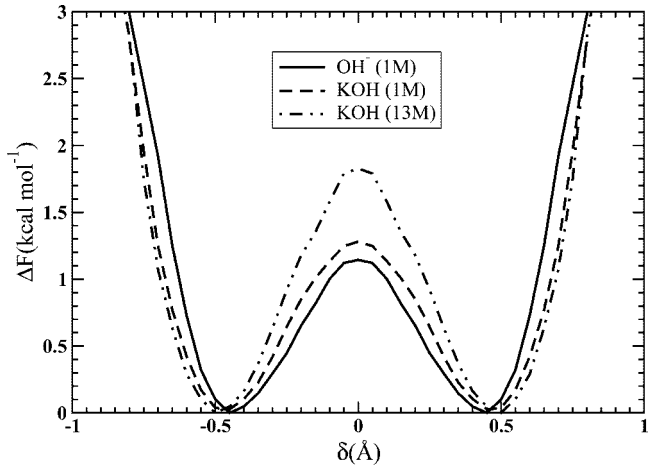

Figure 23. Canonical (Helmholtz) free energy profile of OH^-(aq) at 300 K along the proton transfer coordinate δ without counterions for a single OH^- anion in water obtained from the dynamical hypercoordination mechanism (solid), with counterions for a 1.5 M KOH solution (dashed) as well as for a 13 M KOH solution (dot-dashed). Note that the thermal energy is $k_BT \approx 0.6$ kcal/mol at 300 K. Based on data from refs 16 and 178.

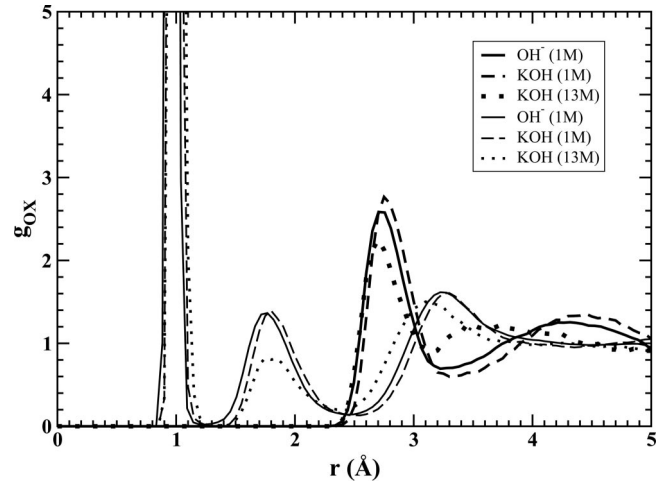

Figure 24. Radial distribution functions, $g(r)$, of OH^-(aq) with reference to all oxygen atoms without counterions for a single OH^- anion in water obtained from the dynamical hypercoordination mechanism (solid), with counterions for a 1.5 M KOH solution (dashed) as well as for a 13 M KOH solution (dot-dashed), where thick and thin lines refer to X = O and X = H partner atoms, respectively. Based on data from refs 16 and 178.

neighboring shell as a function of increasing concentration (similar to the effect observed when compressing pure water). As was shown in ref 178, this distortion gives rise to a reduction in the average water coordination number: there are simply not enough water molecules present in the 1:3 solution to fully solvate all ions.[197] The implication of this phenomenon for charge migration in OH^-(aq) solutions at high concentration is that before a first solvation shell water can transfer one of its protons to the hydroxide ion, its own coordination shell must also adjust so as to be similar to that of the hydroxide ion. This *additional* presolvation step in the dynamical hypercoordination mechanism at high concentration, combined possibly with the suppression of PT events due to a non-negligible structural distortion of the active state complexes (which increases the PT free energy barrier), is presumably partially responsible for the decrease of molar conductivity at 13 M.

Despite the observed effects on structure and free energies in the high concentration limit, the above discussion makes it clear that dynamical hypercoordination, and thus the

resulting structural diffusion mechanism of OH^-(aq), remains essentially the same at high and low concentrations.[178] In particular, it should be pointed out that, even at high concentration, the mechanism based on a coordination number reduction of the hydroxide through loss of a first solvation shell member is still operative, as is confirmed by the coordination numbers in Figure 22, even though it is less efficient for the reasons given above. This conclusion, based on AIMD studies,[178−180] is consistent with experimental findings extracted from a systematic series of studies of concentration and counterion effects on the solvation shell structure of OH^-(aq) using neutron diffraction.[196−200] In view of the general consistency between the AIMD simulations and the neutron diffraction measurements, it is particularly significant that, although the dynamical hypercoordination mechanism obtained from these AIMD simulations is qualitatively different from the traditional mirror image picture, the experimental IR spectrum can, nevertheless, be reproduced in these calculations as well (see Figure 3 of ref 178).

Having elucidated the influence of high concentration (here 13 M) on charge migration in aqueous bulk solutions according to the dynamical hypercoordination mechanism, we ask finally how reliable it is to neglect the counterions at low concentration, 1.5 M, which is one of the assumptions underlying the "standard approach" (see section 4.6). (Note that neglecting the counterions at high concentration would be futile, as they play a crucial role, arising from strong cation solvation effects, in structuring the solution.) To probe this assumption, the 1.5 M KOH data, obtained with one OH^- and one K^+ in the simulation cell, were compared to the standard simulation setup. It should be clear from the total oxygen−oxygen and oxygen−hydrogen radial distribution functions shown in Figure 24, as well as from the radial distributions involving only the hydroxide defect presented in Figures 21 and 22, that the structures of the hydroxide solvation shell and, most importantly, the coordination numbers at 1.5 M KOH, are very similar to those obtained without the counterion. Beyond structural analyses, the free energy profiles of the two cases depicted in Figure 23 are also found to be similar. The PT barrier obtained in the standard simulations is about 1.1−1.2 kcal/mol (see also the classical free energy profile in the upper left panel of Figure 18), which is close to the value of about 1.3 kcal/mol obtained for the 1.5 M KOH solution. All this supports the basic assumption that, at relatively low concentrations of about 1:30 and at even lower concentrations of about 1:60 (which has been shown to lead to the same dynamical hypercoordination picture as the 1:30 case in section 4.6), the effect of the counterion is negligible in that it does not qualitatively alter the OH^-(aq) solvation and migration picture. Again, the negligible influence of the K^+ counterion complies with the observations in ref 69 showing that a hydrated $H^\bullet$ atom[66] does not strongly affect the solvation behavior of an isolated OH^-(aq) at concentrations of 1:32.

7. Charge Migration in Aqueous Basic Solutions: Status Quo et Quo Vadis

The solvation shell structure of hydroxide, as well as its charge migration mechanism and the observed anomalously high conductivity of aqueous basic solutions, have been believed to be closely related to what is known about excess protons in water for roughly a century. The basis for this assumption originates, most likely, with Danneel[155] in his three-page note "Notiz über Ionengeschwindigkeiten" from 1905 (see section 3.1 for more background information) and has been refined by Hückel, Bernal and Fowler, Wannier, and many others up to the present.[4,81−83,144,155−158,160,162−164,166,167] The essential concept introduced by Hückel is to view H_3O^+ as a water molecule with an excess proton, "$H_3O^+ = H_2O + H^+$", while OH^- is regarded as H_2O with a proton missing, symbolically "$OH^- = H_2O - H^+$", i.e. a water molecule with a "proton hole". By assuming analogous solvation shell topologies in aqueous solution, it was thought that the structural diffusion mechanism of OH^-(aq) could be straightforwardly derived from that of H^+(aq) by reversing hydrogen bond polarities and the direction of proton transfer. This notion is most clearly illustrated in Figure 3, which is reproduced from ref 163, in which these ideas are reviewed. Thus, according to this so-called "mirror image" or "proton hole hopping" mechanism (presented in section 3.2), OH^- *accepts three* HBs by its oxygen site and *donates none*. Structural diffusion is driven by the same type of fluctuations in its *second* solvation shell that drive H^+(aq) migration (as summarized in section 2). In this vein, an intermediate $H_3O_2^-$ complex, i.e. schematically $[HO\cdots H\cdots OH]^-$, is formed, which can be regarded as the proton hole analogue of the $H_5O_2^+$ "Zundel complex", i.e. $[H_2O\cdots H\cdots OH_2]^+$, of the H^+(aq) case.

A vastly different solvation and migration scenario, which we term the "dynamical hypercoordination" mechanism (discussed in section 3.3), has been revealed for OH^-(aq) based on a series of *ab initio* molecular dynamics studies in the last 15 years (using the methods presented in section 4). One of the key predictions to have emerged from these studies is that the hydroxide anion in water preferentially *accepts four* hydrogen bonds at its oxygen site in a roughly square-planar arrangement, as shown by the representative snapshot in Figure 4a. This "hypercoordinated" solvation state[135] is, however, unable to accept another proton from a neighboring water molecule; that is, it is the resting and thus the majority state that is essentially inert to proton transfer. Even in this resting state, there is a small propensity to find an additional, fifth water molecule in the neighborhood of the hydroxyl hydrogen site, as seen in the upper right corner of Figure 4a. The resting state can be activated dynamically by fluctuations in the *first* solvation shell of the OH^- that reduce the number of accepted waters from four to three and establish an additional *donated* hydrogen bond from the hydroxyl hydrogen to a water molecule in its vicinity. This transient minority state depicted in Figure 4b adopts a locally tetrahedral structure in its first solvation shell similar that of a typical intact water molecule in the bulk but different in that it accepts three HBs and donates one. In such a short-lived configuration, a proton can be transferred readily along one of the three accepted hydrogen bonds, which converts this particular OH^- defect into a regular water molecule that accepts two and donates two hydrogen bonds. Note that the weak hydrogen bond donated by the hydroxyl hydrogen in the square-planar majority state is now transmuted into a regular hydrogen bond. The net effect of this proton transfer is a translocation of the negative charge defect to the hydrogen-bonded water molecule that donated the proton according to the sequence of events presented in the snapshots of panels (e) → (h) of Figure 12 extracted directly from *ab initio* path integral simulations. Neither quantum

effects on nuclear motion nor concentration/counterion effects alter the key characteristics of this mechanism (see section 6).

Evidently, the traditional mirror image mechanism and the novel dynamical hypercoordination mechanism are mutually exclusive so that the question must be answered as to which one of the two is in closer accord with experiment. This comparison is based on detailed analyses of the different solvation shell structures in section 5.2, diffusion coefficients in section 5.3, charge migration in section 5.4, dynamics and kinetics in section 5.5, and rotational relaxation in section 5.6. A key difference between the two advocated mechanisms is the underlying preferred solvation shell structure of the OH^-(aq) defect, which can be compared directly to experimental findings. Fortunately, there is now a wealth of recent diffraction and spectroscopic experiments on hydroxide anions in bulk aqueous environments (see section 3.5), including LiOH, NaOH, and KOH basic solutions of varying concentration, that probe the solvation structure of OH^-(aq). The experimental findings in bulk solvation environments strongly support the existence of hypercoordination of the oxygen, its preferentially acceptance of four hydrogen bonds, the ability of OH^-(aq) to donate a fifth (weak) hydrogen bond *via* its hydrogen site, and the fact that the $H_3O_2^-$ is a short-lived transient complex rather than a stable intermediate. This, in turn, substantiates the ability of the novel dynamical hypercoordination mechanism to describe structural diffusion and charge migration in aqueous basic solutions.

This overall consistent picture developed here has important and far-reaching ramifications. Most importantly, a fundamental asymmetry exists in the solvation pattern of OH^-(aq) compared to H^+(aq), which leads not only to strongly different structural diffusion mechanisms of the hydrated hydroxide versus the hydrated proton but also to different behavior in more general terms. For example, the dynamical hypercoordination picture of OH^-(aq) diffusion can be expected to influence how we understand phenomena such as the conductivity of negative versus positive charge defects along hydrated membranes and water wires and the properties of charge defects in hydrogen-bonded networks embedded in restricted geometries and under confinement. In addition, the different solvation shell properties of OH^-(aq) versus H^+(aq) will impact our understanding of the equilibrium charge state, basic or acidic, of finite aqueous droplets and extended surfaces, as well as interfaces involving water.[17−31] In particular, experimental support has been given to the idea that OH^- is the most surface-excluded hydrated anion in the series OH^-, Cl^-, Br^-, NO_3^-, and I^- whereas the hydrated proton H^+ is the most strongly surface-accumulated.[20] Settling the question of the basicity or acidity of aqueous interfaces will, in turn, influence our understanding of atomospheric chemical processes, including aerosol reactions, gas uptake, and nanocatalysis.[20,27] The novel solvation patterns uncovered in the *ab initio* molecular dynamics simulation might also have an impact on our understanding of the role of OH^-(aq) in the Hofmeister series[17,20,27,70,71] and the properties of negative versus positive charge defects in nonaqueous associated liquids, including their mixtures with water, charge transport in biomolecular systems,[5−8,61−64] and fuel-cell technologies based on alkaline-anion exchange membranes.[36−40] Recently, the hypercoordinated state has been proposed for trapping of OH^- impurities in ice and, thereby, to account for the relatively low proton activity observed in isotopic substitution experiments in hydroxide-rich ices.[60] Given the general importance of charge migration in basic and acidic aqueous environments, we believe it is timely to discuss the fundamental asymmetry revealed in the solvation pattern of OH^-(aq) versus H^+(aq) and the dynamical hypercoordination mechanism by extending or updating modern textbooks on Physical Chemistry.

In the course of the studies we have performed, we have demonstrated that what we have termed the "presolvation concept" (explained in section 2) provides an astonishingly simple but useful viewpoint for understanding, in general terms, charge defect migration in hydrogen-bonded systems starting from an assumed preferential solvation pattern of the pertinent defect. The presolvation concept not only rationalizes charge migration in acidic bulk solutions (see section 2) but is also able to predict consistent structural diffusion mechanisms of OH^-(aq) depending on the solvation shell properties, as demonstrated for three vastly different scenarios (see section 3). Presolvation is seen not only to predict the mechanism that is consistent with experiment, based on the proper solvation shell structure, but it also offers a microscopic rationalization of the failure of other proposed mechanisms. Moreover, it can be successfully generalized to cope with interfaces (see section 6.2). Overall, although the solvation, diffusion, and kinetics of OH^-(aq) are quite different from those of H^+(aq), despite superficial similarities and suggestive symmetries, the presolvation concept provides a unifying perspective on both basic and acidic solutions. Moreover, the presolvation concept provides a consistent and unified means by which charge defect transport mechanisms can be understood in numerous other types of hydrogen-bonded systems.[45,46,57] An example is charge transfer along a hydrogen-bonded water wire,[62] which requires accounting for the reduced solvation number of the preferred state due to geometric confinement and possibly different solvating acceptor and/or donor groups.

When comparing solvation of OH^- versus H^+ in bulk liquid water, another important observation is that aspects of the hydration shell of the latter can essentially be reproduced using fairly small $H^+ \cdot (H_2O)_n$ clusters by varying their size. In particular, the crucial limiting complexes of H^+(aq), i.e. the Zundel $[H_2O \cdots H \cdots OH_2]^+$ and Eigen $H_3O^+ \cdot (H_2O)_3$ motifs, can be mimicked using finite $n = 2$ and $n = 4$ clusters, respectively. This is distinctly different for OH^-(aq), where the hydrogen bond donated by the hydroxyl hydrogen is not present in finite $OH^- \cdot (H_2O)_n$ clusters in a similar size regime (see section 6.2). Nevertheless, an interesting charge translocation mechanism is found at microsolvation conditions with $n = 6$ in simulations.[211] This restricted mechanism seems to share the feature of the dynamical hypercoordination scenario that PT preferentially occurs once a roughly square-planar coordination of the oxygen site involving four accepted hydrogen bonds is reduced to three in an approximately tetrahedral arrangement; however, it lacks the stabilizing influence of the donated hydrogen bond involving the hydroxyl hydrogen. This should serve as a reminder that microsolvation studies in the gas phase, both in the virtual lab and in the real one, might lead to qualitatively different conclusions from solvation studies carried out in condensed phase environments. Thus, an interesting yet challenging idea for studying dynamical hypercoordination, which is key to understanding basic solutions in general and OH^-(aq) in particular, might be to

grow clusters sufficiently large to involve the donated hydrogen bond. This approach could be attempted both theoretically and experimentally. Furthermore, the interplay of quantum effects and thermal fluctuations with polarization due to bulk solvation can lead to surprising phenomena for the smallest possible hydroxide and hydronium microsolvated complexes (see section 6.2).

Hypercoordination of the hydroxide anion also has an impact on the way basic solutions should be modeled in the future in the framework of force field based molecular dynamics. This is particularly important in view of the demonstrated failure of molecular dynamics based on standard OH^-/water nonpolarizable force fields to explain recent diffraction data on $OH^-(aq)$ solvation.[184] Fortunately, there are promising advances to design improved classical force field models[177] for the hydroxide anion. One route is to optimize the force field using accurate interaction energies of an OH^- that accepts four water molecules at its oxygen (i.e., much like the hypercoordinated state shown in Figure 4a) with polarizability added at the oxygen site.[185] Four such models have been constructed and shown to yield semiquantitative agreement with X-ray data,[185] which is a major improvement over the nonpolarizable force field employed earlier.[184] Another promising route is to parametrize a multistate empirical valence bond model[14] to describe basic aqueous solutions.[30] Alternatively, improvement can be obtained by taking into account explicitly the hypercoordinated solvation shell of $OH^-(aq)$ in terms of a ringlike structure[183] that can accept three or four hydrogen bonds at the oxygen site. In particular, a massless, charged ring, rather than the usual point charges, is used in the "charged ring" (CR) model[183] to represent the negative unit charge in order to mimic the ringlike electron localization function isosurfaces reported in refs 135 and 215 (see Figure 4). Based on this model, work is in progress to generalize this idea to parametrizing an empirical valence bond model[329] for fitting. Apparently, such a combined model has been used most recently to aid in the interpretation of time-resolved vibrational spectroscopy.[206] Unfortunately, however, no details of this model and its performance were presented in the main article or in the Supporting Information in ref 206 that would allow an objective assessment of its quality. Clearly, in addition to hypercoordination at the oxygen site, any accurate empirical model also needs to capture the ability of $OH^-(aq)$ to transiently donate a weak hydrogen bond involving its hydroxyl hydrogen.

The rich conclusions and predictions extracted here from elaborate *ab initio* computer simulations, which are supported by a wealth of recent *time-averaging* diffraction and spectroscopic experiments, should be a challenge to future *time-resolved* experiments on $OH^-(aq)$, such as those in ref 206. In view of these findings, it seems most promising to carry out such experiments directly in the condensed phase in order to probe the ultrafast hydrogen bond dynamics in the bulk environment. This would yield direct access to the kinetics induced by the migration of $OH^-(aq)$ charge defects, where the detailed predictions collected in section 5.5 could serve as useful guidelines. Recent impressive advances[330−333] in this direction are encouraging.[334−343] In addition to the spectacular successes for the $H^+(aq)$ case,[91,92,95,98,100,101] this route will certainly open up novel experimental avenues for research into proton transfer reaction *dynamics* and charge defect migration *kinetics* in many different classes of associated liquids.

8. Acknowledgments

We thank Marcel Baer for helping us prepare the figures and Rachel Glaves for a careful reading of the manuscript. Partial financial support is gratefully acknowledged as follows. D.M.: Ruhr-Universität Bochum (RUB), Deutsche Forschungsgemeinschaft (DFG), and Fonds der Chemischen Industrie (FCI). A.C.: Department of Science and Technology (DST), Department of Atomic Energy (DAE), and Council of Scientific and Industrial Research (CSIR), all Government of India, and Alexander von Humboldt Foundation (AvH) for a Fellowship that allowed stays as a Visiting Professor in Bochum. M.E.T.: NSF CHE-0310107, NET CHE-0704036, Camille and Henry Dreyfus Foundation, Inc. (TC-02-012), and Alexander von Humboldt (AvH) Foundation for the Bessel Award 2005 that allowed stays as a Visiting Professor in Bochum. The calculations were performed at Bovilab@RUB (Bochum) and Rechnerverbund-NRW as well as on Linux Clusters granted to A.C. by DST, DAE, CSIR, and the AvH Foundation.

9. Note Added in Proof

Publications that appeared in the ISI Web of Science after submission of the manuscript are added in proof:

Several papers, including two Comments and a Reply addressing interfacial properties of the hydroxide ion, are collected as a "Frontiers Discussion".[344−348] They refer to the issue of interfacial solvation and the charge state of surfaces of basic aqueous solutions addressed in the general introduction and concluding sections and refs 17−31 cited therein; in particular, the Comment/Reply discussion is related to ref 31 of this review. Moreover, a publication discussing a polarizable empirical force-field study of the reorientational behavior[349] has been included in this string of papers on the solvation properties of hydroxide ion, which refers to the discussion presented in section 5.6 herein. It should be noted, however, that this empirical model does not allow for proton transfer events. Specific hydroxide ion binding at the oil/water interface has been investigated in ref 350, structure and charging of hydrophobic material/water interfaces have been studied in ref 351 with a focus on interfacial hydroxyl and hydronium ions, and ref 352 discusses various aspects of experimental and computational approaches and conclusions derived from these approaches concerning the sign of the excess charge at water surfaces.

Computational details and a quality assessment of the multistate empirical valence bond model extending the "charged-ring" model[183] used in ref 206 to explain femtosecond pump−probe and 2D infrared experiments are now available in ref 353, which replaces the private communication in ref 329.

Following ref 60, the role of hydroxide ions in the diffusion of topological charge defects in ice was studied in ref 354, and the effect of hydroxide ions on proton transfer and H/D isotopic exchange of water molecules was examined at the surface of amorphous ice films in ref 355. Adiabatic and vertical ionization energies of the aqueous hydroxide anion, the vertical attachment energy of an electron to the aqueous hydroxyl radical, and the corresponding adiabatic electron affinity have been determined in ref 356. Binding energies of deprotonated, protonated, and neutral water clusters have been evaluated using a variety of electronic structure methods,[357] which refer to the discussion in section

3.5 on the accuracy[224,225] of computed relative stabilities of microsolvated OH^- clusters.

Finally, drawing on the population correlation function formalism introduced in ref 134 as a tool to quantify charge migration in hydrogen-bonded systems (see section 5.5), investigations of the kinetics of positive charge defects appeared in the most recent literature.[358,359]

10. References

(1) Atkins, P.; de Paula, J. *Atkins' Physical Chemistry*, 8th ed; Oxford University Press: 2006; see Chapter 21.7(a), p 766. The modern view of the Grotthuss mechanism for H^+(aq) structural diffusion driven by hydrogen bond breaking in the second solvation shell has already been introduced in the 6th edition: Atkins, P. W. *Physical Chemistry*, 6th ed.; Oxford University Press: 1998; see Chapter 24.8, p 740 (whereas the molecular rotation mechanism was described in the 5th edition: Atkins, P. W. Physical Chemistry, 5th ed.; Oxford University Press: 1994. see Chapter 24.8, p 840).

(2) Note: "hydroxyl (anion)" and "oxonium" (or "hydroxonium") are sometimes used as synonyms for OH^- and H_3O^+, respectively, whereas "oxidanide" for OH^- and "oxidanium" for H_3O^+ are recommended as substitutes by IUPAC (see IUPAC Provisional Recommendation Drafts 2004).

(3) Onsager, L. *Science* **1969**, *166*, 1359; see in particular p 1364.

(4) Eigen, M. *Angew. Chem., Int. Ed.* **1964**, *3*, 1; for the mirror image concept, see in particular p 3: "Similar structural relationships exist for the defect proton[8]; here, the hydroxide ion HO^- corresponds to the hydronium ion, and the (probably less stable) structural species $H_7O_4^-$ to the secondary hydrate complex $H_9O_4^+$." Angew. Chem. 1963, *75*, 489.

(5) Roux, B. *Acc. Chem. Res.* **2002**, *35*, 366.

(6) Decoursey, T. E. *Physiol. Rev.* **2003**, *83*, 475. Corrections: Physiol. Rev. 2003, *83*, 1067; Physiol. Rev. 2004, *84*, 1479.

(7) Wraight, C. A. *Biochim. Biophys. Acta—Bioenergetics* **2006**, *1757*, 886.

(8) Mulkidjanian, A. Y.; Heberle, J.; Cherepanov, D. A. *Biochim. Biophys. Acta—Bioenergetics* **2006**, *1757*, 913.

(9) Kreuer, K.-D. *Chem. Mater.* **1996**, *8*, 610.

(10) Kreuer, K.-D.; Paddison, S. J.; Spohr, E.; Schuster, M. *Chem. Rev.* **2004**, *104*, 4637.

(11) Several Books and Special Issues are devoted to this subject, such as: Hynes, J. T., Klinman, J. P., Limbach, H.-H., Schowen, R. L., Eds.; *Hydrogen-Transfer Reactions*; Wiley-VCH: Weinheim, 2006. Limbach, H.-H. *Magn. Reson. Chem.* **2001**, *39*, S1. Agmon, N.; Gutman, M. *Isr. J. Chem.* **1999**, *39* (3−4), 213. Limbach, H.-H.; Manz, J. *Ber. Bunsen-Ges. Phys. Chem.* **1998**, *102* (3), 289.

(12) (a) de Grotthuss, C. J. T. *Ann. Chim. (Paris)* **1806**, *LVIII*, 54. (b) English translation (note the three misprints in the name) de Grotthius, C. l. T. *Philos. Mag. (London)* **1806**, *25*, 330. (c) Original pamphlet (unpublished, 22 pages plus front page and one page with Figures I and II, no pagination): MÉMOIRE SUR LA DÉCOMPOSITION DE L'EAU et des corps qu'elle tient en dissolution a l'aide de L'ÉLECTRICITÉ GALVANIQUE par C. J. T. de Grotthuss (Rome, 1805).

(13) Marx, D. *ChemPhysChem* **2006**, *7*, 1848 Addendum. ChemPhysChem 2006, *8*, 209.

(14) Voth, G. A. *Acc. Chem. Res.* **2006**, *39*, 143.

(15) Ludwig, R. *Angew. Chem., Int. Ed.* **2003**, *42*, 258. Angew. Chem. 2003, *115*, 268.

(16) Tuckerman, M. E.; Chandra, A.; Marx, D. *Acc. Chem. Res.* **2006**, *39*, 151.

(17) Collins, K. D.; Washabaugh, M. W. *Q. Rev. Biophys.* **1985**, *18*, 323.

(18) Mucha, M.; Frigato, T.; Levering, L. M.; Allen, H. C.; Tobias, D. J.; Dang, L. X.; Jungwirth, P. *J. Phys. Chem. B* **2005**, *109*, 7617.

(19) Tarbuck, T. L.; Ota, S. T.; Richmond, G. L. *J. Am. Chem. Soc.* **2006**, *128*, 14519.

(20) Pegram, L. M.; Record, M. T., Jr. *Proc. Natl. Acad. Sci. U. S. A.* **2006**, *103*, 14278.

(21) Buch, V.; Milet, A.; Vácha, R.; Jungwirth, P.; Devlin, J. P. *Proc. Natl. Acad. Sci. U.S.A.* **2007**, *104*, 7342.

(22) Kudin, K. N.; Car, R. *J. Am. Chem. Soc.* **2008**, *130*, 3915.

(23) Vácha, R.; Zangi, R.; Engberts, J. B. F. N.; Jungwirth, P. *J. Phys. Chem. C* **2008**, *112*, 7689.

(24) Vácha, R.; Horinek, D.; Berkowitz, M. L.; Jungwirth, P. *Phys. Chem. Chem. Phys.* **2008**, *10*, 4975.

(25) Petersen, P. B.; Saykally, R. J. *Chem. Phys. Lett.* **2008**, *458*, 255.

(26) Jungwirth, P.; Winter, B. *Annu. Rev. Phys. Chem.* **2008**, *59*, 343.

(27) Pegram, L. M., Jr. *Chem. Phys. Lett.* **2008**, *467*, 1.

(28) Tian, C.; Na, J.; Waychunas, G. A.; Shen, Y. R. *J. Am. Chem. Soc.* **2008**, *130*, 13033.

(29) Lee, H. S.; Tuckerman, M. E. *J. Phys. Chem. A* **2009**, *113*, 2144.

(30) Wick, C. D.; Dang, L. X. *J. Phys. Chem. A* **2009**, *113*, 6356.

(31) Winter, B.; Faubel, M.; Vácha, R.; Jungwirth, P. *Chem. Phys. Lett.* **2009**, *474*, 241.

(32) Schuster, M.; Meyer, W. H.; Wegner, G.; Herz, H. G.; Ise, M.; Kreuer, K.-D.; Maier, J. *Solid State Ionics* **2001**, *145*, 85.

(33) Schuster, M. F. H.; Meyer, W. H.; Schuster, M.; Kreuer, K.-D. *Chem. Mater.* **2004**, *16*, 329.

(34) Schuster, M.; Rager, T.; Noda, A.; Kreuer, K.-D.; Maier, J. *Fuel Cells* **2005**, *5*, 355.

(35) Paddison, S. J.; Kreuer, K. E.; Maier, J. *Phys. Chem. Chem. Phys.* **2006**, *8*, 4530.

(36) Slade, R. C. T.; Varcoe, J. R. *Solid State Ionics* **2005**, *176*, 585.

(37) Varcoe, J. R.; Slade, R. C. T. *Fuel Cells* **2005**, *5*, 187.

(38) Varcoe, J. R.; Slade, R. C. T.; Yee, E. L. H. *Chem. Commun.* **2006**, 1428.

(39) Huang, A.; Xia, C.; Xiao, C.; Zhuang, L. *J. Appl. Polym. Sci.* **2006**, *100*, 2248.

(40) Chempath, S.; Einsla, B. R.; Pratt, L. R.; Macomber, C. S.; Boncella, J. M.; Rau, J. A.; Pivovar, B. S. *J. Phys. Chem. C* **2008**, *112*, 3179.

(41) Hyman, H. H.; Quarterman, L. A.; Kilpatrick, M.; Katz, J. J. *J. Phys. Chem.* **1961**, *65*, 123.

(42) Gillespie, R. J.; Moss, K. C. *J. Chem. Soc. A* **1966**, 1170.

(43) Kim, D.; Klein, M. L. *J. Am. Chem. Soc.* **1999**, *121*, 11251.

(44) Raugei, S.; Klein, M. L. *ChemPhysChem* **2004**, *5*, 1569.

(45) Morrone, J. A.; Tuckerman, M. E. *J. Chem. Phys.* **2002**, *117*, 4403.

(46) Morrone, J. A.; Haslinger, K. E.; Tuckerman, M. E. *J. Phys. Chem. B* **2006**, *110*, 3712.

(47) Petersen, M. K.; Voth, G. A. *J. Phys. Chem. B* **2006**, *110*, 7085.

(48) Münch, W.; Kreuer, K.-D.; Silvestri, W.; Maier, J.; Seifert, G. *Solid State Ionics* **2001**, *145*, 437.

(49) Iannuzzi, M.; Parrinello, M. *Phys. Rev. Lett.* **2004**, *93*, 025901.

(50) Iannuzzi, M. *J. Chem. Phys.* **2006**, *124*, 204710.

(51) Haile, S. M.; Boysen, D. A.; Chisholm, C. R. I.; Merle, R. B. *Nature (London)* **2001**, *410*, 910.

(52) Boysen, D. A.; Uda, T.; Chisholm, C. R. I.; Haile, S. M. *Science* **2004**, *303*, 68.

(53) Wood, B. C.; Marzari, N. *Phys. Rev. B* **2007**, *76*, 134301.

(54) Lee, H. S.; Tuckerman, M. E. *J. Phys. Chem. C* **2008**, *112*, 9917.

(55) Wise, H. *J. Phys. Chem.* **1967**, *71*, 2843.

(56) Glasser, L. *Chem. Rev.* **1975**, *75*, 21.

(57) Rosso, L.; Tuckerman, M. E. *Solid State Ionics* **2003**, *161*, 219.

(58) Cascella, M.; Raugei, S.; Carloni, P. *J. Phys. Chem. B* **2004**, *108*, 369.

(59) Blumberger, J.; Ensing, B.; Klein, M. L. *Angew. Chem., Int. Ed.* **2006**, *45*, 2893.

(60) Cwiklik, L.; Buch, V. *Phys. Chem. Chem. Phys.* **2009**, *11*, 1294.

(61) Sagnella, D. E.; Laasonen, K.; Klein, M. L. *Biophys. J.* **1996**, *71*, 1172.

(62) Mei, H. S.; Tuckerman, M. E.; Sagnella, D. E.; Klein, M. L. *J. Phys. Chem. B* **1998**, *102*, 10446.

(63) Jensen, M. Ø.; Röthlisberger, U.; Rovira, C. *Biophys. J.* **2005**, *89*, 1744.

(64) Riccardi, D.; König, P.; Prat-Resina, X.; Yu, H.; Elstner, M.; Frauenheim, T.; Cui, Q. *J. Am. Chem. Soc.* **2006**, *128*, 16302.

(65) Crowell, R. A.; Lian, R.; Shkrob, I. A.; Bartels, D. M.; Chen, X.; Bradforth, S. E. *J. Chem. Phys.* **2004**, *120*, 11712.

(66) Kirchner, B.; Stubbs, J.; Marx, D. *Phys. Rev. Lett.* **2004**, *89*, 215901.

(67) Petersen, C.; Thøgersen, J.; Jensen, S. K.; Keiding, S. R. *J. Phys. Chem. A* **2007**, *111*, 11410.

(68) Thøgersen, J.; Jensen, S. K.; Petersen, C.; Keiding, S. R. *Chem. Phys. Lett.* **2008**, *466*, 1.

(69) Renault, J. P.; Vuilleumier, R.; Pommeret, S. *J. Phys. Chem. A* **2008**, *112*, 7027; the Supporting Information ("Supplementary Material Figure S1: Square displacement of the hydroxide anion along a single trajectory") has been kindly provided by the authors.

(70) Kunz, W.; Henle, J.; Ninham, B. W. *Curr. Opin. Colloid Interface* **2004**, *9*, 19.

(71) Lo Nostro, P.; Ninham, B. W.; Milani, S.; Lo Nostro, A.; Pesavento, G.; Baglioni, P. *Biophys. Chem.* **2006**, *124*, 208.

(72) Devlin, J. P.; Uras, N.; Sadlej, J.; Buch, V. *Nature (London)* **2002**, *417*, 269.

(73) Kang, H. *Acc. Chem. Res.* **2005**, *38*, 893.

(74) Lee, C.-W.; Lee, P.-R.; Kang, H. *Angew. Chem., Int. Ed.* **2006**, *45*, 5529.

(75) Kuo, I. F. W.; Mundy, C. J. *Science* **2004**, *303*, 658.

(76) Mundy, C. J.; Kuo, I. F.-W. *Chem. Rev.* **2006**, *106*, 1282.

(77) Bianco, R.; Hynes, J. T. *Acc. Chem. Res.* **2006**, *39*, 159.

(78) Gutberlet, A.; Schwaab, G.; Birer, Ö.; Masia, M.; Kaczmarek, A.; Forbert, H.; Havenith, M.; Marx, D. *Science* **2009**, *324*, 1545; see also ref 79.

(79) Zwier, T. S. *Science* **2009**, *324*, 1522.

(80) Wicke, E.; Eigen, M.; Ackermann, Th. *Z. Phys. Chem. (N.F. Frankfurt)* **1954**, *1*, 340.
(81) Conway, B. E.; Bockris, J. O'M.; Linton, H. *J. Chem. Phys.* **1956**, *24*, 834; see in particular p 847 ("For a water molecule at OH′, however, there is a proton *deficiency* in the water compared with the normal stoichiometry H:O = 2:1 and the opposition of two OH bonds and their consequent repulsion which occurs just before rotation in the $H_3O^{\bullet}-H_2O$ case does not take place, ...") and the respective scheme.
(82) Ackermann, Th. *Discuss. Faraday Soc.* **1957**, *24*, 180; see in particular Figures 11 and 12.
(83) Eigen, M.; De Maeyer, L. *Proc. R. Soc. (London)* **1958**, *247*, 505; see in particular Figure 60.
(84) Meiboom, S. *J. Chem. Phys.* **1961**, *34*, 375.
(85) Luz, Z.; Meiboom, S. *J. Am. Chem. Soc.* **1964**, *86*, 4768.
(86) Zundel, G.; Metzger, H. *Z. Phys. Chem. (N.F. Frankfurt)* **1968**, *58*, 225.
(87) Halle, B.; Karlström, G. *J. Chem. Soc., Faraday Trans. 2* **1983**, *79*, 1031; note that the kinetic H/D isotope effect for k_- should read 2.8 ± 0.4 in the abstract (B. Halle, private communication). J. Chem. Soc., Faraday Trans. 2 1983, *79*, 1047.
(88) Chang, H.-C.; Wu, C.-C.; Kuo, J.-L. *Int. Rev. Phys. Chem.* **2005**, *24*, 553.
(89) Headrick, J. M.; Diken, E. G.; Walters, R. S.; Hammer, N. I.; Christie, R. A.; Ciu, J.; Myshakin, E. M.; Duncan, M. A.; Johnson, M. A.; Jordan, K. D. *Science* **2005**, *308*, 1765; Correction. Headrick, J. M.; et al. *Science* **2005**, *309*, 1326.
(90) Zundel, G. *Adv. Chem. Phys.* **2000**, *111*, 1.
(91) Bakker, H. J.; Nienhuys, H. K. *Science* **2002**, *297*, 587.
(92) Rini, M.; Magnes, B. Z.; Pines, E.; Nibbering, E. T. J. *Science* **2003**, *301*, 349.
(93) Rini, M.; Pines, D.; Magnes, B. Z.; Pines, E.; Nibbering, E. T. J. *J. Chem. Phys.* **2004**, *121*, 9593.
(94) Botti, A.; Bruni, F.; Imberti, S.; Ricci, M. A.; Soper, A. K. *J. Chem. Phys.* **2004**, *121*, 7840.
(95) Mohammed, O. F.; Pines, D.; Dreyer, J.; Pines, E.; Nibbering, E. T. J. *Science* **2005**, *310*, 83.
(96) Botti, A.; Bruni, F.; Ricci, M. A.; Soper, A. K. *J. Chem. Phys.* **2006**, *125*, 014508.
(97) Woutersen, S.; Bakker, H. J. *Phys. Rev. Lett.* **2006**, *96*, 138305.
(98) Tielrooij, K. J.; Timmer, R. L. A.; Bakker, H. J.; Bonn, M. *Phys. Rev. Lett.* **2009**, *102*, 198303.
(99) Winter, B.; Faubel, M.; Hertel, I. V.; Pettenkofer, C.; Bradforth, S. E.; Jagoda-Cwiklik, B.; Cwiklik, L.; Jungwirth, P. *J. Am. Chem. Soc.* **2006**, *128*, 3864.
(100) Amir, W.; Gallot, G.; Hache, F.; Bratos, S.; Leicknam, J.-C.; Vuilleumier, R. *J. Chem. Phys.* **2007**, *126*, 034511.
(101) Mohammed, O. F.; Pines, D.; Nibbering, E. T. J.; Pines, E. *Angew. Chem., Int. Ed.* **2007**, *46*, 1458.
(102) Tuckerman, M. E.; Laasonen, K.; Sprik, M.; Parrinello, M. *J. Phys.: Condens. Matter* **1994**, *6*, A93.
(103) Tuckerman, M.; Laasonen, K.; Sprik, M.; Parrinello, M. *J. Phys. Chem.* **1995**, *99*, 5749; see also ref 105.
(104) Tuckerman, M.; Laasonen, K.; Sprik, M.; Parrinello, M. *J. Chem. Phys.* **1995**, *103*, 150.
(105) Note: Figure 1 in ref 103 depicts only part of the full structural diffusion scenario found in the underlying *ab initio* simulations; see also refs 102 and 104. As stated in the main text, in approximately 60% of the configurations the excess proton is associated with the oxygen atom of a single water molecule, thus forming an Eigen complex $H_9O_4^+$ as depicted in panel a of Figure 1 in ref 103. This *majority complex* is, however, in dynamical equilibrium with Zundel complexes $H_5O_2^+$ such as those shown in panels b and c, with these being consequently the *minority complexes*. It was also found in ref 103 that the charge defect H^+(aq) fluctuates dynamically between these Eigen and Zundel complexes as a result of ultrafast proton transfer along any one of the three hydrogen bonds donated by the hydronium H_3O^+ ion, it being the core of an Eigen complex. In order for the majority (Eigen) complex to undergo structural diffusion, it must necessarily pass through the minority (Zundel) complex configuration. The particular hydrogen bond along which the proton is transferred to a water molecule in the first shell of this H_3O^+ is selected by forming a so-called "special" (hydrogen) bond due to an undercoordination in the second solvation shell effected by hydrogen bond cleavage.[103] In order to demonstrate this point, panels b and c show two such representative transfer events involving the *same* Eigen complex (a). Thus, these processes must be discussed with reference to the majority complex, i.e. the Eigen complex, shown in panel a. Here, the hydrogen bond donated by the H_3O^+ core that points toward the bottom gets selected due to the undercoordination of the water molecule accepting it (note that there is no hydrogen bond with respect to the water molecule on its left side). Panel b shows the situation 40 fs after panel a, when this particular proton transfer is carried out *half way* along the selected special bond, by highlighting the corresponding Zundel complex. Another choice of a special bond is shown in panel c, about 180 fs later. As stated in the text, it involves the same Eigen complex (a) as the event leading to the Zundel complex (b), but a *different* special bond is selected this time due to appropriate fluctuations in the second solvation shell, which creates a Zundel complex with the hydrogen-bonded water molecule in the upper right corner (note that the formerly disconnected water molecule in the lower left corner now donates a hydrogen bond). Finally, it is stressed that the same mechanism that is only partly captured by three snapshot configurations in Figure 1 of the pioneering work[103] is depicted more coherently in Figure 1 of ref 120 by documentation of a successful charge migration event, i.e. a full displacement of an Eigen complex from panel a to panel c *via* a connecting Zundel complex (b) and including the onset of the next displacement by formation of another Zundel complex in panel d that is disconnected from the one in panel b.
(106) Agmon, N. *Chem. Phys. Lett.* **1995**, *244*, 456.
(107) Agmon, N.; Goldberg, S. Y.; Huppert, D. *J. Mol. Liq.* **1995**, *64*, 161.
(108) Ando, K.; Hynes, J. T. *J. Mol. Liq.* **1995**, *64*, 25.
(109) Agmon, N. *J. Chim. Phys. Phys.-Chim. Biol.* **1996**, *93*, 1714.
(110) Lobaugh, J.; Voth, G. A. *J. Chem. Phys.* **1996**, *104*, 2056.
(111) Ando, K.; Hynes, J. T. *J. Phys. Chem. B* **1997**, *101*, 10464.
(112) Vuilleumier, R.; Borgis, D. *J. Mol. Struct.* **1997**, *437*, 555.
(113) Vuilleumier, R.; Borgis, D. *J. Phys. Chem. B* **1998**, *102*, 4261.
(114) Vuilleumier, R.; Borgis, D. *Chem. Phys. Lett.* **1998**, *284*, 71.
(115) Schmitt, U. W.; Voth, G. A. *J. Phys. Chem. B* **1998**, *102*, 5547.
(116) Sagnella, D. E.; Tuckerman, M. E. *J. Chem. Phys.* **1998**, *108*, 2073.
(117) Vuilleumier, R.; Borgis, D. *J. Chem. Phys.* **1999**, *111*, 4251.
(118) Agmon, N. *Isr. J. Chem.* **1999**, *39*, 493.
(119) Schmitt, U. W.; Voth, G. A. *J. Chem. Phys.* **1999**, *111*, 9361.
(120) Marx, D.; Tuckerman, M. E.; Hutter, J.; Parrinello, M. *Nature (London)* **1999**, *397*, 601; see also ref 121.
(121) Hynes, J. T. *Nature (London)* **1999**, *397*, 565.
(122) Marx, D.; Tuckerman, M. E.; Parrinello, M. *J. Phys.: Condens. Matter* **2000**, *12*, A153.
(123) Vuilleumier, R.; Borgis, D. *J. Mol. Struct.* **2000**, *552*, 117.
(124) Schmitt, U. W.; Voth, G. A. *Chem. Phys. Lett.* **2000**, *329*, 36.
(125) Day, T. J. F.; Schmitt, U. W.; Voth, G. A. *J. Am. Chem. Soc.* **2000**, *122*, 12027.
(126) Geissler, P. L.; Dellago, C.; Chandler, D.; Hutter, J.; Parrinello, M. *Science* **2001**, *291*, 2121. ; see also Klein, M. L. *Science* **2001**, *291*, 2106.
(127) Day, T. J. F.; Soudackov, A. V.; Cuma, M.; Schmitt, U. W.; Voth, G. A. *J. Chem. Phys.* **2002**, *117*, 5839.
(128) Kim, J.; Schmitt, U. W.; Gruetzmacher, J. A.; Voth, G. A.; Scherer, N. E. *J. Chem. Phys.* **2002**, *116*, 737.
(129) Lapid, H.; Agmon, N.; Petersen, M. K.; Voth, G. A. *J. Chem. Phys.* **2005**, *122*, 014506.
(130) Asthagiri, D.; Pratt, L. R.; Kress, J. D. *Proc. Natl. Acad. Sci. U.S.A.* **2005**, *102*, 6704.
(131) Boero, M.; Ikeshoji, T.; Terakura, K. *ChemPhysChem* **2005**, *6*, 1775.
(132) Swanson, J. M. J.; Maupin, C. M.; Chen, H.; Petersen, M. K.; Xu, J.; Wu, Y.; Voth, G. A. *J. Phys. Chem. B* **2007**, *111*, 4300.
(133) Markovitch, O.; Chen, H.; Izvekov, S.; Paesani, F.; Voth, G. A.; Agmon, N. *J. Phys. Chem. B* **2008**, *112*, 9456; see also ref 105.
(134) Chandra, A.; Tuckerman, M. E.; Marx, D. *Phys. Rev. Lett.* **2007**, *99*, 145901.
(135) Tuckerman, M. E.; Marx, D.; Parrinello, M. *Nature (London)* **2002**, *417*, 925; see also ref 15.
(136) Stillinger, F. H. *Science* **1980**, *209*, 451.
(137) Marx, D. *Science* **2004**, *303*, 634.
(138) Wernet, P.; Nordlund, D.; Bergmann, U.; Cavalleri, M.; Odelius, M.; Ogasawara, H.; Naslund, L. A.; Hirsch, T. K.; Ojamae, L.; Glatzel, P.; Pettersson, L. G. M.; Nilsson, A. *Science* **2004**, *304*, 995.
(139) Marx, D.; Parrinello, M. *Z. Phys. B (Rapid Note)* **1994**, *95*, 143.
(140) Marx, D.; Parrinello, M. *J. Chem. Phys.* **1996**, *104*, 4077.
(141) Tuckerman, M. E.; Marx, D.; Klein, M. L.; Parrinello, M. *J. Chem. Phys.* **1996**, *104*, 5579.
(142) Marx, D.; Tuckerman, M. E.; Martyna, G. J. *Comput. Phys. Commun.* **1999**, *118*, 166.
(143) Eucken, A. *Z. Elektrochem.* **1948**, *52*, 255.
(144) Gierer, A.; Wirtz, K. *Ann. Phys.* (Leipzig, 6. Folge) 1949, *6*, 257; see in particular p 282 ("Da H^+- und OH^--Ion einen ähnlichen Mechanismus für die Extrabeweglichekeit haben, vermuten wir, daβ auch der Struktureinfluβ des Wassers ähnlich ist."); p 283 ("Wir beschränken uns im folgenden auf die Betrachtung des H^+-Ions; gleiche Betrachtungen gelten für das OH^--Ion, ..."); and p 296 ("Abgesehen von dem verschiedenen q gilt für OH^--Ionen die gleiche Formel (52) wie für H^+-Ionen."); see also section III.4 "Die Arbeit von Huggins" wherein ref 171 is discussed ("Wenn das Modell von Huggins auch nicht ohne weiteres eine quantitative Theorie ergibt,

so entspricht es doch am besten unseren heutigen Vorstellungen von der Bedeutung von Wasserstoffbrücken für die Extraleitfähigkeit.").
(145) Marcus, R. A. *Annu. Rev. Phys. Chem.* **1964**, *15*, 155.
(146) Marcus, R. A. *Angew. Chem., Int. Ed. Engl.* **1993**, *32*, 1111.
(147) Borgis, D.; Hynes, J. T. *Chem. Phys.* **1993**, *170*, 315.
(148) Staib, A.; Borgis, D.; Hynes, J. T. *J. Chem. Phys.* **1995**, *102*, 2487.
(149) Borgis, D.; Hynes, J. T. *J. Phys. Chem.* **1996**, *100*, 1118.
(150) Ando, K.; Hynes, J. T. *Adv. Chem. Phys.* **1999**, *110*, 381.
(151) Kiefer, P. M.; Hynes, J. T. *J. Phys. Chem. A* **2004**, *108*, 11793.
(152) Laage, D.; Hynes, J. T. *Science* **2006**, *311*, 832; see also ref 153.
(153) Ludwig, R. *ChemPhysChem* **2007**, *8*, 44.
(154) Palascak, M. W.; Shields, G. C. *J. Phys. Chem. A* **2004**, *108*, 3692.
(155) Danneel, H. *Z. Elektrochem.* **1905**, *11* (16), 249.; see in particular p 250: "Dasselbe würde für das *OH′*-Ion und für alle Ionen des Lösungsmittels gelten.". This communication is a direct reply to the note. Tijmstra Bz, S.; Notiz über Ionengeschwindigkeiten., *Z. Elektrochem.* **1905**, *11* (16), 249–249. on two reviewlike publications by Danneel slightly earlier in the same volume (Danneel, H. *Z. Elektrochem.* **1905**, *11* (8), 118., see in particular the footnote on p 125, and Danneel, H. *Z. Elektrochem.* **1905**, *11* (13), 202)., where Danneel discusses the papers Dempwolff, C. *Phys. Z.* **1904**, *5* (20), 637 and Tijmstra Bz., S. *Z. Phys. Chem. (Leipzig)* **1904**, *49*, 345., respectively, on conductivity measurements of CH_3O^- in alcohols and their aqueous mixtures, yielding an astonishingly high mobility (*"Wanderungsgeschwindigkeit"*) for this large anion.
(156) Hückel, E. *Z. Elektrochem.* **1928**, *34*, 546.; see in particular p 547 ("Das Wasserstoffion in wä*β*riger Lösung ist also sozusagen ein Wassermolekül, das ein Proton zu viel, das Hydroxylion ein Wassermolekül, das ein Proton zu wenig hat."); p 550 ("Im Mittel findet so ein Transport von Protonen von links nach rechts statt, der einem Wandern von OH-Ionen als Ganzes in entgegengesetzter Richtung äquivalent ist."); p 550 ("Die anzustellenden Überlegungen und Rechnungen lassen sich ohne weiteres sinngemä*β* auf den Fall des OH-Ions übertragen."); and p 561 ("Wir verzichten hier darauf, das Verhalten des OH-Ions im einzelnen zu diskutieren, da dieses gegenüber der Diskussion beim Wasserstoffion nichts Neues ergibt.").
(157) Wannier, G. *Ann. Phys. (Leipzig, 5. Folge)* **1935**, *24*, 545–568. Ann. Physik (Leipzig, 5. Folge) 1935, *24*, 569; see in particular p 550−551 ("Von diesem Gesichtspunkt aus besitzt H_3O^+ ein Loch und drei Protonen, H_2O zwei Löcher und zwei Protonen und OH^- drei Löcher und ein Proton. Diese Auffassung bietet den Vorteil, die Rechungen stark zu vereinfachen, da H_3O^+ und OH^- dann Spiegelbilder voneinander sind: Während für H_3O^+ das überschüssige Proton von Molekel zu Molekel wandert, ist es bei OH^- das überschüssige Loch, das durch Protonen benachbarter Wassermolekeln beständig aufgefüllt wird und so eine ähnliche Wanderung durch die Flüssigkeit vollzieht. Wegen dieser Spiegelbildlichkeit kann eine explizite Erwähnung des OH^- Ions oft unterbleiben.") and p 585 ("Vor allem aber mu*β* man gegen die obigen Werte einwenden, da*β* der Unterschied zwischen H_3O^+ und OH^-, der in den experimentellen Daten zum Ausdruck kommt, durch die erhaltenen Zahlen nicht erklärt wird, da wir die auftretenden Unterschiede nicht verstehen können." (*sic!*)).
(158) Bernal, J. D.; Fowler, R. H. *J. Chem. Phys.* **1933**, *1*, 515; see in particular p 542 ("A very similar mechanism must hold for $(OH)^-$.") and p 547 ("§17. The hydroxyl ion: The extra mobility of the $(OH)^-$ is about one-half that of $(OH_3)^+$. It is obviously necessary and possible to accept the same general explanation for the extra mobility of both ions.").
(159) Huggins, M. L. *J. Am. Chem. Soc.* **1931**, *53*, 3190; see in particular p 3191 ("Analogously, an OH^- ion can remove a hydrogen from a water molecule if the oxygen in the latter has around it three other hydrogens (Scheme)."); see ref 171 for a modified viewpoint.
(160) Stearn, A. E.; Eyring, H. *J. Chem. Phys.* **1937**, *5*, 113; see in particular p 121: "The same treatment of the conductance of O^-H will give a $\Delta F^{\ddagger}$ for the reaction $H_2O + O^-H \rightarrow O^-H + H_2O$ lying in this same range."
(161) Moore, W. J. *Physical Chemistry*, 5th ed.; Longman: London, 1972−1990; see Chapter 10.12, pp 435−436.
(162) Schiöberg, D.; Zundel, G. *J. Chem. Soc., Faraday Trans. 2* **1973**, *69*, 771; see in particular Figure 2b.
(163) Stillinger, F. H. Proton Transfer Reactions and Kinetics in Water. In *Theoretical Chemistry: Advances and Perspectives*; Eyring, H., Henderson, D., Eds.; Academic Press: New York, 1978; pp 177−234; see in particular Figures 1, 2, and 12.
(164) Agmon, N. *Chem. Phys. Lett.* **2000**, *319*, 247.
(165) Moore, J. H.; Spencer, N. D. *Encyclopedia of Chemical Physics and Physical Chemistry*; Institute of Physics Publishing: Bristol, 2001; see section A2.4.3.3 and p 490 in Vol. I.
(166) Asthagiri, D.; Pratt, L. R.; Kress, J. D.; Gomez, M. A. *Chem. Phys. Lett.* **2003**, *380*, 530.
(167) Asthagiri, D.; Pratt, L. R.; Kress, J. D.; Gomez, M. A. *Proc. Natl. Acad. Sci. U.S.A.* **2004**, *101*, 7229. and Tech. Rep., Los Alamos Natl. Lab. LA-UR-02-7006 (2002), available from www.arxiv.org/abs/physics/0211057.
(168) Levine, I. N. *Physical Chemistry*, 6th ed.; McGraw-Hill: New York, 2009; see scheme on p 501 in Chapter 15.6.
(169) Zatsepina, G. N. *J. Struct. Chem.* **1971**, *12*, 894. (translated from Zh. Strukt. Khim. 1971, 12 (6), 969−974; see ref therein on an earlier publication in Russian on a similar topic: Zatsepina, G. N. Zh. Strukt. Khim. 1969, *10*, 211.
(170) Librovich, N. B.; Sakun, V. P.; Sokolov, N. D. *Chem. Phys.* **1979**, *39*, 351; see also. Giguere, P. A. *Chem. Phys.* **1981**, *60*, 421. Librovich, N. B.; Sakun, V. P.; Sokolov, N. D. *Chem. Phys.* **1981**, *60*, 425.
(171) Huggins, M. L. *J. Phys. Chem.* **1936**, *40*, 723; see, in particular, p 726: "In water solution such an ion [*i.e. an* OH^- *ion*], unlike H^+, would probably not form aggregates such as $(H\text{-}O\text{-}H\text{-}O\text{-}H)^-$ because the larger Coulomb repulsion between the oxygens and larger Coulomb attraction between the central hydrogen and each oxygen would tend to make the central hydrogen bridge an unsymmetrical one. The oxygen atom in an OH^- ion would be expected to tend to surround itself with four unsymmetrical hydrogen bridges, like that in a water molecule or $H_5O_2^+$ ion."; see ref 159 for an earlier, different viewpoint.
(172) Herrmann, H.; Hertz, H. G.; Maurer, R. *Chimia* **1985**, *39*, 61.
(173) Muller, R. P.; Warshel, A. *J. Phys. Chem.* **1995**, *99*, 17516.
(174) Tunón, I.; Rinaldi, D.; Ruiz-López, M. F.; Rivail, J. L. *J. Phys. Chem.* **1995**, *99*, 3798.
(175) Tunón, I.; Martins-Costa, M. T. C.; Millot, C.; Ruiz-López, M. F. *J. Chem. Phys.* **1997**, *106*, 3633.
(176) Ruiz-López, M. F.; Oliva, A.; Tunón, I.; Bertran, J. *J. Phys. Chem. A* **1998**, *102*, 10728.
(177) Pliego, J. R.; Riveros, J. M. *J. Phys. Chem. B* **2000**, *104*, 5155.
(178) Zhu, Z. W.; Tuckerman, M. E. *J. Phys. Chem. B* **2002**, *106*, 8009.
(179) Chen, B.; Park, J. M.; Ivanov, I.; Tabacchi, G.; Klein, M. L.; Parrinello, M. *J. Am. Chem. Soc.* **2002**, *124*, 8534.
(180) Chen, B.; Ivanov, I.; Park, J. M.; Parrinello, M.; Klein, M. L. *J. Phys. Chem. B* **2002**, *106*, 12006.
(181) Hermida-Ramón, J. M.; Karlström, G. *J. Phys. Chem. A* **2003**, *107*, 5217.
(182) Vassilev, P.; Louwerse, M. J.; Baerends, E. J. *J. Phys. Chem. B* **2005**, *109*, 23605.
(183) Ufimtsev, I. S.; Kalinichev, A. G.; Martinez, T. J.; Kirkpatrick, R. J. *Chem. Phys. Lett.* **2007**, *442*, 128.
(184) Megyes, T.; Balint, S.; Grosz, T.; Radnai, T.; Bakó, I.; Sipos, P. *J. Chem. Phys.* **2008**, *128*, 044501.
(185) Vácha, R.; Megyes, T.; Bakó, I.; Pusztai, L.; Jungwirth, P. *J. Phys. Chem. A* **2009**, *113*, 4022.
(186) De Paz, M.; Giardini, A. G.; Friedman, L. *J. Chem. Phys.* **1970**, *52*, 687.
(187) Meot-Ner (Mautner), M.; Speller, C. V. *J. Phys. Chem.* **1986**, *90*, 6616.
(188) Yang, X.; Castleman, A. W., Jr. *J. Phys. Chem.* **1990**, *94*, 8500.
(189) Buchner, R.; Hefter, G.; May, P. M.; Sipos, P. *J. Phys. Chem. B* **1999**, *103*, 11186.
(190) Bruni, F.; Ricci, M. A.; Soper, A. K. *J. Chem. Phys.* **2001**, *114*, 8056; see also ref 191.
(191) Note: the detailed solvation shell structure of OH^-(aq) was not investigated in ref 190 from 2001. Rather, it was devoted to analyzing the total structure of a concentrated NaOH aqueous solution in liquid and glassy states; the 10 molar (10 M) concentration used corresponds to about one Na^+ and one OH^- ion per 5.2 water molecules. It was not until 2003 that the first detailed analysis of the solvation shell of the hydrated hydroxide was published[196] for a 4.6 M NaOH solution (about one OH^- per 12 water molecules) using a combination of neutron diffraction with hydrogen isotopic substitution and Monte Carlo simulation within the so-called "empirical potential structure refinement" (EPSR) framework. The concentration dependence down to 2 M (corresponding to about 1:28 molecules) was studied in refs 197 and 200 whereas counterion effects were analyzed systematically in ref 198 using LiOH, NaOH, and KOH solutions covering the concentration range from 1:3 down to 1:12.
(192) Chaudhuri, C.; Wang, Y.-S.; Jiang, J. C.; Lee, Y. T.; Chang, H.-C.; Niedner-Schatteburg, G. *Mol. Phys.* **2001**, *99*, 1161.
(193) Nienhuys, H.-K.; Lock, A. J.; van Santen, R. A.; Bakker, H. J. *J. Chem. Phys.* **2002**, *117*, 8021.
(194) Wang, Y.-S.; Tsai, C.-H.; Lee, Y. T.; Chang, H.-C.; Jiang, J. C.; Asvany, O.; Schlemmer, S.; Gerlich, D. *J. Phys. Chem. A* **2003**, *107*, 4217.
(195) Robertson, W. H.; Diken, E. G.; Price, E. A.; Shin, J.-W.; Johnson, M. A. *Science* **2003**, *299*, 1367. See also: Huneycutt, A. J.; Saykally, R. J. *Science* **2003**, *299*, 1329.
(196) Botti, A.; Bruni, F.; Imberti, S.; Ricci, M. A.; Soper, A. K. *J. Chem. Phys.* **2003**, *119*, 5001.

(197) Botti, A.; Bruni, F.; Imberti, S.; Ricci, M. A.; Soper, A. K. *J. Chem. Phys.* **2004**, *120*, 10154.
(198) Imberti, S.; Botti, A.; Bruni, F.; Cappa, G.; Ricci, M. A.; Soper, A. K. *J. Chem. Phys.* **2005**, *122*, 194509.
(199) Botti, A.; Bruni, F.; Imberti, S.; Ricci, M. A.; Soper, A. K. *J. Mol. Liq.* **2005**, *117*, 81.
(200) McLain, S. E.; Imberti, S.; Soper, A. K.; Botti, A.; Bruni, F.; Ricci, M. A. *Phys. Rev. B* **2006**, *74*, 094201.
(201) Corridoni, T.; Sodo, A.; Bruni, F.; Ricci, M. A.; Nardone, M. *Chem. Phys.* **2007**, *336*, 183.
(202) Smiechowski, M.; Stangret, J. *J. Phys. Chem. A* **2007**, *111*, 2889.
(203) Smiechowski, M.; Stangret, J. *J. Mol. Struct.* **2007**, *834*−*836*, 239.
(204) Cappa, C. D.; Smith, J. D.; Messer, B. M.; Cohen, R. C.; Saykally, R. J. *J. Phys. Chem. A* **2007**, *111*, 4776.
(205) Aziz, E. F.; Ottosson, N.; Faubel, M.; Hertel, I. V.; Winter, B. *Nature (London)* **2008**, *455*, 89.
(206) Roberts, S. T.; Petersen, P. B.; Ramasesha, K.; Tokmakoff, A.; Ufimtsev, I. S.; Martinez, T. J. *Proc. Natl. Acad. Sci. U.S.A.* **2009**, *106*, 15154.
(207) Kutzelnigg, W. *Einführung in die Theoretische Chemie*; Wiley-VCH: Weinheim, 1975/78, 1992/94, 2002; see, in particular, Teil II, "Die chemische Bindung", section 12.
(208) Olah, G. A.; Prakash, G. K. S.; Field, L. D.; Wade, K. *Hypercarbon Chemistry*; John Wiley & Sons: New York, 1987.
(209) Olah, G. A.; Rasul, G. *Acc. Chem. Res.* **1997**, *30*, 245.
(210) Jensen, W. B. *J. Chem. Educ.* **2006**, *83*, 1751.
(211) Li, X.; Teige, V. E.; Iyengar, S. S. *J. Phys. Chem. A* **2007**, *111*, 4815.
(212) Asthagiri, D.; Pratt, L. R.; Ashbaugh, H. S. *J. Chem. Phys.* **2003**, *119*, 2702.
(213) Librovich, N. B.; Maiorov, V. D. *Russ. J. Phys. Chem.* **1982**, *56*, 624.
(214) Savin, A.; Nesper, R.; Wengert, S.; Fässler, T. F. *Angew. Chem., Int. Ed. Engl.* **1997**, *36*, 1809. Angew. Chem. 1997, *109*, 1892; see also www.cpfs.mpg.de/ELF.
(215) Liu, Y.; Tuckerman, M. E. *J. Phys. Chem. B* **2001**, *105*, 6598.
(216) Kiriukhin, M. Y.; Collins, K. D. *Biophys. Chem.* **2002**, *99*, 155.
(217) Rais, J.; Okada, T. *J. Phys. Chem. B* **2008**, *112*, 5393.
(218) Newton, M. D.; Ehrenson, S. *J. Am. Chem. Soc.* **1971**, *93*, 4971.
(219) Masamura, M. *J. Chem. Phys.* **2002**, *117*, 5257.
(220) Masamura, M. *J. Comput. Chem.* **2002**, *22*, 31.
(221) Zhan, C.-G.; Dixon, D. A. *J. Phys. Chem. A* **2002**, *106*, 9737.
(222) Lee, H. M.; Tarkeshwar, P.; Kim, K. S. *J. Chem. Phys.* **2004**, *121*, 4657.
(223) Pliego, J. R., Jr.; Riveros, J. M. *J. Chem. Phys.* **2000**, *112*, 4045.
(224) Pickard, F. C., IV; Pokon, E. K.; Liptak, M. D.; Shields, G. C. *J. Chem. Phys.* **2005**, *122*, 024302.
(225) Dahlke, E. E.; Orthmeyer, M. A.; Truhlar, D. G. *J. Phys. Chem. B* **2008**, *112*, 2372.
(226) Novoa, J. J.; Mota, F.; del Valle, C. P.; Planas, M. *J. Phys. Chem. A* **1997**, *101*, 7842.
(227) Note: the OH^-(aq) diffusion coefficient reported in Table 21.8 in ref 1 should read 5.30×10^{-9} m^2/s instead of 5.03×10^{-9} m^2/s, as printed.
(228) Mills, R. *J. Phys. Chem.* **1973**, *77*, 685.
(229) Hardy, E. H.; Zygar, A.; Zeidler, M. D.; Holz, M.; Sacher, F. D. *J. Chem. Phys.* **2001**, *114*, 3174.
(230) Marcus, Y. *Ion Properties*; Marcel Dekker: New York, 1997; see in particular Chapter 11, "Ion Transport", and Table 14, "Transport Properties", therein.
(231) Heinzinger, K.; Weston, R. E., Jr. *J. Phys. Chem.* **1964**, *68*, 744.
(232) Heinzinger, K.; Weston, R. E., Jr. *J. Phys. Chem.* **1964**, *68*, 2179.
(233) Perdew, J. P.; Wang, Y. *Phys. Rev. B.* **1992**, *45*, 13244. Perdew, J. P.; Chevary, J. A.; Vosko, S. H.; Jackson, K. A.; Pederson, M. R.; Singh, D. J.; Fiolhais, C. *Phys. Rev. B* **1992**, *46*, 6671.
(234) Becke, A. D. *Phys. Rev. A* **1988**, *38*, 3098.
(235) Lee, C.; Wang, W.; Parr, R. G. *Phys. Rev. B* **1988**, *37*, 785.
(236) Boese, A. D.; Doltsinis, N. L.; Handy, N. C.; Sprik, M. *J. Chem. Phys.* **2000**, *112*, 1670.
(237) Marx, D. Theoretical Chemistry in the 21st Century: The "Virtual Lab". In *Proceedings of the "Idea-Finding Symposium: Frankfurt Institute for Advanced Studies"*; Greiner, W., Reinhardt, J., Eds.; EP Systema: Debrecen, 2004; pp 139−153. see www.theochem.rub.de/go/cprev.html.
(238) Sprik, M.; Hutter, J.; Parrinello, M. *J. Chem. Phys.* **1996**, *105*, 1142.
(239) Kuo, I.-F. W.; Mundy, C. J.; McGrath, M. J.; Siepmann, J. I.; VandeVondele, J.; Sprik, M.; Hutter, J.; Chen, B.; Klein, M. L.; Mohamed, F.; Krack, M.; Parrinello, M. *J. Phys. Chem. B* **2004**, *108*, 12990.
(240) VandeVondele, J.; Mohamed, F.; Krack, M.; Hutter, J.; Sprik, M.; Parrinello, M. *J. Chem. Phys.* **2005**, *122*, 014515.
(241) Kuo, I.-F. W.; Mundy, C. J.; McGrath, M. J.; Siepmann, J. I. *J. Chem. Theor. Comput.* **2006**, *2*, 1274.
(242) Todorova, T.; Seitsonen, A. P.; Hutter, J.; Kuo, I.-F. W.; Mundy, C. J. *J. Phys. Chem. B* **2006**, *110*, 3685.
(243) Mallik, B. S.; Semparithi, A.; Chandra, A. *J. Phys. Chem. A* **2008**, *112*, 5104.
(244) Kühne, T. D.; Krack, M.; Parrinello, M. *J. Chem. Theor. Comput.* **2009**, *5*, 235.
(245) Geissler, P. L.; Van Voorhis, T.; Dellago, C. *Chem. Phys. Lett.* **2000**, *324*, 149.
(246) Handgraaf, J.-W.; van Erp, T. S.; Meijer, E. J. *Chem. Phys. Lett.* **2003**, *367*, 617.
(247) Morrone, J. A.; Tuckerman, M. E. *Chem. Phys. Lett.* **2003**, *370*, 406.
(248) Diraison, M.; Martyna, G. J.; Tuckerman, M. E. *J. Chem. Phys.* **1999**, *111*, 1096.
(249) Liu, Y.; Tuckerman, M. E. *J. Phys. Chem. B* **2001**, *105*, 6598.
(250) Boese, A. D.; Chandra, A.; Martin, J. M. L.; Marx, D. *J. Chem. Phys.* **2003**, *119*, 5965.
(251) Perdew, J. P.; Burke, K.; Ernzerhof, M. *Phys. Rev. Lett.* **1996**, *77*, 3865. Erratum: Phys. Rev. Lett. 1997, *78*, 1396.
(252) Zhang, Y.; Yang, W. *Phys. Rev. Lett.* **1998**, *80*, 890.
(253) Hammer, B.; Hansen, L. B.; Nørskov, J. K. *Phys. Rev. B* **1999**, *59*, 7413.
(254) Fernandez-Serra, M. V.; Ferlat, G.; Artacho, E. *Mol. Simul.* **2005**, *31*, 361.
(255) Schwegler, E.; Grossman, J. C.; Gygi, F.; Galli, G. *J. Chem. Phys.* **2004**, *121*, 5400.
(256) Fernández-Serra, M. V.; Artacho, E. *J. Chem. Phys.* **2004**, *121*, 11136.
(257) Sit, P. H.-L.; Marzari, N. *J. Chem. Phys.* **2005**, *122*, 204510.
(258) Lee, H.-S.; Tuckerman, M. E. *J. Chem. Phys.* **2006**, *125*, 154507.
(259) Lee, H.-S.; Tuckerman, M. E. *J. Chem. Phys.* **2007**, *126*, 164501.
(260) Longsworth, L. G. *J. Phys. Chem.* **1954**, *58*, 770.
(261) Tuckerman, M. E.; Marx, D.; Klein, M. L.; Parrinello, M. *Science* **1997**, *275*, 817.
(262) Car, R.; Parrinello, M. *Phys. Rev. Lett.* **1985**, *55*, 2471.
(263) Marx, D.; Hutter, J. *Ab Initio Molecular Dynamics: Basic Theory and Advanced Methods*; Cambridge University Press: Cambridge, 2009.
(264) Marx, D.; Hutter, J. Ab Initio Molecular Dynamics: Theory and Implementation. In *Modern Methods and Algorithms of Quantum Chemistry*; Grotendorst, J., Ed.; NIC: FZ Jülich, 2000; pp 301−449; see www.theochem.rub.de/go/cprev.html.
(265) Tuckerman, M. E. *J. Phys.: Condensed Matter* **2002**, *14*, R1297.
(266) Iftimie, R.; Minary, P.; Tuckerman, M. E. *Proc. Natl. Acad. Sci. U.S.A.* **2005**, *102*, 6654.
(267) Hutter, J.; et al. CPMD, IBM Corporation 1990−2010 and MPI für Festkörperforschung Stuttgart 1997−2001; see www.cpmd.org.
(268) Troullier, N.; Martins, J. L. *Phys. Rev. B* **1991**, *43*, 1993.
(269) Vanderbilt, D. *Phys. Rev. B* **1990**, *41*, 7892.
(270) Laasonen, K.; Pasquarello, A.; Lee, C.; Car, R.; Vanderbilt, D. *Phys. Rev. B* **1993**, *47*, 10142.
(271) Blöchl, P. E. *Phys. Rev. B* **1994**, *50*, 17953; see section V.C.2 therein for a mass renormalization scheme to correct for frequency redshifts due to using finite fictitious electron masses.
(272) Asthagiri, D.; Pratt, L. R.; Kress, J. D. *Phys. Rev. E* **2003**, *68*, 041505.
(273) Grossman, J. C.; Schwegler, E.; Draeger, E. W.; Gygi, F.; Galli, G. *J. Chem. Phys.* **2004**, *120*, 300.
(274) Izvekov, S.; Voth, G. A. *J. Chem. Phys.* **2005**, *123*, 044505. Erratum: J. Chem. Phys. 2006, *124*, 039901.
(275) Tuckerman, M. E.; Parrinello, M. *J. Chem. Phys.* **1994**, *101*, 1302.
(276) Mantz, Y. A.; Chen, B.; Martyna, G. J. *Chem. Phys. Lett.* **2005**, *405*, 294.
(277) Pastore, G.; Smargiassi, E.; Buda, F. *Phys. Rev. A* **1991**, *44*, 6334.
(278) Marx, D.; Hutter, J.; Parrinello, M. *Chem. Phys. Lett.* **1995**, *241*, 457.
(279) Marx, D.; Fois, E. S.; Parrinello, M. *Int. J. Quantum Chem.* **1996**, *57*, 655.
(280) Martyna, G. J.; Klein, M. L.; Tuckerman, M. *J. Chem. Phys.* **1992**, *97*, 2635.
(281) Tuckerman, M. E.; Berne, B. J.; Martyna, G. J.; Klein, M. L. *J. Chem. Phys.* **1993**, *99*, 2796.
(282) Benoit, M.; Marx, D.; Parrinello, M. *Nature (London)* **1998**, *392*, 258; see also. Teixeira, J. *Nature (London)* **1998**, *392*, 232.
(283) Benoit, M.; Marx, D.; Parrinello, M. *Comput. Mater. Sci.* **1998**, *10*, 88.
(284) Benoit, M.; Marx, D.; Parrinello, M. *Solid State Ionics* **1999**, *125*, 23.
(285) Benoit, M.; Marx, D. *ChemPhysChem (Commun.)* **2005**, *6*, 1738.
(286) Tuckerman, M. E.; Marx, D. *Phys. Rev. Lett.* **2001**, *86*, 4946.
(287) Rousseau, R.; Marx, D. *Phys. Rev. Lett.* **1998**, *80*, 2574.
(288) Della Sala, F.; Rousseau, R.; Görling, A.; Marx, D. *Phys. Rev. Lett.* **2004**, *92*, 183401.
(289) Egorov, S. A.; Skinner, J. L. *Chem. Phys. Lett.* **1998**, *293*, 469.
(290) Ramírez, R.; López-Ciudad, T.; Kumar, P.; Marx, D. *J. Chem. Phys.* **2004**, *121*, 3973.

(291) Poulsen, A.; Nyman, G.; Rossky, P. J. *Proc. Natl. Acad. Sci. U.S.A.* **2005**, *102*, 6709.
(292) Lawrence, C. P.; Skinner, J. L. *Proc. Natl. Acad. Sci. U.S.A.* **2005**, *102*, 6720.
(293) King-Smith, R. D.; Vanderbilt, D. *Phys. Rev. B* **1993**, *47*, 1651.
(294) Resta, R. *Rev. Mod. Phys.* **1994**, *66*, 899.
(295) Iftimie, R.; Thomas, J. W.; Tuckerman, M. E. *J. Chem. Phys.* **2004**, *120*, 2169.
(296) Thomas, J. W.; Iftimie, R.; Tuckerman, M. E. *Phys. Rev. B* **2004**, *69*, 125105.
(297) Iftimie, R.; Tuckerman, M. E. *J. Chem. Phys.* **2005**, *122*, 214508.
(298) Tobias, D. J.; Martyna, G. J.; Klein, M. L. *J. Phys. Chem.* **1993**, *97*, 12959.
(299) Stillinger, F. H. *Adv. Chem. Phys.* **1975**, *31*, 1.
(300) Rapaport, D. C. *Mol. Phys.* **1983**, *50*, 1151.
(301) Luzar, A.; Chandler, D. *Nature (London)* **1996**, *379*, 55.
(302) Luzar, A. *J. Chem. Phys.* **2000**, *113*, 10663.
(303) Chandra, A. *Phys. Rev. Lett.* **2000**, *85*, 768.
(304) Balasubramanian, S.; Pal, S.; Bagchi, B. *Phys. Rev. Lett.* **2002**, *89*, 115505.
(305) Xu, H.; Stern, H. A.; Berne, B. J. *J. Phys. Chem. B* **2002**, *106*, 2054.
(306) Schreiner, E.; Nicolini, C.; Ludolph, B.; Ravindra, R.; Otte, N.; Kohlmeyer, A.; Rousseau, R.; Winter, R.; Marx, D. *Phys. Rev. Lett.* **2004**, *92*, 148101.
(307) Rousseau, R.; Schreiner, E.; Kohlmeyer, A.; Marx, D. *Biophys. J.* **2004**, *86*, 1393.
(308) Gordon, R. G. *J. Chem. Phys.* **1966**, *45*, 1643.
(309) Gallot, G.; Bratos, S.; Pommeret, S.; Lascoux, N.; Leicknam, J.-Cl.; Kozinski, M.; Amir, W.; Gale, G. M. *J. Chem. Phys.* **2002**, *117*, 11301.
(310) Park, S.; Fayer, M. D. *Proc. Natl. Acad. Sci. U.S.A.* **2007**, *104*, 16731.
(311) Moilanen, D. E.; Fenn, E. E.; Lin, Y.-S.; Skinner, J. L.; Bagchi, B.; Fayer, M. D. *Proc. Natl. Acad. Sci. U.S.A.* **2008**, *105*, 5295.
(312) Rezus, Y. L. A.; Bakker, H. J. *J. Chem. Phys.* **2005**, *123*, 114502.
(313) Cringus, D.; Yeremenko, S.; Pshenichnikov, M. S.; Wiersma, D. A. *J. Phys. Chem. B* **2004**, *108*, 10376.
(314) Bieze, T. W. N.; van der Maarrel, J. R. C.; Leyte, J. C. *Chem. Phys. Lett.* **1993**, *216*, 56.
(315) Ludwig, R. *Chem. Phys.* **1995**, *195*, 329.
(316) van der Maarel, J. R. C.; Lankhorst, D.; De Bleijser, J.; Leyte, J. C. *Chem. Phys. Lett.* **1985**, *122*, 541.
(317) Mallik, B. S.; Chandra, A. *J. Mol. Liq.* **2008**, *143*, 31.
(318) Roscioli, J. R.; McCunn, L. R.; Johnson, M. A. *Science* **2007**, *316*, 249.
(319) Samson, C. C. M.; Klopper, W. *J. Mol. Struct. THEOCHEM* **2002**, *586*, 201.
(320) Tachikawa, M.; Shiga, M. *J. Am. Chem. Soc.* **2005**, *127*, 11908.
(321) McCoy, A. B.; Huang, X. C.; Carter, S.; Bowman, J. M. *J. Chem. Phys.* **2005**, *123*, 064317.
(322) Yu, H.-G. *J. Chem. Phys.* **2006**, *125*, 204306.
(323) Diken, E. G.; Headrick, J. M.; Roscioli, J. R.; Bopp, J. C.; Johnson, M. A.; McCoy, A. B. *J. Phys. Chem. A* **2005**, *109*, 1487.
(324) Laasonen, K.; Klein, M. L. *J. Am. Chem. Soc.* **1994**, *116*, 11620.
(325) Laasonen, K.; Klein, M. L. *J. Phys. Chem. A* **1997**, *101*, 98.
(326) Sillanpaa, A. J.; Laasonen, K. *Phys. Chem. Chem. Phys.* **2004**, *6*, 555.
(327) Tsuchida, E. *J. Phys. Soc. Jpn.* **2006**, *75*, 054801.
(328) Heuft, J. M.; Meijer, E. J. *Phys. Chem. Chem. Phys.* **2006**, *8*, 3116.
(329) Kalinichev, A. G. Private communication.
(330) Elsaesser, T., Bakker, H. J., Eds.; *Ultrafast Hydrogen Bonding Dynamics and Proton Transfer Processes in the Condensed Phase*; Kluwer: Dordrecht, 2002.
(331) Nibbering, E. T. J.; Elsaesser, T. *Chem. Rev.* **2004**, *104*, 1887.
(332) Nibbering, E. T. J.; Fidder, H.; Pines, E. *Annu. Rev. Phys. Chem.* **2005**, *56*, 337.
(333) Bakker, H. J. *Chem. Rev.* **2008**, *108*, 1456.
(334) Stenger, J.; Madsen, D.; Hamm, P.; Nibbering, E. T. J.; Elsaesser, T. *Phys. Rev. Lett.* **2001**, *87*, 027401.
(335) Kropman, M. F.; Bakker, H. J. *Science* **2001**, *291*, 2118.
(336) Fecko, C. J.; Eaves, J. D.; Loparo, J. J.; Tokmakoff, A.; Geissler, P. L. *Science* **2003**, *301*, 1698.
(337) Omta, A. W.; Kropman, M. F.; Woutersen, S.; Bakker, H. J. *Science* **2003**, *301*, 347.
(338) Huse, N.; Heyne, K.; Dreyer, J.; Nibbering, E. T. J.; Elsaesser, T. *Phys. Rev. Lett.* **2003**, *91*, 197401.
(339) Nibbering, E. T. J.; Elsaesser, T. *Chem. Rev.* **2004**, *104*, 1887.
(340) Loparo, J. J.; Fecko, C. J.; Eaves, J. D.; Roberts, S. T.; Tokmakoff, A. *Phys. Rev. B* **2004**, *70*, 180201.
(341) Cowan, M. L.; Bruner, B. D.; Huse, N.; Dwyer, J. R.; Chugh, B.; Nibbering, E. T. J.; Elsaesser, T.; Miller, R. J. D. *Nature (London)* **2005**, *434*, 199.
(342) Dokter, A. M.; Woutersen, S.; Bakker, H. J. *Phys. Rev. Lett.* **2005**, *94*, 178301.
(343) Eaves, J. D.; Loparo, J. J.; Fecko, C. J.; Roberts, S. T.; Tokmakoff, A.; Geissler, P. L. *Proc. Natl. Acad. Sci. U.S.A.* **2005**, *102*, 13019.
(344) Sakyally, R. *Chem. Phys. Lett.* **2009**, *481*, 1.
(345) Mundy, C. J.; Kuo, I. F. W.; Tuckerman, M. E.; Lee, H.-S.; Tobias, D. J. *Chem. Phys. Lett.* **2009**, *481*, 2.
(346) Beattie, J. K. *Chem. Phys. Lett.* **2009**, *481*, 17.
(347) Gray-Weale, A. *Chem. Phys. Lett.* **2009**, *481*, 22.
(348) Winter, B.; Faubel, M.; Vácha, R.; Jungwirth, P. *Chem. Phys. Lett.* **2009**, *481*, 19.
(349) Sun, X.; Yoo, S.; Xantheas, S. S.; Dang, L. *Chem. Phys. Lett.* **2009**, *481*, 9.
(350) Creux, P.; Lachaise, J.; Graciaa, A.; Beattie, J. K.; Djerdjev, A. M. *J. Phys. Chem. B* **2009**, *113*, 14146.
(351) Tian, C. S.; Shen, Y. R. *Proc. Natl. Acad. Sci. U.S.A.* **2009**, *106*, 15148.
(352) Gray-Weale, A.; Beattie, J. K. *Phys. Chem. Chem. Phys.* **2009**, *11*, 10994.
(353) Ufimtsev, I. S.; Kalinichev, A. G.; Martinez, T. J.; Kirkpatrick, R. J. *Phys. Chem. Chem. Phys.* **2009**, *11*, 9420.
(354) Cwiklik, L.; Devlin, J. P.; Buch, V. *J. Phys. Chem. A* **2009**, *113*, 7482.
(355) Kim, J.-H.; Kim, Y.-K.; Kang, H. *J. Chem. Phys.* **2009**, *131*, 044705.
(356) Adriaanse, C.; Sulpizi, M.; VandeVondele, J.; Sprik, M. *J. Am. Chem. Soc.* **2009**, *131*, 6046.
(357) Bryantsev, V. S.; Diallo, M. S.; van Duin, A. C. T.; Goddard, W. A., III. *J. Chem. Theor. Comput.* **2009**, *5*, 1016.
(358) Chen, H.; Voth, G. A.; Agmon, N. *J. Phys. Chem. B* **2009**, *114*, 333.
(359) Berkelbach, T. C.; Lee, H. S.; Tuckerman, M. E. *Phys. Rev. Lett.* **2009**, *103*, 238302.

CR900233F